Miniaturization of light-sheet microscopy systems using MEMS as active optical elements

Spyridon Bakas

Department of Electrical and Electronic Engineering

University of Strathclyde

A thesis presented in fulfilment of the requirements for the degree of Doctor of Philosophy

June 29, 2024

This thesis is the result of the author's original research. It has been composed by the author and has not been previously submitted for examination which has led to the award of a degree. The copyright of this thesis belongs to the author under the terms of the United Kingdom Copyright Acts as qualified by University of Strathclyde Regulation 3.50. Due acknowledgement must always be made of the use of any material contained in, or derived from, this thesis.

Signed:

Date: 29/06/2024

Spyridon Bakas

Research outputs

Journal articles

- Bakas, S., Uttamchandani, D., Toshiyoshi, H. et al. MEMS enabled miniaturized light-sheet microscopy with all optical control. Sci Rep 11, 14100 (2021), https://doi.org/10.1038/s41598-021-93454-8

Conference proceedings articles and oral presentations

- Bakas, Spyridon, Deepak Uttamchandani, and Ralf Bauer. "Light-sheet microscopy using MEMS and active optics for 3D image acquisition control." MOEMS and Miniaturized Systems XIX. Vol. 11293. SPIE, 2020, https://doi.org/10.1117/12.2544987
- Photonics for Health, Atmosphere, Safety and Education (PHASE 2020)
- Bakas, Spyridon, et al. "MEMS enabled control of light-sheet microscopy optical beam paths." 2018 International conference on Optical MEMS and Nanophotonics (OMN). IEEE, 2018. https://doi.org/10.1109/OMN.2018.8454642
- Bakas, Spyridon, et al. "A miniaturised light-sheet microscopy system using MEMS micromirror control." 2019 International Conference on Optical MEMS and Nanophotonics (OMN). IEEE, 2019. 10.1109/OMN.2019.8925053

Conference posters

- IOP photon Birmingham 2018
- Photonics - 2018 Delhi
- PHOTONEX Glasgow 2019
- Virtual Light Sheet Fluorescence Microscopy Meeting 2020
- Virtual IOP photon 2020

Abstract

Light-sheet microscopy is widely recognised in the field of bioimaging as one of the main options when it comes to 3D imaging of large cleared samples or live imaging of organisms. This can be mainly attributed to certain advantages that result from its unique orthogonal optical geometry, such as low photobleaching and fast acquisition of 3D volumes. This work introduces two compact light-sheet microscopy systems that explore the miniaturization of the technique, with the use of small-scale devices that control the operation of the illumination and imaging path. In the two main systems presented in this work two different 2D micro-electromechanical systems (MEMS) mirrors are used for the generation of the scanned light-sheet in one axis, as well as, for the parallel translation of the light-sheet on the orthogonal axis. In this way the parallel planes of the sample can be illuminated without the need of a mechanical stage. This type of optical translation is coupled with the use of a tunable lens in the imaging path that refocuses to each subsequent illuminated plane. The result of this is a stage-free microscope with all optical scanning. An exploration to the use of a secondary tunable lens is also presented in this work as a tool for homogenising the light-sheet thickness throughout the field of view (FOV) by a post processing method of image "tiling". Both the MEMS and the tunable lens are small scale devices that not only contribute in a microscope with compact footprint but can equally reduce the overall cost of the device with relatively inexpensive pricing. In the same spirit the device is built with custom 3D printed holders and off-the-shelf optomechanical parts. The use of the 3D printer has also been investigated in the field of optical component design, with a custom-made 3D printed prism that was developed to correct aberrations and allow imaging of microscope slides at an angle. Different test samples are used to characterize the optical paths of the systems as well as its overall imaging performance. The collection of z stacks is accomplished with the use of a custom control software whereas attention is given to different ways of visualizing the 3D stacks that are acquired with the microscope.

Acknowledgements

First, I would like to thank my first supervisor, Dr. Ralf Bauer, for giving me the opportunity to be part of this challenging but fulfilling journey of my doctoral studies. I can now, with certainty, see that all the time and effort spent working together under your guidance outweigh the difficult and uncertain moments of this journey, and I appreciate all the experiences we shared. The two collaborative trips to India as part of this project were unforgettable experiences that would not have been possible without your hard work and initiative.

I would like to extend my gratitude to Mark Donnachie and Dr. Peter Tinning, with whom I was fortunate to share a lab during my time at the University of Strathclyde. Our scientific and non-scientific discussions greatly supported me and alleviated the challenges and pressures that naturally arose during my studies. Similarly, I would like to thank my second supervisor, Professor Deepak Uttamchandani, for his invaluable guidance and direction.

Of course, I want to express my heartfelt thanks to my entire family. You have all been exceptionally supportive, and I struggle to see how this would have been possible without you. Both during my time at the university and especially during my writing period, you were always there for me and helped me navigate the final and most challenging step of my experience.

Finishing this work would not have been possible without the support of my current line manager, Dr. James Swoger, who has consistently provided the understanding and guidance that allowed me to continue working on the final parts of my thesis while also starting my new role.

I would also like to thank all my close friends from Glasgow and Greece for being there for me when needed and for allowing me to share both the positive and challenging aspects of this experience. Finally, I would like to sincerely thank my close circle in my current city. You were there for me during one of the most difficult parts of my journey, balancing the completion of my thesis with the challenges of starting a new job in a new country. Thank you for all the understanding, acceptance and frankness you showed me.

Table of Contents

1 Introduction

1.1 Motivation

Biomedical research has seen great advancements during the past few decades, with its tangible outcomes providing a greater understanding of human life while having a direct impact in the fields of medicine and pharmacy. This effort has been greatly benefited by the advances in technology associated with the field. For example, the imaging instruments used in biomedical sciences have been steadily advancing their technology, enabling scientists to extract more information out of samples with improved resolution in time and space. One of the ubiquitous used tools in this effort are microscopes which are present in significant amount of experimental methods, allowing the visualization of samples and analysis of their features. Microscopy itself has seen great research advancements over the last few decades, with a range of newly developed instruments and imaging approaches achieving different crucial requirements set by biomedical scientists such as higher resolution [1], better contrast [2], fast live-cell imaging [3], ease of use [4], [5] and minimal photodamage to samples [6]. Most of these requirements have been met by optical microscopes based on fluorescence imaging. Matching specific fluorescently labelled antibodies to different parts of a sample gives researchers the opportunity to target and isolate features of interest, increasing imaging parameters such as selectivity and contrast. The usual trade-off between higher resolution and larger instantaneous FOV (Field of View) is an example where different microscopy approaches can be applied to target each specific biomedical question with different microscopes targeting a different imaging scenario requirement.

While microscopes in general use a single imaging objective to excite and collect fluorescence, a new concept of the fluorescent microscope was introduced with the development of the light-sheet fluorescence microscope (LSFM) that decouples the illumination and imaging. In its initial form an orthogonal imaging system was described by R. Zsigmondy in 1902 [7] and later developed as a fluorescence

instrument by Voie [8] and by E. Stelzer et al. [9].It would take another few years since the idea got reintroduced in its complete form as a selective plane imaging system by Huisken et al. [10]. LSFM aims to tackle two very important constraints that prior existing microscopes were facing for 3D samples and long-time imaging, namely, 3D imaging speed and contrast of samples and long-term imaging through reduced photobleaching and phototoxicity of the sample. 3D imaging is defined as the acquisition of three-dimensional data that captures volume information of a sample, in contrast with traditional 2D imaging. Even from its early stages LSFM managed to provide a faster alternative to confocal microscopy when it comes to 3D imaging as it is based on the direct imaging of a single plane compared to a point-by-point image reconstruction. Its optical geometry also meant that the light doses to the sample were significantly less and the effects of photobleaching and phototoxicity were greatly reduced [6].

With LSFM these days already being considered an establish method in fluorescence imaging [6], lots of efforts are undertaken to further improve the system capabilities and imaging results, both in academic settings and from commercial microscope vendors. Often, these efforts increase the cost, complexity, and size of the system whilst the majority of the systems are built to be used with specific samples and sample holders exclusively. This can be a limiting factor to biomedical scientists that would be interested in using the LSFM solution. LSFMs therefore have the potential to become a widely available tool in biomedical research with solutions that will manage to promote the benefits of light-sheet fluorescence imaging while providing a compact, easy-to-use and affordable solution.

1.2 Thesis Aim and Objectives

The aim of this research work is to develop a LSFM that is compact, inexpensive and has the ability to image samples in conventional mounting geometries without the need of special holders or mounting techniques. This would allow re-introducing LSFM as a tool that can benefit and complement biomedical imaging research work in standard laboratory workflows.

To achieve this aim, a number of objectives focusing on development and integration of different miniaturised elements into a new LSFM technology are targeted:

To enable a compact design, the use of microelectromechanical system (MEMS) optical micromirrors and electrical tunable lenses together with small lens geometries is targeted, allowing the development of a small footprint system. To embed these devices, a first objective was their full performance characterisation and test.

Associated with this, a second objective is the design and development of LSFM systems with all optical scanning to increase imaging speeds and limit potential sample movement induced aberrations or artefacts. In this work, a 2D MEMS mirror will be used for creating and positioning a digitally scanned light-sheet, together with a tunable lens for adjusting the imaging focus.

To increase the possible axial resolution of the systems while keeping large field of views, a third objective is the integration of an axial scan of the light-sheet illumination, which allows the creation of thinner light-sheets and therefore improved axial resolution if this scan is synchronised with rolling shutter or tiled image capture approaches.

For all investigated light-sheet approaches, the objective was to create designs that are able to use microscope slides or well-plates as specimen sample holders, feeding into the aim of an easy to use system that can be used in standard imaging workflows.

A final objective for this thesis was to make use of off-the-shelf components that can be conveniently purchased with minimal lead times, next to the use of 3D printed opto-mechanics that allow the creation of novel solutions that are developed specifically for this project.

1.3 Novelty

The work presented in this thesis has led to numerous academic publications in journals and conference proceedings. The novelty of the research can be outlined as follows:

- A first miniaturised MEMS LSFM with all-optical 3D image control.

- The first use of 2D raster scanning MEMS as light-sheet generating elements for an open-top light-sheet system.
- The first use of a 3D-printed prism as coupling element for microscope slide mounted sample geometries.
- The investigation of different MEMS micromirror actuation techniques for multiple LSFM implementations.
- A MEMS and tunable lens based axial tiling miniaturised LSFM implementation to improve axial resolution while keeping the benefits of all optical positioning scanning in a small package.

1.4 Thesis Outline

The thesis starts by covering the background knowledge and literature review of Fluorescence microscopy and LSFM as well as optical MEMS technology and their use in bio-imaging in Chapter 2. Chapter 3 focuses on the presentation and characterization of all the fundamental components that were used in the design of the optical paths and meet the requirements of being used in the proposed LSFM systems. Chapter 4 describes the implementation of a miniaturized LSFM with all optical scanning. From the optical design simulation to the implementation and characterization of the two optical paths. Initial results on imaging of cell samples are also presented here. Chapter 5 presents a more versatile LSFM system with an option to axially translate the beam waist and the use of new equipment capable of improving the 3D imaging capabilities. The optical path simulation results are shown, and the characterization is confirmed with experimental data of the created setup. Imaging results are again presented using cell samples mounted on a microscope slide. Chapter 6 opens a discussion on the main active elements of the two systems and how they compare as devices but also how they differentiate the two built systems, in the context of miniaturized LSFM design. Chapter 7 highlights conclusions of the presented work and suggests improvements and further work to make the technology more useful in the field.

2 Background

This background chapter will introduce the basics of fluorescence imaging as well as the limitations that can occur to biological samples due to increased light dosages. The theory of fluorescence microscopy in general and LSFM more specifically will additionally be covered and how its fundamental concepts allow it to be a solution with lower light doses on samples while at the same time providing faster full field imaging speeds. Additionally, the advantages and limitations of LSFM will be discussed compared to two further widely used fluorescence techniques. A review will be presented on the mechanisms that enable 3D imaging through different LSFM implementations using variations of stages and sample mounting, and how they can be a mitigating factor to the cost and usable sample variety. The second part of the background will focus on the theory of optical MEMS and a review on optical MEMS approaches for microscopy systems. Focus will be given on how MEMS mirrors can be an alternative active element in the design of LSFM and how they can turn the microscope in a more compact and accessible solution.

2.1 Fluorescence Microscopy

The purpose of this section is not to analyse all the different methods that have been established in the field of fluorescence microscopy over the last few decades. Instead, an attempt will be made to introduce the basic principles behind fluorescence microscopy along with its three major configurations and their importance and use in the field of biomedical sciences. Furthermore, the limitations and considerations of fluorescence microscopy will be discussed in the context of LSFM and the solutions that it can offer.

Imaging of biological samples is a crucial part of understanding living organisms, tissues and cells and enable research findings in the life sciences. The tools required for imaging of such samples need to provide a host of information in a small timeframe and leave the sample minimally affected after the imaging process. One of the most

important features in imaging is contrast. Contrast allows for a clear separation between different areas of the picture giving crucial information on the analysis of a subject. The concept of fluorescence microscopy was a ground-breaking development [11] in the effort of increasing the contrast and specificity of traditional brightfield microscopes by allowing users to target and resolve specific features of the sample.

2.1.1 Fluorescence

The principle of fluorescence can be explained with the Jablonski diagram [12] illustrated in Figure 1. Fluorophores are the chemical compounds widely associated with fluorescence. The ground state of the fluorophore molecule is a singlet state. Once the molecule is excited with a photon with energy that can bridge the bandgap between the ground and excited state of the fluorophore it will reach the excited state S1 or S2, with each of those states including a number of vibration energy levels. This process is called fluorescence excitation [13]. The relaxation to the lowest vibrational level of the excited state S1 occurs then in a non-radiative process happening in time scales between 10^{-14} s and 10^{-11} s. Fluorescence emission of a photon happens during the relaxation of the excited state S1 back to the ground state, with fluorescence photons being lower in energy compared to the energy of the excitation photons and emitted in a much slower timeframe between 10^{-9} s and 10^{-7} s. The change in energy has an impact on the wavelength between the excitation and emission, with the light emitted during fluorescence being longer in wavelength than the excitation light.

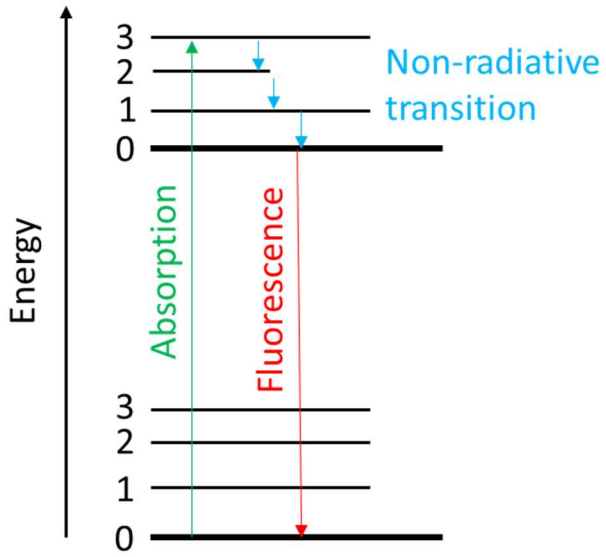

Figure 1. Jablonski Diagram of the molecular energy shifts that take place during fluorescence

The change occurring between the excitation and emission wavelength is known as Stokes shift (Figure 2) [14]. More accurately, the Stokes shift is described as the difference in wavelength between the maximum of the absorption (excitation) spectrum and the maximum of the emission spectrum for the same electronic transition in a fluorescent molecule. The excitation and emission spectra are a unique characteristic of each molecule and are unique to its molecular structure.

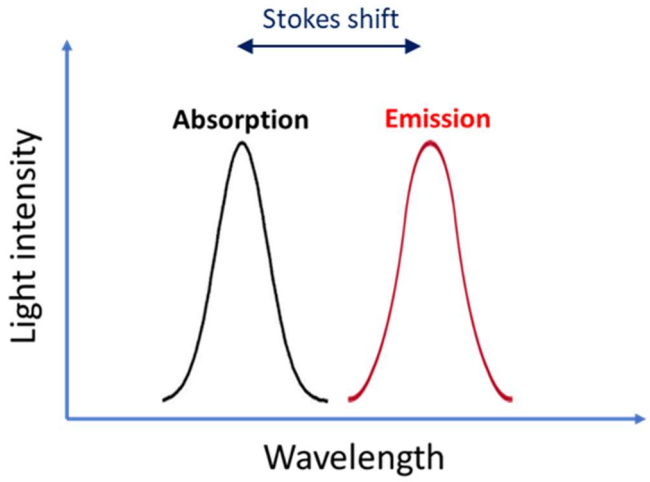

Figure 2. Stokes' shift diagram of the absorption and emission spectra

The particularity that defines the excitation and emission spectra of fluorescent molecules is what makes fluorescence such an important feature of modern microscopy experiments. The excitation profile of each different molecule is used in a strategic way to collect information on different features of a sample, allowing multiplexing of multiple fluorophores if their excitation and emission spectra can be separated during imaging [15].

Usually, biological samples have to go through a labelling process that enables them to be imaged in a fluorescence imaging setup. The way that this can be achieved is with the use of fluorescence dyes and fluorescence proteins with known properties and emission spectra that can be selectively attached to chemical substances or biological samples before the imaging process. Biological fluorescent stains are intrinsically fluorescent molecules that can be bound to the molecule of interest. Examples of this are acid stains such as DAPI that bind to the minor groove of the DNA and can be used to label the nucleus of a cell [16] or toxins such as phalloidin that is bound to a cell and stains its actin network [17]. Additional important staining categories are immunofluorescence [18], where a fluorescent treated antibody can be directly bound to its antigen of interest, and the genetical modification of proteins to fluorescent proteins, like the GFP (green fluorescent protein) [19] that allows the direct targeting of its location.

In principle, fluorescence microscope operation is based on illumination of a sample with the appropriate source wavelength to excite the fluorophores. The emitted wavelength should be the only one to be collected from the imaging set up of the microscope and the most established way to do this is by using an optical filter before the recording device to block scattered light from the excitation process. The filters are usually glass optical elements coated with layers of dielectric material. Depending on the configuration and design concept of the microscope the filter can be non-reflective or reflective also known as a dichroic mirror.

2.1.2 Wide Field Fluorescence and Confocal Microscopy

An optical microscope can fundamentally be characterized by two main components, illumination, and imaging. Both are equally important in the design of a microscope and their implementation can vary on the chosen system and possible application. For example, for illumination one can select from a range of technologies such as lasers or LED lamps and use geometrical optics to design a system that either illuminates small sections of the sample or a larger FOV depending on the application. On the other hand, the imaging of the sample aims in principle to provide a highly magnified version of the region of interest by collecting the light coming from the excited sample through magnifying optics on to a detector or a camera. As a result, a microscope needs to collect as much light as possible from the area of interest of the sample with minimal background signal. This is the aspect where fluorescence microscopy manages to excel as, according to the fluorescence theory explained previously, only areas of the sample that are fluorescently labelled will emit the wavelength of light that the filter propagates towards the detector device.

In order to further understand the methodology of fluorescence microscopy it will be useful to provide an overview of the two main methods in the field, wide-field fluorescence microscopy and confocal microscopy. Wide-field fluorescence microscopy refers to the epifluorescence microscopy setup shown in Figure 3 where the same objective is used for imaging and illumination and the full field of view available through the objective is illuminated at the same time [20]. In its simplest configuration a dichroic mirror will be used to separate the two paths and an addition of an emission filter is blocking scattered light entering the camera. Even though wide-field microscopes can provide excellent results with a simple design they tend to suffer from certain limitations as the excitation beam will illuminate areas of the sample that are not being imaged, exciting fluorescence from out of focus areas and causing blurring and increased background signal in 3D samples.

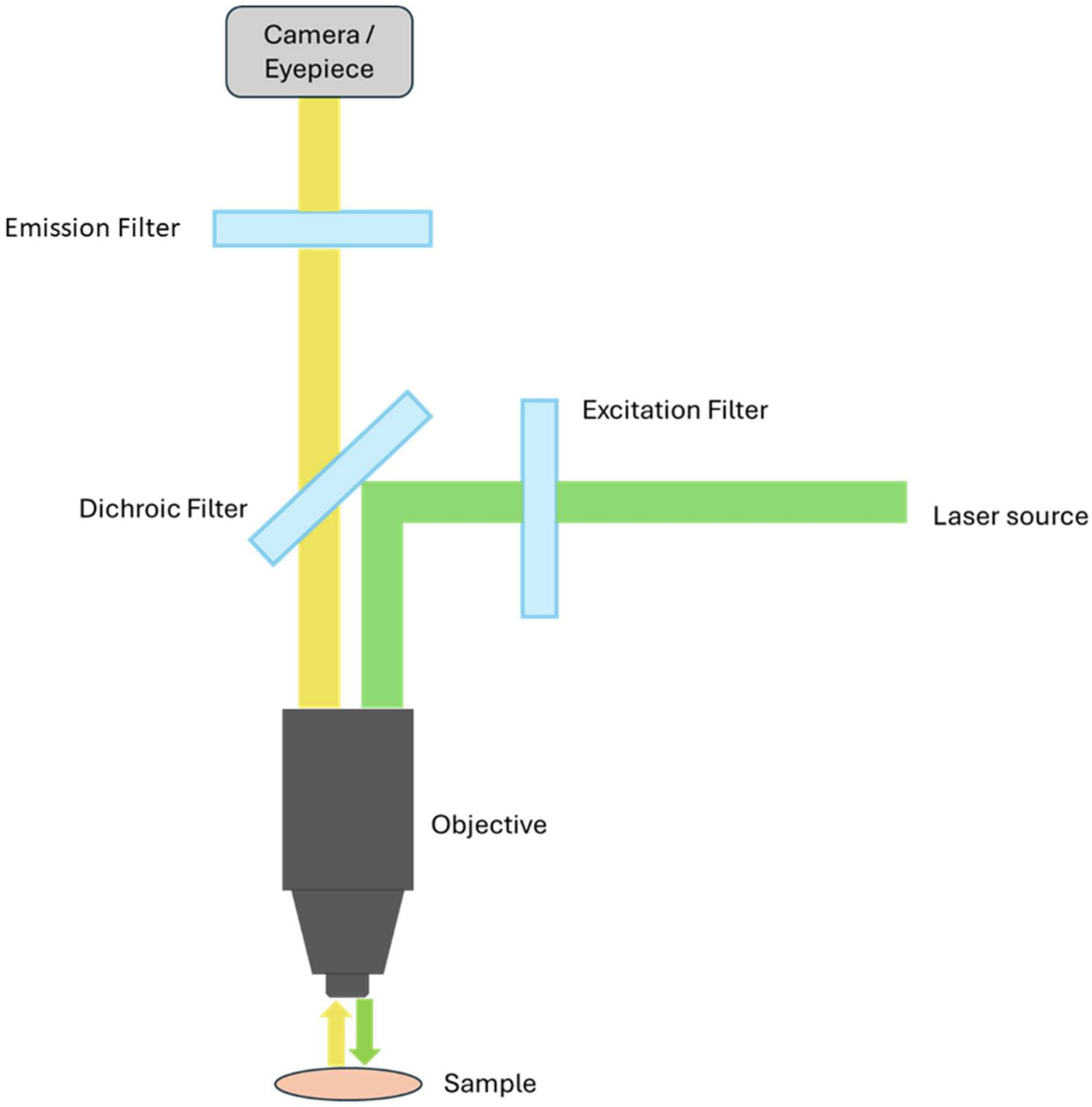

Figure 3. Epifluorescent widefield microscope schematic.

A development that was made to resolve this issue is known as confocal microscopy [21] . In its simplest configuration the confocal microscope consists of a lens that will collimate a laser beam, which will then travel through the beam splitter and overfill the back aperture of the objective lens. In this way only, a diffraction limited point of the sample's volume in the objective focal plane will be illuminated, conversely with the illumination method of the epifluorescence microscope. The emitted fluorescence from this point will be collected by the same objective lens. The beam splitter will propagate the beam towards a tube lens which will focus the emitted light through a pinhole that is placed in the back-focal plane of the tube lens in front of the detector.

The pinhole is positioned in a specified distance that will allow only emitted light from the focal plane of the excitation beam to reach the detector. Any emitted fluorescence from focal planes "above" or "below" of the focal plane focus before or after the pinhole. As a result, only a small amount of signal from those planes would reach the detector. Predominantly, signal from the selected single plane is captured making confocal microscopy a method of optical sectioning and highly reduced background fluorescence.

Confocal microscopy (Figure 4) is a highly controllable imaging system with high resolution and decreased background levels compared to the widefield microscope. A drawback is usually considered to be the speed of imaging as a single 2D image will require the combined lengthy process of point by point capturing and reconstruction, as well as low light efficiency as depending on the pinhole size a lot of fluorescence light will be blocked.

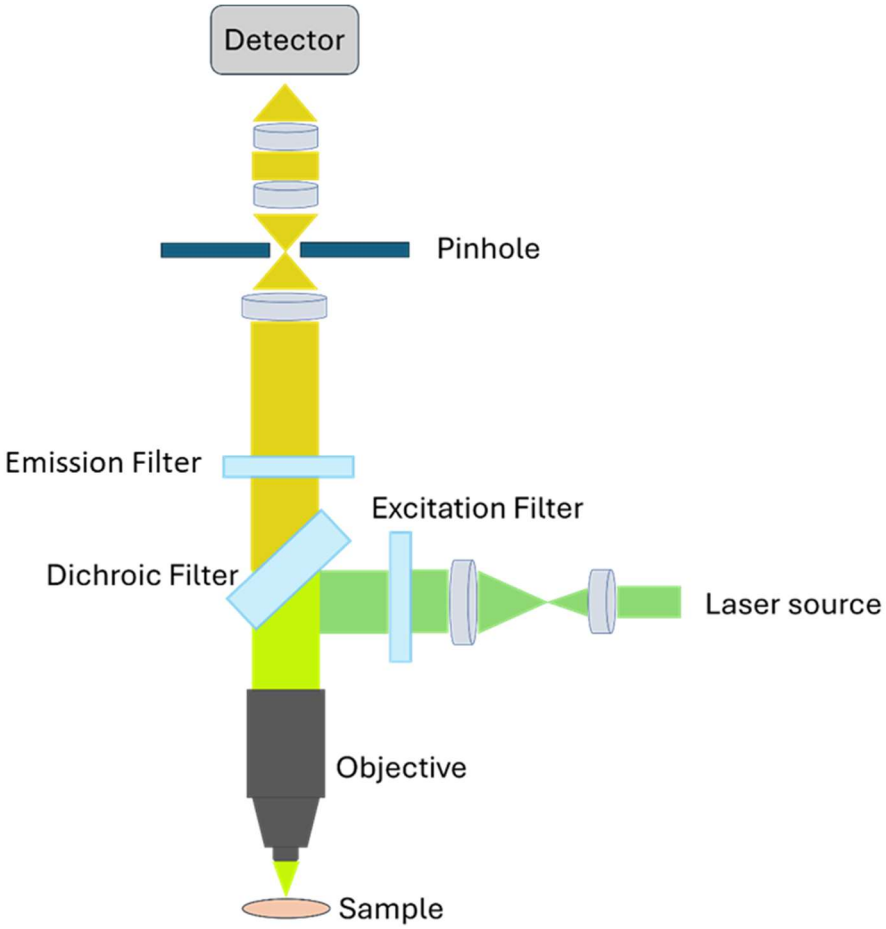

Figure 4. Confocal Microscope schematic.

2.1.3 Fluorescence Microscopy Considerations Related to Widefield Fluorescence and Confocal Microscopy

The main limitations in the use of the fluorescence imaging systems described so far can be summed up in three categories namely, high illumination power leading to photobleaching and phototoxicity, fluorescence signal and, imaging speed.

Photobleaching and phototoxicity

Photobleaching is the process under which a fluorescent sample will present a decay in their fluorescent intensity as a result of the interaction between the excitation light and the sample. The process of photobleaching is irreversible and the quality of imaging significantly decreases as the sample emitted fluorescence is gradually lost due to photooxidation of the dye [22]. All types of fluorescent microscopes suffer from this issue but it can be more prominent in specific setups. Widefield microscopy suffers from photobleaching extensively due to the illumination of areas of the sample that are not being imaged. The same though stands for confocal microscopy as even though the pinhole rejects fluorescence emitted from out of focus areas it will still illuminate them and cause photobleaching.

Another effect present in fluorescent imaging methods is phototoxicity. The term refers to the damage of a live cell during light exposure and whilst in contact with a fluorescent dye. The activated fluorescent dye interacts with components of the cell and causes permanent damage. Damage can range from loss of plasma to even a total death of the cell [23].

Fluorescence signal

A disadvantage that is mostly related to widefield fluorescence microscopy is the reduced quality of fluorescent signal that is collected as part of the system architecture. Since fluorescence light is collected from regions above and below the imaged plane, the result can be inconsistent in certain situations leading to blurry images. This can be attributed to the increased background signal from out of focus planes. It is fair to note that this issue is not prominent in confocal microscopy as one of its main features is to tackle out of focus fluorescence.

3D imaging speed

Considering the field of 3D imaging it is fair to assume that confocal microscopy is the most appropriate tool for the task as its ability to reject out of focus light from the not-focused planes results in high quality z-stacks. Z-stacks refer to the series of images that are captured in the different focal planes along the z axis of the sample and can be combined and used to reconstruct its three-dimensional structure. It is important to note though, that the collection of such data can pose limitations when it comes to time efficiency, especially for confocal microscopes. In order to produce a single 2D image, the microscope should collect information through point by point scanning of the plane as it has been stated in the relevant section. This limitation is further amplified in the event of live or dynamic imaging where the speed of confocal microscopes does not make them the default option. It is fair to note that certain technologies aim to bridge this gap and produce high speed acquisition in confocal microscopy. Those include laser scanning confocal microscopes and multi-point confocal techniques [24], [25].

Motivation for LSFM - low background, efficient illumination and faster 3D imaging

One can be led to the conclusion that the limitations of fluorescence microscopy are a result of the exposure to light and the uncontrolled way that this is usually implemented in the two main methods of epifluorescence, and confocal microscopy. This issue is further amplified when 3D imaging of larger volumes is needed and the sample is illuminated for a longer period. A need arises for a method that can achieve lower photobleaching, with reduced out of focus fluorescence implemented in significantly increased rate for 3D volumes. The method of LSFM achieves to perform comparably better in all these areas based on its fundamental configuration that is explained in the next chapter.

2.2 Light-sheet Microscopy

2.2.1 Light-sheet Introduction

As it has been briefly introduced previously light-sheet fluorescence microscopy (LSFM) is a method of fluorescence microscopy where imaging is a result of an orthogonal implementation of the illumination and imaging optical paths. Before

analysing the properties of LSFM in more detail, it is essential to define the terminology used for explaining the features of the light sheet and how they relate to the coordinate axes of the system. Throughout this work, the following conventions are consistently maintained: The z axis is associated with terms such as width, depth, or thickness of the light sheet. The y axis corresponds to the height of the light sheet. The x axis represents the axis of propagation for the light sheet. This standardized terminology ensures clarity and consistency in describing the spatial characteristics of the light sheet throughout the subsequent analysis. The imaging area of LSFM, and its comparison with the aforementioned microscopy methods, can be seen in Figure 5. Considering the different geometries implemented in each type of microscope it is possible to understand LSFM is able to achieve both lower illumination exposure and higher 3D imaging rates. Specifically, in LSFM the illumination is independent from the detection path and is oriented in an orthogonal direction to the detection path. In this way, only a thin section of the sample is illuminated, causing fluorescence emission from only this plane and allowing the detection optics to directly collect the information from only this section and form the image of the plane using the whole pixel count of the camera. This is the reason that LSFM is also known as single plane illumination microscopy (SPIM). The thickness of the planes is defined by the light-sheet thickness. In contrast, both widefield and confocal microscopy have a coupling between the illumination and detection path increasing the potential of photobleaching and phototoxicity of the undetected areas of the sample as it has been described previously [26]. LSFM manages to preserve the fluorescence ability and increase the sample lifetime [27], [28] due to its true optical sectioning power.

Furthermore, as LSFM does not illuminate out of focus planes it will inherently avoid blurring effects caused by background signals, with its axial resolution being limited by its light-sheet width in most cases.

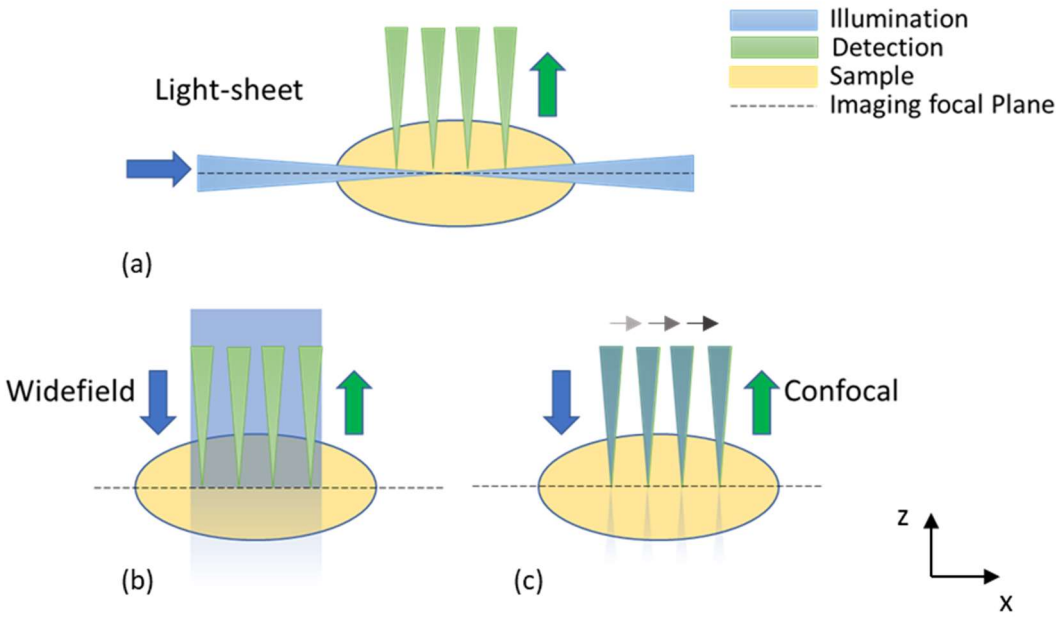

Figure 5. Comparison side view schematic between light-sheet, widefield and confocal microscopy. It includes the illumination and detection direction of each implementation. (a) LSFM: Illumination of a single thin line in an orthogonal configuration allows for direct detection of the whole plane. (b) Widefield microscopy: Same axes orientation for illumination and detection paths with the fluorescent information being detected from the illuminated plane that is in focus. (c) Confocal microscopy: Point scanning method of illumination with the illumination of one point being followed by the detection in the same axis. The same process is repeated unit all points that form a plane have been acquired.

The same can be said for imaging rates for 3D imaging. Confocal imaging has been the base method used for volume imaging by biologists for years [29] as it is able to discriminate depth with its pinhole rejection method when compared to widefield microscopy [30] . LSFM in comparison not only manages to image 3D volumes successfully [31-33] but it does that with imaging speeds that are up to 3 orders of magnitude higher when compared to a confocal microscope [34-36] with potentially even up to 6 orders if the technique wasn't limited by the camera and hardware acquisition speeds [37]. To provide a better understanding of the reason behind the speed one must again observe the fundamental difference in the image acquisition methods of each. In confocal microscopy imaging speed is defined by the scanning method used in order to acquire all points that form the imaging plane followed by successive scanning of further planes until the desired volume is imaged. In a LSFM scan, a single plane is already detected, and the total time of imaging is defined by the

method used to achieve the consequently staggered focal planes that form the desired imaging volume.

2.2.2 Implementations

All the above come to signify the importance of LSFM as an imaging method for biologists when it comes to 3D imaging. It is important at this point to present the two main implementations of the LSFM geometry based on the light-sheet generation mechanism. Focus will be given to different examples of each method presented in the literature and what differentiates the two based on their features.

Before analysing the different methods used in producing the light-sheet in LSFM it is important to define the characteristics of the beam propagation in the FOV as it is illustrated in Figure 6. For the example for a Gaussian beam [38] the minimum light-sheet thickness will be equal to the half-width of the beam waist w:

$$2w = \frac{\lambda}{\pi\theta} = \frac{2n\lambda}{\pi NA} \tag{1}$$

Where θ is the divergence angle, n is the refractive index, λ is the wavelength, and NA is the numerical aperture of the lens/objective focusing the Gaussian beam (schematically shown in Figure 6). Also, the light-sheet thickness will in general be equal to the sectioning ability and as a result equal to the axial resolution of the microscope with $R_{axial} = 2w$. It is important to note that in practice some LSFM implementations can have a lower R_{axial} when imaging objectives with high NA are used [39].

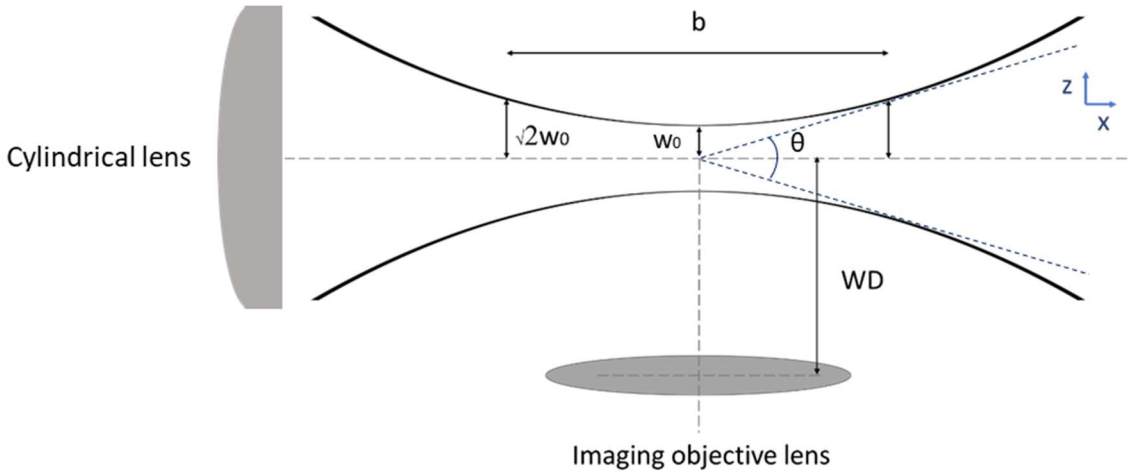

Figure 6. LSFM beam characteristics, where w_0 is the beam radius

The excitation beam width is usually measured in two ways. Beam diameter or *2w* is the measured width where the intensity has dropped to $1/e^2$ of the maximum intensity of a cross-section. Full-width-half-maximum (FWHM) is the beam width where the intensity has dropped to 50% of the peak intensity of a cross-section [40].

The confocal parameter *b* is a measure of the beam focus. Specifically, confocal parameter is the distance between the two points of the Gaussian beam where the beam waist increases by a factor of √2 relative to the minimum beam waist at the focus. The distance in x between one of the two points and the centre is defined as Rayleigh length and is equal to half the confocal parameter with $z_R=b/2$. At the same time the distance between the imaging objective and the centre of the light-sheet thickness is known as working distance, and it is the distance from the objective lens to its plane of focus. Commonly in LSFM the confocal parameter may represent the usable extent of the light-sheet as the intensity drops faster after this point as a result of the sudden beam waist increase. In theory the Rayleigh range relates to the beam waist radius with the following equation

$$zR = \frac{\pi w^2}{\lambda} \tag{2}$$

The relationship between z_R and *w* reveals that light-sheets with smaller thickness will have a large beam divergence and as a result the usable sectioning thickness will be limited along the propagation axis. At the same time the usable light-sheet thickness

may be increase with a cost of the sectioning ability of the instrument. This is an important trade-off that one must make in the design concept of the microscope and is usually one that is determined by the application that the microscope is intended for.

2.2.3 Single Plane Illumination Microscopy and Digitally Scanned Light-sheet Microscopy

The two fundamental established methods for generating the light-sheet are with either the use of a cylindrical lens (SPIM) or by implementing a rapid scanning beam in the illumination path, (DSLM – Digitally Scanned Light-sheet Microscopy). A simplified schematic of both is presented in Figure 7.

A cylindrical lens has a different radius of curvature (ROC) between the x and y axes and typically is flat in one of the axes. In this way during propagation of the beam only one axis will be focused with the result resembling a line focus effect rather than a point focus observed in spherical lenses. In the simplest configuration of SPIM the cylindrical lens is utilized for shaping the light-sheet before it enters the illumination objective [10] with the height of the light-sheet being determined by the focal length ratio of the cylindrical lens and excitation objective as well as the incoming beam diameter. A drawback of SPIM is that in its simple form the illumination is uneven as a result of beam scattering and shadowing when the beam travels through the sample. An implementation of SPIM with two oppositely placed illumination objectives was introduced to tackle this issue [41]. Even though it manages to reduce the undesired effects of non-uniform illumination it is considered a difficult method to practically implement in terms of optical alignment [42].

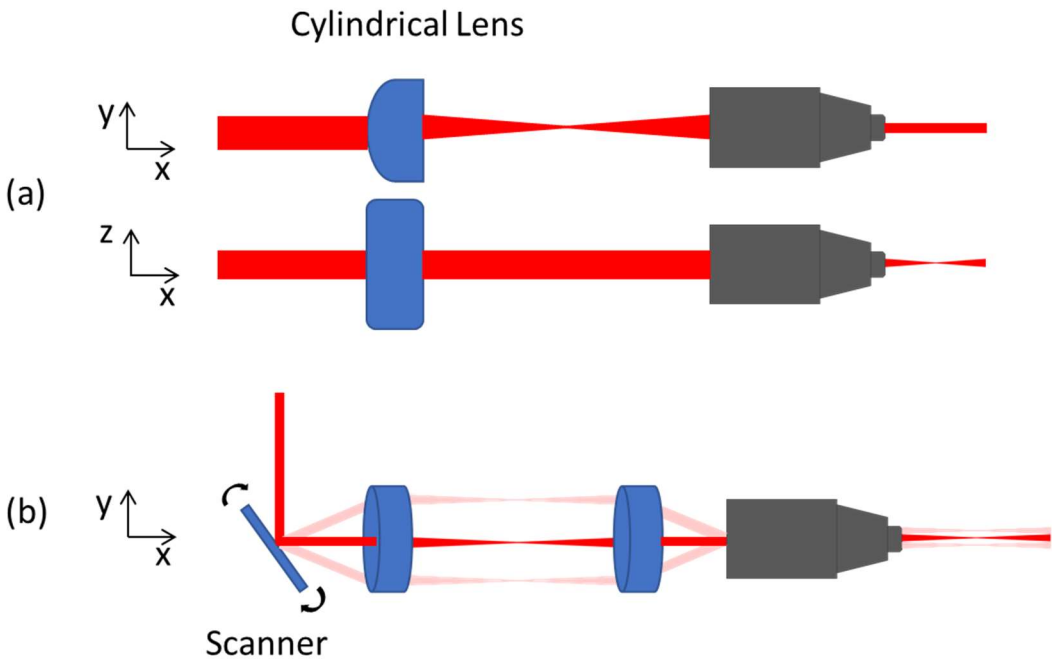

Figure 7. (a) SPIM implementation schematic. The beam is focused into a line. Entering the back aperture of the objective only one axis of the beam is focused creating a thin light-sheet at the sample area. (b) DSLM schematic using a scanning mirror. The beam reflects the fast-rotating mirror. The scanned reflection of the beam is collimated and focused by the objective to create a scanned light-sheet.

An alternative to the use of SPIM is DSLM that manages to offer significant improvements in areas such as control, scalability, illumination and axial resolution. In its first design [43] the DSLM managed to achieve an illumination efficiency of 95% compared to the 3% in SPIM. In DSLM a scanner element is used instead of the cylindrical lens for shaping the light-sheet. As a result, a line profile is formed due to rapid scanning to illuminate a full imaging slice at least once per camera exposure. The most frequent implementation of this method is accomplished with the use of a galvanometric mirror [38]. This methodology opened the door to the use of exotic beams as illumination sources, in methods of improving the illumination either with the use of Bessel beams [44], [45], Airy beams [46] and even moving to lattice light-sheets [47]. The use of these methods not only allows the reduction of the light-sheet intensity drop as it travels through the sample but provide a higher uniformity of the light-sheet thickness over a given FOV and as a result of the axial resolution of the light-sheet in the z direction. The main issue with these methods is the inevitable creation of sidelobes. The sidelobes increase in thickness as the beam propagates and

can cause illumination of parallel planes leading to unwanted fluorescence background and blurring.

Additional ways to create thinner light-sheets over a larger field of view have been implemented with different methods to axially scan the Gaussian light-sheet focus and acquire images where the light-sheet focus is swept across the FOV. This effect creates a uniformly thin light-sheet that does not suffer from the sidelobe illumination of techniques like the Bessel beam microscope systems. Different ways to achieve this active sweeping include the use of tunable acoustic gradient TAG lenses [48-50] in the illumination path of the microscope, as this type of lens can operate fast in the μs range. Another device that has been used in achieving the sweeping of the light-sheet is the spatial light modulator (SLM) [51],[52]. In the SLM implementation tiling is used to achieve this sweeping as the device is not as fast as the TAG lens and can operate in the ms range. While TAG lenses are faster, SLMs are usually less expensive and can be obtained as off-the-shelf products from a range of suppliers. Deformable mirrors [53], piezoelectric mirrors [54] and galvanometric scanners [55] have equally been used for this field of axially scanned light-sheet microscopy. Next to these, tunable lenses are also off-the-shelf products, even more affordable than SLMs and have been successfully used in the sweeping of the light-sheet focus for homogenizing the light-sheet width in different implementations. This has been possible by enabling the rolling shutter [56], [57] operation of recent scientific cameras and using it as a virtual slit that is synchronized with the illumination focus. Compared to the previously mentioned devices, the ETL (Electrical Tunable Lens) has been documented as an easier way to integrate, to existing LSFM setups and upgrade their illumination capabilities.

2.2.4 Methods for Imaging in 3D

Resolution

Even though illumination inevitably receives most of the attention in LSFM, it is still important to analyse the imaging characteristics and methods employed when it comes to 3D imaging.

The imaging path of the LSFM in its simple configuration consists solely of a finite conjugate microscope objective and the camera of choice. As a result the lateral resolution is defined by the diffraction limit with Abbe's equation [38].

$$\Delta x, y = \frac{0.61\,\lambda}{NA} \tag{3}$$

Where λ is the emitted wavelength and NA is the numerical aperture of the imaging objective. From this equation it is possible to see that the minimum lateral resolvable distance can be achieved with a high NA objective for each emission wavelength. Even though the technology of objective lenses has evolved, and high NA lenses are becoming common, in most cases they will come with a sacrifice on working distance. This sacrifice is quite an important one in the basic methodology of LSFM due to its orthogonal nature and the fact that two objectives with defined working distance have to be placed in very limited area during imaging. Lateral resolution signifies a field where LSFM aims to improve on, with different approaches of super resolution techniques already managing to do this with nanometre range results. The most recent techniques currently managing to be combined with light-sheet and achieve resolutions below the diffraction limit are namely, SIM (Structured Illumination Microscopy) [58], SMLM (Single Molecule Localization Microscopy) [59], and STED (Stimulated Emission Depletion Microscopy) [60]. It's important to note that these solutions often come with compromises such as the increased complexity of the systems.

3D Imaging

LSFM as explained previously manages to image a single plane as part of the orthogonal illumination. In order to image 3D volumes multiple parallel planes, have to be attained and reconstructed as a volume. As a result, several methods have been employed on how to achieve this vertical scanning with either mechanical, opto-mechanical or all optical configurations (Figure 8).

Specifically, in the basic implementation of LSFM the illumination and imaging objective are kept fixed within the system. An axial scanning stage was the preferred

choice in the earliest implementation of the orthogonal setup [8], and it was more recently enhanced by a rotational stage [10] (Figure 8 (a)). In both cases the sample gets mechanically displaced (or rotated) with the camera capturing every new plane after the rotation. The generation of the mechanical translation is usually in the form of a piezo motor. Even though this is still a valid method for accessing and imaging different planes of the sample, it provides certain drawbacks. When deciding to move the sample even in the smallest step one must accept the risk of damage or imaging aberrations that can occur due to its sensitive nature. Also, these methods can be slow compared to the high frame rates of cameras and lead to the limited capturing of dynamic events.

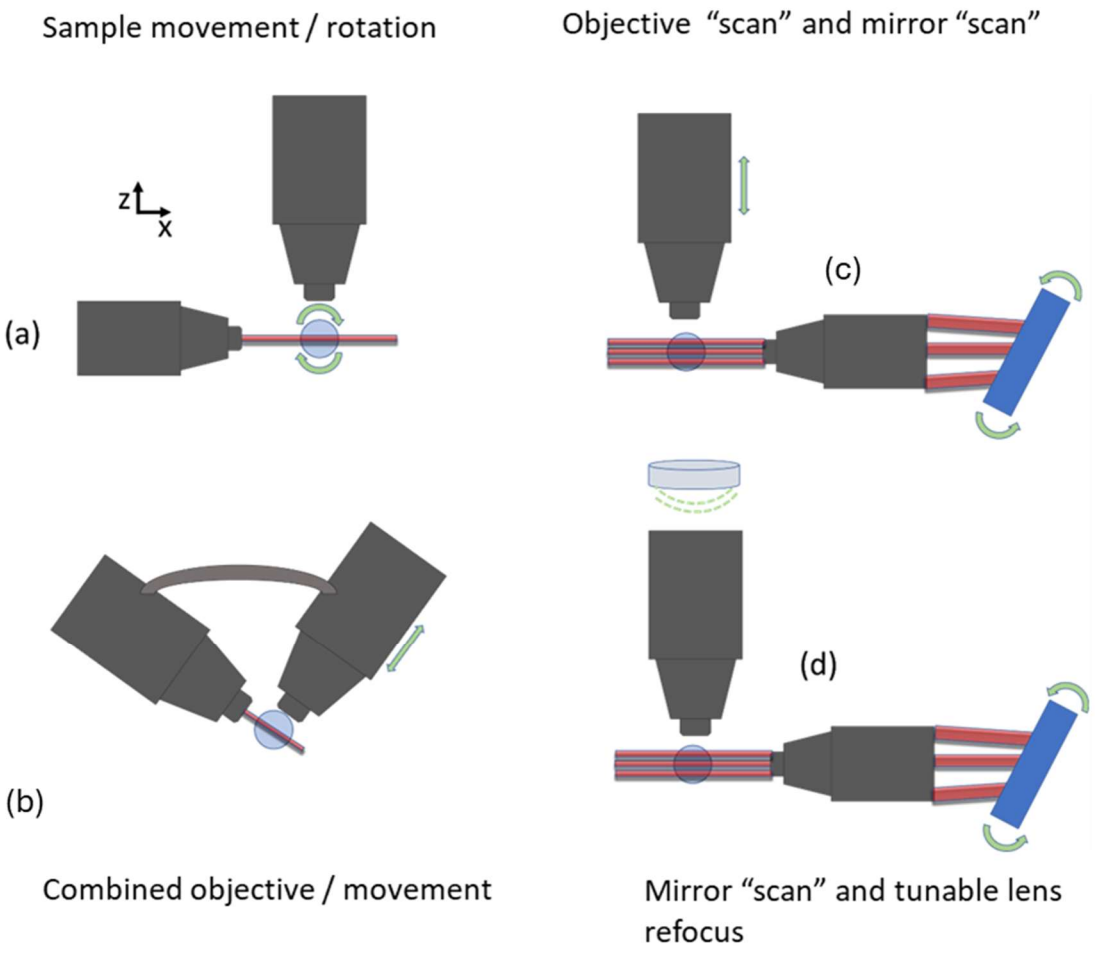

Figure 8. Simplified schematics of 3D imaging methodologies of LSFM. (a) Mechanical rotation of sample chamber. (b) OCPI coupled paths stage translation (c) Mirror light-sheet scanner and mechanical refocusing (d) All optical scanning.

The immediate alternative to a mechanical movement of the sample is keeping the sample at a fixed position while mechanically translating the illumination and imaging path in a synchronized way. This was first achieved with the method of OCPI (Objective-Coupled Planar Illumination Microscopy) [61] (Figure 8 (b)). The method couples the two paths on to a single stage and mechanically translates them providing the ability to image faster events. This method has been adopted and improved in terms of scanning speed and axial resolution [37]. The main drawback of this method was inevitably that heavy components ought to be moved in order to acquire a volume.

The use of a light-sheet scanning mirror (Figure 8 (c)) is introduced in some examples in an effort to reduce the mechanical movement of the light-sheet axis. In this method with the use of a galvanometric mirror the light-sheet gets translated parallelly whereas a synchronized movement of the mechanical objective stage refocuses the newly illuminated plane[62].

The main limitation that arises with the previously mentioned methods is to achieve even higher imaging rates as the mechanical stages used in the imaging path of the systems can be significantly slower than the capabilities of the camera. A few new methodologies aim to address this issue and introduce an optical scanning during 3D imaging. This includes again the scanning of the light-sheet but instead of a mechanical refocusing, a tunable lens is used to optically refocus to the parallel illuminated planes (Figure 8 (d)) [63],[64]. In a different approach to avoid the mechanical translation in LSFM the depth of field of the imaging objective is extended [53] with the use of wavefront coding. Finally, the remote-refocus approach [55] has been implemented in LSFM with the use of a mirror in a fast stage that reflects the intermediate captured plane that corresponds to the z position of the mirror.

Furthermore, of particular interest in the field of LSFM is the sample mounting techniques that can be used in 3D imaging. A well-known method is by embedding the sample in agarose [10], [65] or by using agarose in hollow cylinders [66]. Optically clear tubes FEP tubes are used [67], [68] to house a small concentration of agarose and allow for a more practical stage rotation of the sample.

It is important at this point to identify a distinction that has emerged in the field of light-sheet microscopy. A new class of systems is moving away from the traditional

orthogonal arrangement of illumination and detection axes described in the aforementioned examples. This shift aims to allow samples to be imaged in a more familiar and accessible manner, enabling the use of conventional sample holders such as microscope slides or petri dishes. This approach addresses practical limitations of traditional light-sheet microscopy, particularly in terms of sample preparation and positioning. The systems presented later in this thesis aim to occupy this space, along with several other implementations that have been developed concurrently or prior to this work.

The geometrical restrictions of LSFM can make this a challenging issue however several implementations like single lens [69] upright [70] or open-top microscopes [71], [72] manage to successfully image sample in more conventional ways. Other techniques that have made possible the imaging of sample in conventional configurations include the oblique plane microscopy approaches [73],[74] where the sample is again illuminated and detected by a single objective where the paths exit and enter at an oblique angle. In a similar configuration where the optical paths create an oblique angle the SCAPE (Swept Confocally Aligned Planar Excitation) microscopy [75] approach uses a scanning mirror to sweep the path across its depth for fast rate imaging. Finally, it is important to note that 3D imaging in LSFM does not come without drawbacks. A plethora of parallel planes need to be imaged for a volume representation. This usually results in huge data acquisition requirements, arguably making it one of the most important considerations of the system [76]. The terabytes of data require special imaging processing pipelines and efficient methods for image storage and processing [77].

2.2.5 Open and Versatile Light-sheet Microscopy

It is safe to say that LSFM research has made major steps in the last decade with a plethora of commercial systems now available (for example Zeiss Lightsheet 7 and Lattice Lightsheet 7, Olympus Alpha 3, Bruker SPIM series, 3i Marianas and Lattice, MSquared Aurora and others) along with the technologically advanced research grade solutions presented above. However, the commercial microscopes usually come at a high cost, and biomedical laboratories may not be ready to heavily invest yet in a

relatively new technology with the purchase of those systems. At the same time several LSFM methods that were presented required special mounting and preparation techniques for sample imaging, along with complex and expensive designs that understandably intimidates their reproduction and wide use. This led to several techniques that attempt to provide wider access to LSFM either through open protocols or with providing more simplified and versatile designs that can be repeated and used for a variety of purposes.

The open-access platform consists of OpenSPIM [78] (Figure 9 (a)), OpenSpinMicroscopy (OpenSpin) [79] and MesoSPIM [57] (Figure 9 (b)) . OpenSPIM provides scientist with all the necessary information to build and use their LSFM system. Through their website one can access buying lists, assembly instructions and software for the microscopy system. In terms of the actual working principle the microscope relies on the cylindrical lens for the shaping of the light-sheet while the majority of the components can be customized and upgraded based on the users requirements and even suggest more advanced LSFM designs [80]. The microscope uses both off-the-shelf components as well as 3D printed designs for custom solutions including the sample mount. OpenSpin on the other hands extends from the fundamental methods and provides the option for more versatile imaging. Two different illumination methods are provided one with the classical SPIM methodology and an alternative DSLM where the light-sheet is generated and scanned across the sample depth with a galvanometric mirror. MesoSPIM is also an initiative that provides open access to technical knowledge databases for building a LSFM system. The setup is specifically focused on large clear samples taking advantage of advance methods for imaging larger FOVs, such as the synchronization of the sCMOS (scientific Complementary Metal-Oxide-Semiconductor) camera rolling shutter with an illumination path ETL beam refocusing. The initiative is recognized for its results and is gaining popularity across labs worldwide with more than 20 such setups being active up to this date.

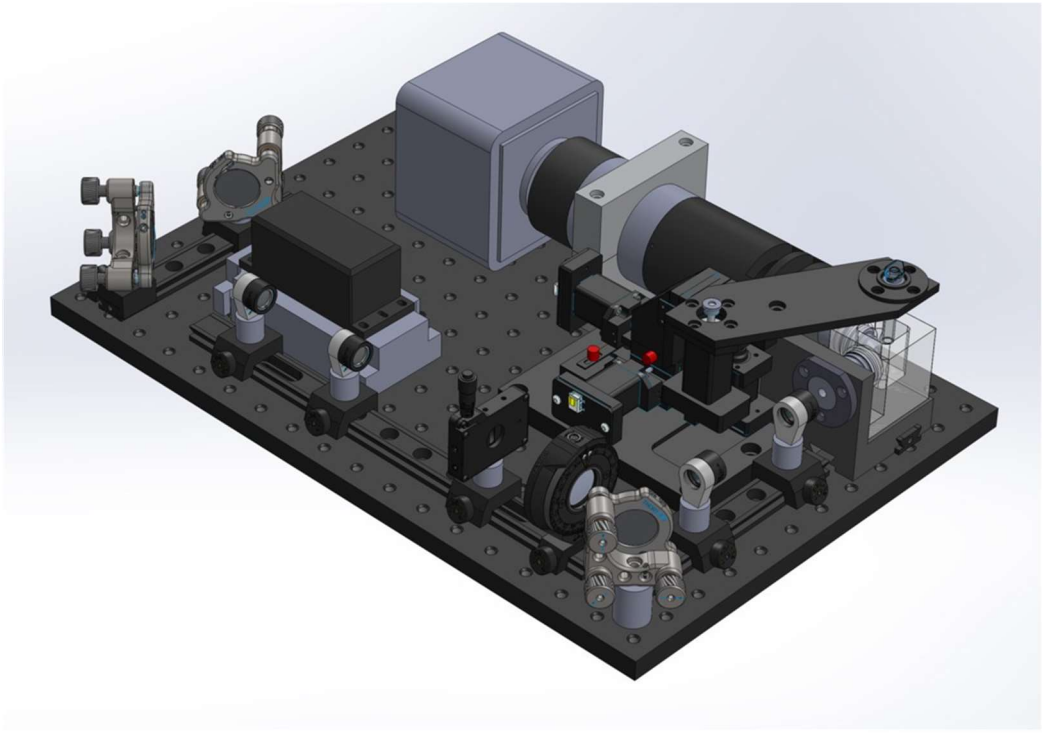

(a)

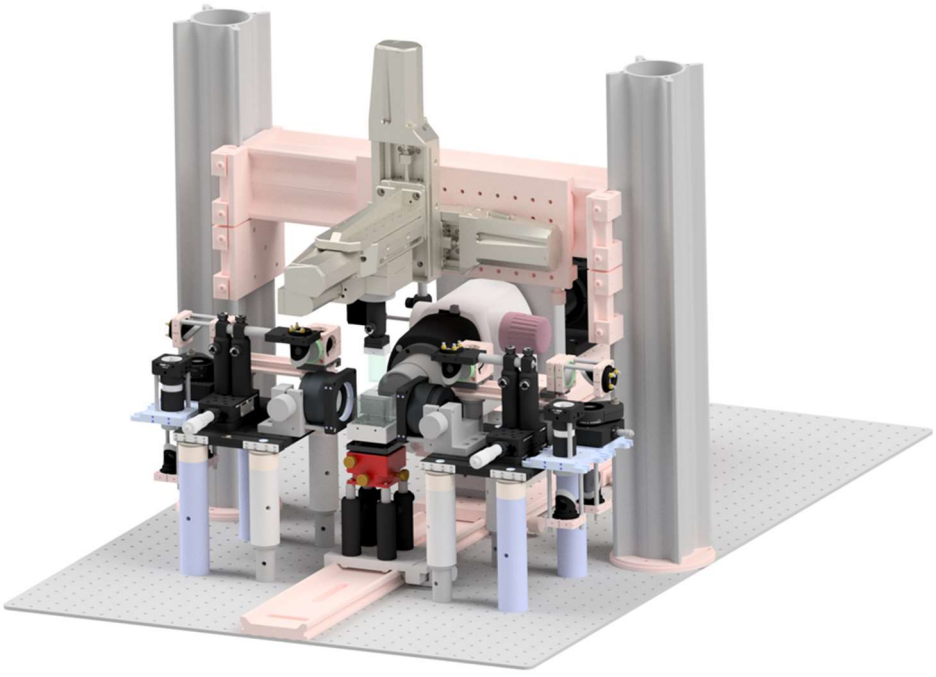

(b)

Figure 9. (a) OpenSPIM 3D design [81] with 300 mm x 450 mm footprint and (b) MesoSPIM 3D design [82] with 750 mm x 1100 mm footprint.

Even though the systems offer robust solutions for 3D imaging with LSFM they often come with certain limitations. Specifically, the cost remains still high (~ £100,000) for

being considered inexpensive. Additionally, mounting protocols can be considered a restriction for sample categories that are not intended to move during imaging. Finally even though the systems operate on an innovative and supported protocol users may find the alignment and use of the system challenging [83].

In other implementations the aspect of versatility takes a vital place in LSFM in an attempt to reduce complexities in the mounting techniques and relevant use limitation of systems. As mentioned in the previous chapter the departure from special mounting techniques have allowed LSFM to be used with a wider variety of samples [84], [85]. In the same spirit implementations are looking at multipurpose solutions [86] providing even greater versatility. Furthermore, LSFM research is trying to provide more compact systems that can be easily implemented in multiple environments. The miniaturization of the system can be a result of modification to the OpenSPIM platform [87] or with an implementation of a cylindrical mirror to a straightforward orthogonal setup [88]. Compact upright systems have also been reported [89] mounted on standard standalone breadboards. The use of 3D printing has also been explored as a solution to a smaller and more accessible LSFM systems [90]. Finally other reports have even attempted to walk one step further and couple LSFM on a smartphone imaging system [91].

It is important to note that the initiatives presented in this section served as inspiration for the development of the microscopy systems detailed in Chapters 4 and 5. Although the developed systems are not intended to be proposed as open-access microscopy setups, they follow a similar approach by utilizing a combination of off-the-shelf optomechanical elements and 3D-printed structures. However, it should be emphasized that these initiatives do not directly address miniaturization and cost reduction to the extent achieved by the systems developed in this work, nor do they offer the capability to image samples on standard microscopy slides. Comparably, the low-cost examples presented in this section, while innovative, lack the advanced optical scanning features explored in this work. Both developed systems push the boundaries of LSFM technology by incorporating novel scanning mechanisms and optimized optical designs, enabling high-resolution imaging of samples in conventional formats. This approach aims to bridges the gap between accessibility and advanced functionality in light-sheet microscopy.

2.3 MEMS Mirrors in Microscopy

Microelectromechanical systems (MEMS)

Current trends in LSFM research are moving towards solutions that are able to challenge the traditional mechanical stages that are used for 3D imaging. Minimizing the movement of the sample is a proven way of limiting potential damage to sensitive specimens while at the same time reducing optical artefacts during imaging. Furthermore, latest research outputs attempt to provide LSFM solutions in a more compact and affordable package making it a viable option for laboratories that are still considerate of the method. In this spirit MEMS and specifically MEMS mirrors [92] can play an important role in LSFM as active elements for both the generation of the light-sheet and control of the optical paths during 3D imaging.

MEMS (Microelectromechanical systems), after the name are small size devices that can relate an electrical power input into a mechanical output or vice-versa. They are very useful in today's industry and research in many fields such as sensors, medical technology and defence, due to the low cost, ease of manufacturing, convenient manual or automated control, and minimal energy needs. MEMS mirrors specifically have been an important tool in the development of small-scale imaging systems, and used for example as laser scanners, where the appointed light source is directed towards the MEMS. The MEMS then becomes an active part in the system as it will be able to reflect or redirect the light depending on the desired specification and intended application. MEMS mirrors can be divided into four different categories depending on their actuation principle namely, electrostatic, electromagnetic, electrothermal and piezoelectric [93]. Electrostatic actuation is one of the most common methods of MEMS design. Its operation is based on the forces that appear between two conductive plates once voltage is applied. Those forces cause the plates to move based on the geometrical constraints of the design. An example of electrostatically actuated mirrors is the comb-drive design [94] that uses an array of stationary and movable fingers to generate a fast mirror rotation. Electromagnetically actuated mirrors usually base their operation on two parts namely the magnet and the coil. In their basic configuration a coil is surrounding the mirror, whereas a permanent magnet is positioned beneath it [95]. Based on Lorentz force between the coil and the

magnet the mirror can rotate around the axis with high achievable maximum angles. Electrothermal MEMS mirrors work based on the principle of thermal expansion. The majority of MEMS is fabricated with semiconductor materials like silicon. While the current flow in silicon increases, this causes an increase in the temperature of the material in a phenomenon known as Joule heating. Sequentially the temperature causes the material to expand. This effect is being used in different type of actuation techniques such as the use of multi-beam silicon actuators that are constraint to rotate a centrally connected mirror [96], or with a bimorph configuration to create a varifocal optical element [97]. Finally, piezoelectric actuators take advantage of piezoelectric materials to create different strategies of mirror rotation. Materials like PZT [98] can be deposited on the MEMS actuators that surround the mirror and cause to rotate quasi-statically or resonantly. The theory behind this effect is based on the inverse piezoelectric effect where the application of voltage to piezoelectric materials causes them to expand or contract based on the polarity.

All the techniques mentioned above have been employed in research and industry for the design of MEMS mirrors, with the choice between them based on the advantages and disadvantages of each category [92], [99]. Specifically, electrothermal MEMS have restricted use in fast applications due to the few milliseconds needed for heating up the material, but are known to produce larger optical scan angles. In contrast, electromagnetic mirrors can generate both large angles and fast rotation with response times less than a millisecond. However, their use can be limited due to their bulky size, which can be up to 2-3 times larger than other categories, primarily due to the need for coils and magnets. Piezoelectric and electrostatic mirrors usually offer a balanced operation, producing moderate rotations with fast response times, generally less than a millisecond. These two types often provide a good compromise between size, speed, and scan angle, making them suitable for a wide range of applications. Table 1 summarizes achievable optical angles for each technology.

Table 1. Summary of average values [92] for selected 2D MEMS of different actuation technologies.

MEMS mirror actuation method	**Static Optical Angle (°)**	**Resonant Optical Angle (°)**
Electrothermal MEMS	21.5	21.9
Electromagnetic MEMS	59.05	33.9
Piezoelectric MEMS	13.7	21.4
Electrostatic MEMS	11	50.7

It is worth noting that the maximum achievable angles are not only a characteristic of the actuation method. The mechanical design of the actuators of the mirrors is considered equally a crucial factor for the generation of large rotations.

MEMS in Microscopy and biomedical imaging

MEMS mirrors have played an important role in biomedical imaging applications as they can replace bulkier and more expensive components in a pursuit of miniaturized and controllable systems. Various imaging systems use MEMS mainly for controlling an optical path or producing a resonance scan [100].

One of the first uses of MEMS in such systems is the MEMS scanner used in Optical Coherence Tomography (OCT) micro-endoscopes [101]. OCT is a technique for fast real time imaging based on interferometry of light beam scanning of biological tissue. This allows for the acquisition of high-resolution cross section images. The main application of OCT has traditionally been the imaging of the eye tissue but the endoscopic OCT has allowed imaging of many more parts of the body with examples ranging from gastroenterology and cardiology to urology and gynaecology. The use of MEMS in such systems is extremely beneficial as their small form factor allows them to be integrated in the endoscope, while their beam scanning capabilities has proved to be efficient for imaging. One of the first examples of this is with a single-axis rotating electrothermal MEMS [102] and later with the introduction of a 2D

electrostatic MEMS [103]. The latter configuration allowed an early view into the use of MEMS for in vitro 3D imaging.

The miniaturization features that benefit OCT devices have also been beneficial in the field of confocal microscopy. Even though MEMS type devices have been used as scanners in confocal microscopy from up to two decades ago[103-105] for laser scanning applications, their integration in miniaturized devices for in vivo studies has attracted more attention recently [104]. The miniaturization of the confocal microscope due to the use of MEMS has enabled its integration in endoscopic designs [105] and handheld devices[106]. Another field of microscopy that has benefited from the use of MEMS is that of photoacoustic microscopy (PAM). PAM is a technique that takes advantage of the formation of sound waves after light is absorbed from the sample. The use of a pulsed laser causes thermoelastic expansion to the tissue, generating an acoustic wave that can be detected by an ultrasound transducer [107]. The use of MEMS has been exploited to increase the efficiency of these devices by enabling a bigger area to be imaged at greater speeds [108]. The high speed of the scanners has enabled real-time in vivo imaging implementations [109] while the small size has contributed in the design of handheld PAM devices [110]. Finally, examples of MEMS use have expanded even to super-resolution microscopy techniques such as in structured illumination microscopy (SIM). In this implementation the use of three axis MEMS mirrors are used to control the interference pattern and phase of the microscope [111].

It is important to mention that MEMS in the form of digital micromirror devices (DMD) and adaptive optics mirrors have also been used in microscopy for different applications. This field will not be covered in this thesis as the device of interest is single mirror MEMS.

MEMS in Light-sheet Microscopy

Interestingly, even though one of the first available commercial LSFM system uses a MEMS scanner (Zeiss Lightsheet), its integration of the field is still limited. MEMS have seen use in LSFM mainly for axial manipulation of the beam providing a more isotropic resolution [112]. Conversely galvanometric mirrors have established themselves as the main optomechanical element for the generation and scanning of the

light-sheet in DSLM. This can be attributed to their wider availability and stability at the time of the development of the first DSLM systems. Nowadays, MEMS scanning mirrors become increasingly available by commercial distributors making them a more viable choice while their compact size and availability makes them a very attractive option. Specifically comparing the two, a 2D MEMS mirrors can be 5 times smaller than a 2D galvo with the overall cost between the most affordable options of each ranging in the same scale (~£500 vs ~£2500).

Prior to the work in this thesis an LSFM implementations with MEMS has already started to be considered as a miniaturization solution within the research group [113], with the initial approach for the illumination path shown in Figure 10.

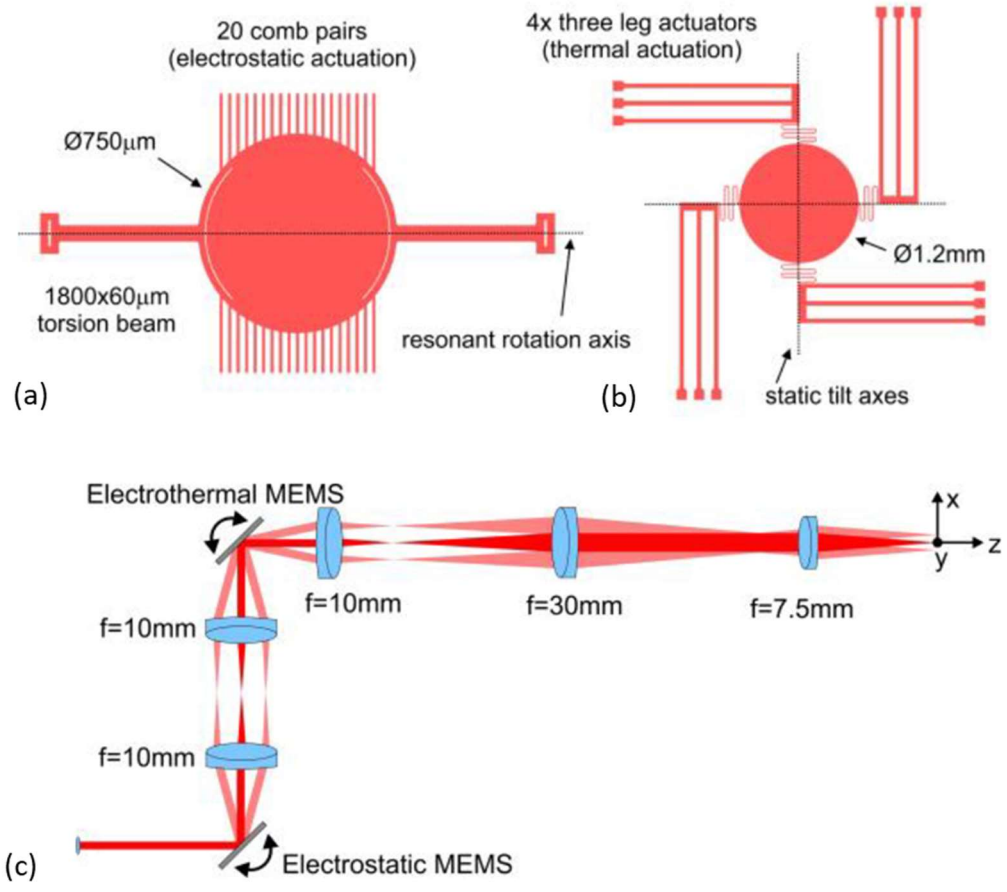

Figure 10. MEMS LSFM excitation system [113]. (a) Electrostatic scanning mirror for light-sheet generation. (b) Electrothermal mirror for light-sheet scan in depth (c) Miniaturized DSLM implementation.

One electrostatic and one electrothermal mirror are used in this case in order to produce a light-sheet and control its positioning. A fast comb drive electrostatic MEMS mirror is used to create the scan line coming from the 488 nm light source. The light-sheet is directed in an orthogonal direction where it can be further controlled with the use of an electrothermal mirror. The serpentine thermal actuators can achieve static angles of up to 4° and allow manipulation of the beam before it reaches the final focal plane. The setup can achieve a FWHM of 3.5 μm with high intensity throughout the 550 μm tall light-sheet. The work presented on novel MEMS enabled LSFM systems in chapters 4 and 5 is building on these initial concepts but makes use of only a single 2D MEMS to create and position the light-sheet simultaneously. This aims to reduce the complexity of the system by minimizing the number of optical elements needed.

2.4 Summary

This chapter aimed to cover the underlying principles of LSFM expanding on an introduction into fluorescence microscopy and the achievements that have taken place throughout the field in recent years. Specifically, the basic theory of fluorescence microscopy has been introduced through the concepts of absorption and emission wavelength in fluorescent molecules. The division between three different fluorescent microscope categories has been made under the fields of Widefield Fluorescence, Confocal Microscopy and LSFM. Emphasis is given on the limitations of the first two microscope types for certain settings and how LSFM can potentially assist to overcome those and present a fluorescent imaging tool with better contrast imaging, higher acquisition speed and reduced photobleaching. A more detailed background on LSFM is given from its early starts a few decades ago till more recent implementations of the orthogonal imaging setup. Different LSFM setups are presented in terms of the mechanism that generate the light-sheet as well as the components and methodologies that allow 3D imaging. A special mention is given on open access LSFM setups as an attempt to make LSFM a more accessible tool. The accessibility of LSFM can be further potentially aided with components that drop the cost and decrease the size of the system. MEMS are devices that are recognized to meet both of those requirements. Thus, a brief review of MEMS in microscopy is presented with examples ranging from

OCT to the early designs of a miniaturized LSFM system with MEMS as active elements in the optical paths. The evolution of this design will be discussed in detail in the following chapters.

3 Optical Elements and Custom Parts

In this chapter the individual optical elements required for building the miniaturized LSFM systems demonstrated in this thesis will be introduced. The design specifications of the elements are going to be presented along with a full characterization of their features. The analysis is made with a focus on exploring the capabilities of the elements as part of the imaging systems that will be introduced in the following chapters.

The fundamental elements behind the miniaturization of LSFM demonstrated in this thesis are the MEMS micromirrors. A two-dimensional micromirror is used for both the generation and lateral control of a light-sheet. Two different micromirrors are introduced in this section featuring different actuation techniques, with one being piezoelectrically actuated and the second one being electrothermally actuated. As introduced in Section 2.3, the choice of MEMS mirror is influenced by the actuation technology but ultimately depends on the specific project requirements. It is worth noting that at the early stages of this project, the market for single-mirror MEMS scanners was not as developed as it is today. MEMS mirrors were either integrated parts of devices or limited designs used in academia, which is the case for the 2D mirrors presented in this chapter.

The opportunity to integrate a 2D MEMS mirror instead of two separate MEMS mirrors (Figure 10) significantly narrowed the selection pool of possible devices. However, this approach offered several advantages, including improved miniaturization and cost reduction, the possibility of seamless control, and a reduction in the number of devices that need to be synchronized. These benefits indicated that pursuing a 2D MEMS mirror solution was a step in the right direction for our LSFM system.

Both 2D MEMS mirror devices characterized in this chapter fulfilled the initial requirements, with their respective features explored in the following sections. However, it is important to acknowledge that these choices are not without drawbacks. As discussed in this chapter, both MEMS mirrors suffer from non-linearity, which

must be addressed for successful operation of the system. This non-linearity is a common challenge in MEMS mirror design and often requires compensation through calibration, control mechanisms or post-processing methods. Compromises were also necessary regarding the maximum angles achievable on the two axes. In this case, the limitations of the devices directly define the limits of the final systems, as will be demonstrated later. This constraint highlights the importance of carefully selecting MEMS mirrors that can provide sufficient scan angles for the intended application while balancing other factors such as speed, size, and power consumption.

The micromirrors of this project are used in the same general position within each iteration of the light-sheet illumination path and the characterization will enable a direct comparison between the components in terms of their optical angles and positioning results.

In addition to the micromirrors, two different tunable lenses are introduced in this chapter which allow changing the focal position of the excitation or emission arm of the light-sheet systems. Both tunable lenses are commercial elements and feature shape changing technology, making them applicable to the refocusing requirement of the imaging path. Additionally, one of the tunable lenses will be used to vary the focus of the light-sheet focal position axially in the ASLM configuration introduced in chapter 5. Their main difference between the two tunable lenses lies in their clear aperture size. A full characterization of the lenses is presented in this chapter based on their technical specifications as well as further investigation regarding their use and applicability to the imaging system.

Finally, the 3D printed prism design, fabrication and characteristics are presented. The use of the prism aims to reduce imaging aberrations in an easy to implement and inexpensive solution.

3.1 Piezoelectric MEMS

3.1.1 Piezoelectric MEMS Design Characteristics

The active element used for the generation and control of the light-sheet in the Miniaturized LSFM setup presented in chapter 4 is a 2D piezoelectric (PZ) actuated MEMS (see Figure 11). The MEMS was developed by Stanley Inc in collaboration with Tokyo University. A set of six pre-production MEMS mirrors were provided for the microscopy work as an ongoing collaboration between the University of Strathclyde and Tokyo University. The MEMS is designed to achieve a 2D raster scan with the single 1100 µm diameter mirror surface, combining a static angular movement (slow axis) with an orthogonal resonant angular movement (fast axis). In this work the MEMS has been used in the excitation arm of a light-sheet system to scan and position a fluorescence excitation laser beam. The fast-resonant axis is generating the light-sheet while the slow axis is used in conjunction with a telecentric optical lens setup to enable the orthogonal translation of the light-sheet through the sample.

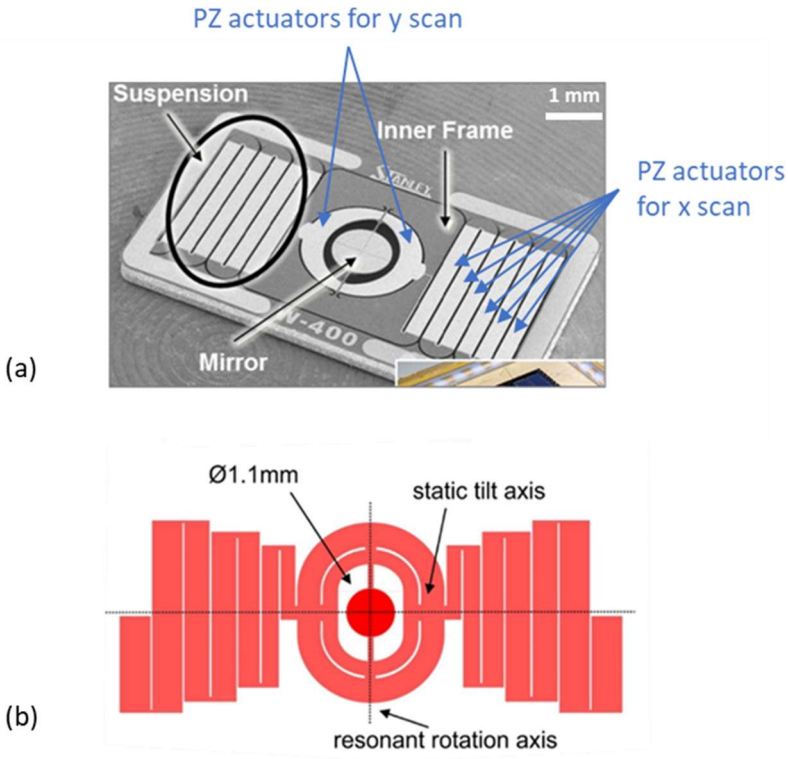

Figure 11. (a) SEM figure [114] and (b) top view schematic of the piezoelectric MEMS mirror.

The thickness of the device layer of the MEMS chip is 100 μm of single crystalline silicon with a top 2 μm thin PZT layer to enable piezoelectric actuation. The design expands with an oval shape actuator frame surrounding the mirror connected to the mirror perimeter by two torsion beams on opposite sides, around which the fast resonance movement is occurring. The frame has multiple piezoelectric actuators placed on its surface which allow separate excitation of the resonance movement. The MEMS is designed to enable a static movement through the spiral actuators connecting the frame to the chip substrate, while the inner ring frame is responsible for a fast-scanning rotation on the vertical axis. The mirror surface is coated with Al to increase its reflectance.

The piezoelectric actuators on the spiral arms are electrically connected so that only every second arm is connected to the same electrical wire bond terminal. This way a different polarity of actuation voltage can be applied to each subsequent spiral arm, which allows out-of-plane bending of subsequent spiral steps in opposite directions.

The underlying effect creating the bending motion is the inverse piezoelectric effect, which describes the ability of a piezoelectric material to convert electrical input to a mechanical change. For this device, the piezoelectric material layer of one serpentine section will be actuated so that it exhibits compressive stress while the neighbouring section's piezoelectric layer will be actuated so that it exhibits tensile stress. The combined mechanical stresses will create an ''upwards movement'' as is illustrated in Figure 12, where "Piezo A" refers to the actuators connected to one voltage terminal and "Piezo B" to the actuators connected to a second voltage terminal with opposite polarity. The methodology of utilizing actuators with opposing polarities can generate significantly larger angles of deflection. This is achieved through a complementary motion where, as one set of actuators moves upward, the actuators on the opposite side correspondingly move "downwards". The spiral-shaped actuators, being connected to the outer frame of the mirror, enable this frame to rotate around the main axis of the device. This rotational motion induces the static angle in the mirror. Such a design leverages the combined effect of both sets of actuators, resulting in a larger total angle of rotation compared to single-polarity actuator configurations.

The inner ring frame surrounding the micromirror is also designed to induce a rotation due to the piezoelectric effect. In contrast with the spiral actuator, the inner ring is set to rotate during its resonance and as a result enable a continuous fast sinusoidal rotation. The oval shape of the frame defines the rotation axis as it allows for motion orthogonally to the static angle. The connection torsion beams attaching to the mirror on the opposite sides of the oval length will increase the minor resonance tilt of the inner frame. As a result, the full resonance of the mirror gets amplified producing larger angles along this axis [115].

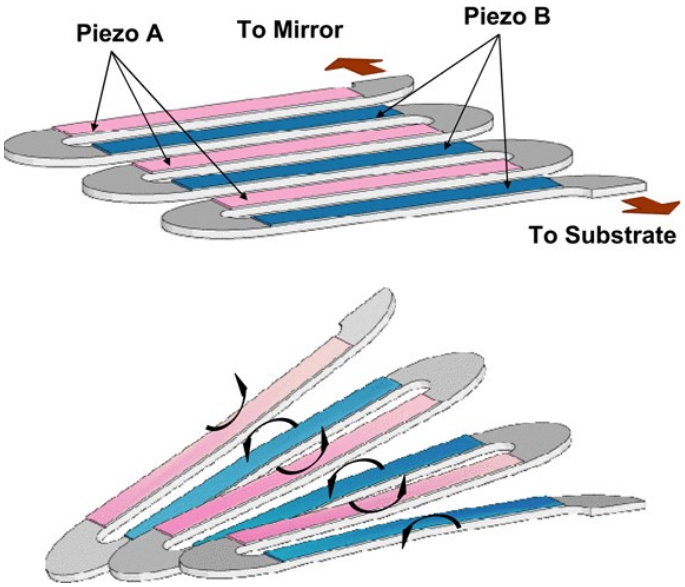

Figure 12. Working prinicple schematic of the spiral actuators for the piezoelectric MEMS mirror.

The mirror was characterized for its surface quality with an optical profile surface measurement illustrated in Figure 13. The surface profile evaluation was accomplished in cleanroom settings with a VEECO NT1000 optical surface profiler. The instrument works as a white light interferometer where the surface shape and roughness of an object is measured based on Michelson interferometry configuration [116]. Specifically, the light emitted from the instrument's light source is separated with a mirror into a reference beam and a measurement beam. The reference beam is reflected of a fixed mirror while the measurement beam is reflected off a movable mirror towards the test object. Both beams are reflected back to the devices detector where they are brought to interference. The interference patterns are captured by the detector,

while the software will interpret it into a complete surface topography dataset. The measurements taken for all the surface profile datasets that are presented in this thesis have been captured with the VSI (vertical scanning interferometry) mode with a 2.5x magnification objective. During a VSI scan [117] the objective moves vertically to image the whole height surface difference of the sample with the speed defined by the cameras frame rate. During each scan the camera pixels will collect the interference fringes that occur in the specific area of the sample. The fringe contrast for each pixel is measured, enabling the mapping of the surface topography.

The MEMS mirror manages to incorporate a practically flat surface with overall fluctuations not exceeding ± 0.03 μm (better than λ/10 surface flatness for the visible). The radius of curvature of the mirror is in the range of 20 meters, according to the measurement provided by the Veeco profiler software.

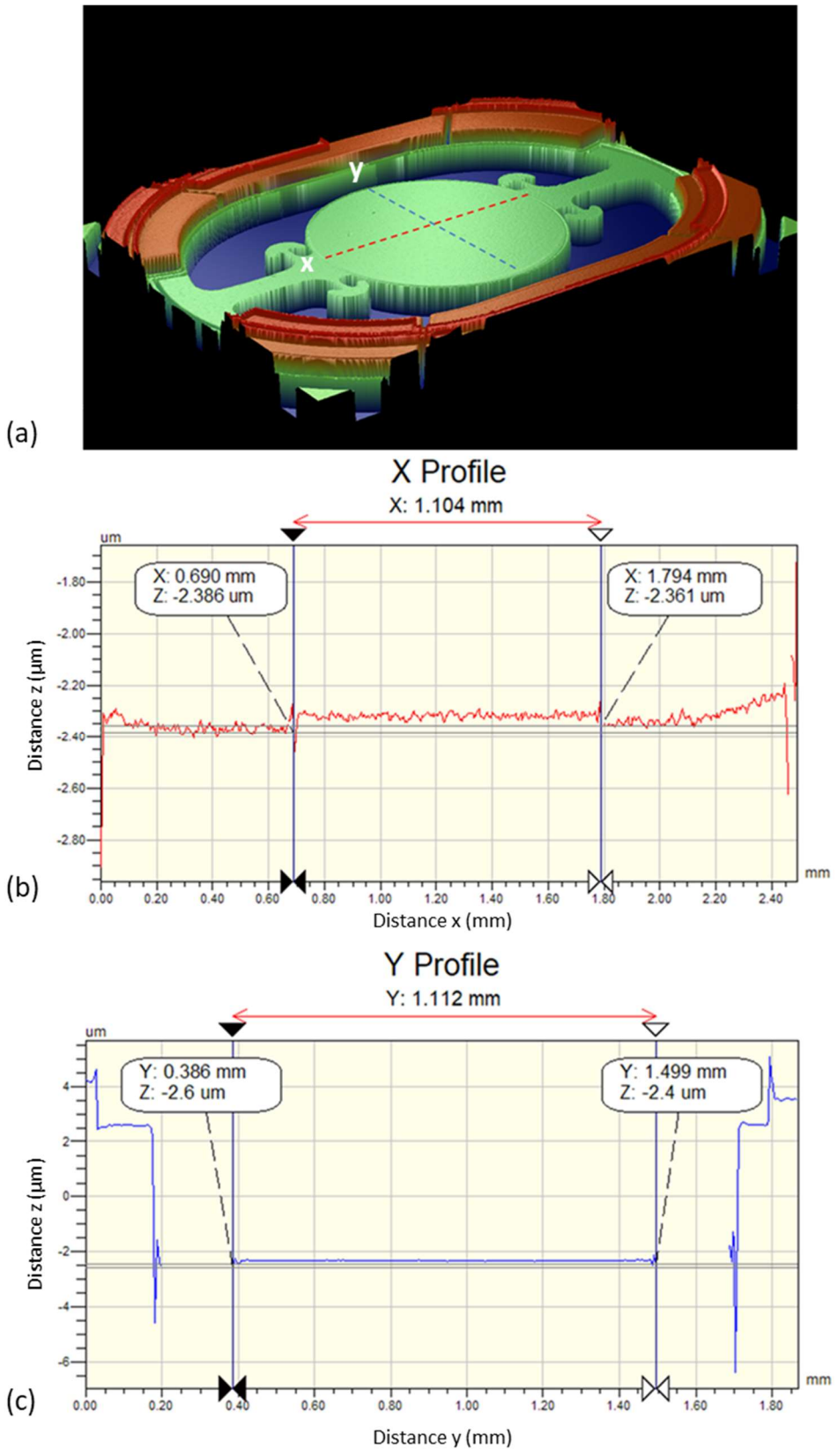

Figure 13. (a) Surface profile 3D schematic along with diagram of the surface height variation along the centre of the mirror. The red and blue dotted lines indicate the x

axis and y axis respectively. (b) The x axis profile plot with the step variation presented, revealing the coating layer of the device and (c)y axis profile plot with the large step increase in the edges revealing the actuator layer surface height relevant to the mirror surface. In both axes the roughness of the mirror did not exceed 0.025 μm.

3.1.2 Piezoelectric MEMS Angle Characterization

The mirror is characterized for its total optical scan angle (TOSA) for both the slow and fast axis. The experiment is set up with a laser source being reflected off the mirror surface and projected onto a screen (Figure 14). The laser source is positioned 5 cm away from the mirror. The distance between the mirror and the screen is 50 cm. The displacement of the laser reflection with varying actuation voltages is measured on the screen using a ruler. The change in coordinates on the screen following an actuation of either MEMS axis can be translated to the TOSA by applying the geometrical formula:

$$TOSA = tan^{-1}\left(\frac{l}{d}\right) \tag{4}$$

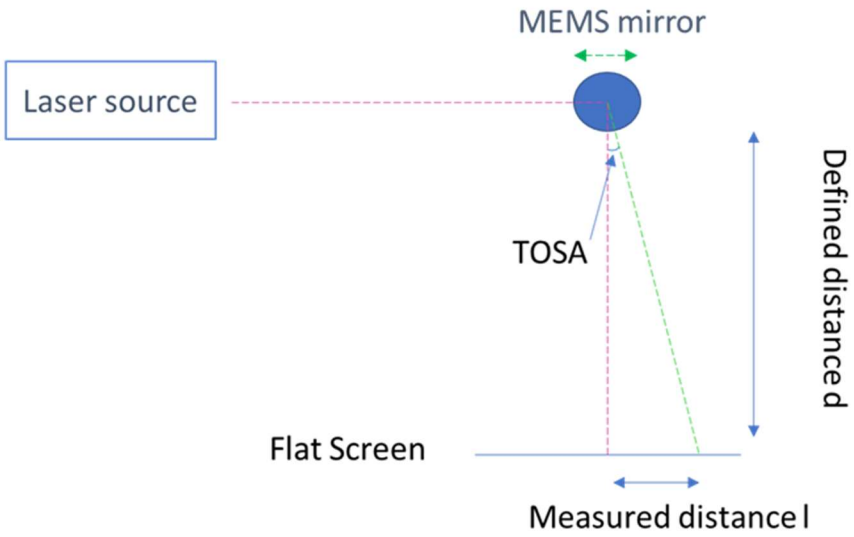

Figure 14. Schematic of test principle used in characterizing MEMS angle using a reflected beam. Measurement of Total Optical Scan Angle (TOSA) based on the on the reflection offset recorded on a flat screen.

The recorded TOSA for the slow axis is illustrated in Figure 15. A DC voltage ranging from 0 V up to a maximum of 20 V was used sequentially for the two piezo terminals of each serpentine actuator, actuating only the two terminals on opposite sides of the chip that create the same movement direction at any given time. It was found that after the 20 V maximum voltage the PZT layers of the device may suffer structural damage due to electrical breakdown. In the case of negative voltage inputs, it was found that the layer damage occurred with significantly smaller values. As a result, all of the characterization and use of the MEMS in this work is a product of positive input voltage. The graph shows that the response of the static axis follows a similar trend in both angular directions reaching a maximum of 1.5° for each direction and 3° combined. The response time of the MEMS has also been characterized using a quadrant diode detector by colleagues at the University of Strathclyde. The input response time is measured as <1ms during actuation of the static angle with a step voltage of 0.5 V.

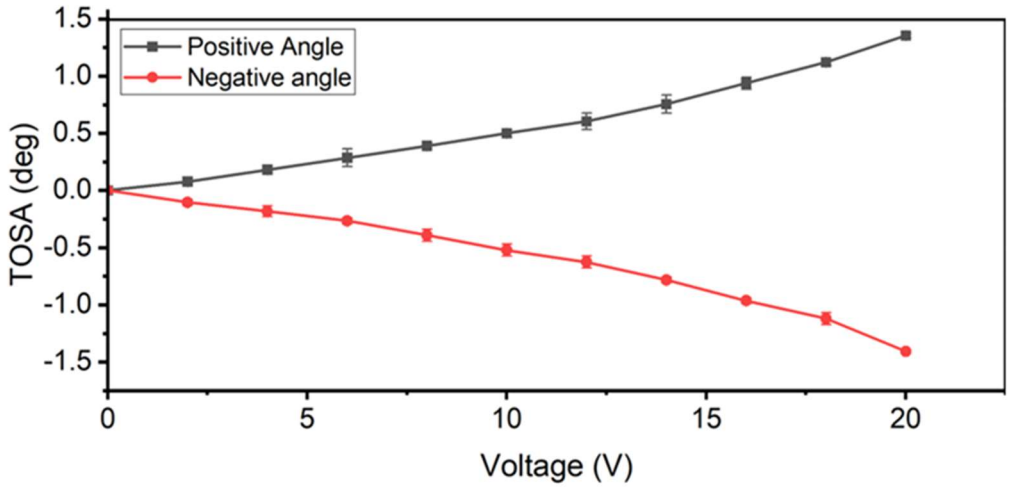

Figure 15. Static angle characterization of PZ MEMS for positive and negative angles.

The characteristic of the fast-resonant axis is illustrated in Figure 16. Resonance angle characterization of piezoelectric MEMS.The response of three diferent voltage inputs are illustrated namely, V1in=10 V , V2in= 15 V and V3in= 20 V with respective resonances at f1=36.805 kHz f2=36.801 kHz and f3=36.795 kHz. The resonant angle is measured for a set of three different sinusoidal voltage inputs namely, 10 Vpp, 15 Vpp and 20 Vpp. All waveforms are set to a voltage offset equal to half the amplitude in order to avoid a negative voltage input. A frequency sweep from 36.73 kHz to 36.88

kHz in 5 Hz steps was used. The maximum resonance tilt movement of the mirror occurs at the excitation frequency of 36.8 kHz for the 20 Vpp input with the maximum scan angle of 27°. It is also observed that the maximum angle point for each increasing voltage input is located in a lower frequency point indicating a non-linear behaviour, while no hysteresis is observed for the described actuation range. Hysteresis in a resonant scanner becomes more prominent at high voltages that exceed the maximum allowance of this device. As noted in the case of MEMS scanners [118], spring softening during resonant actuation can cause nonlinearity issues, as the response adopts a different profile depending on whether the eigenfrequency is approached from lower or higher frequencies. Fortunately, none of the scanners used in this thesis exhibit this issue within the operational limits of their characterization.

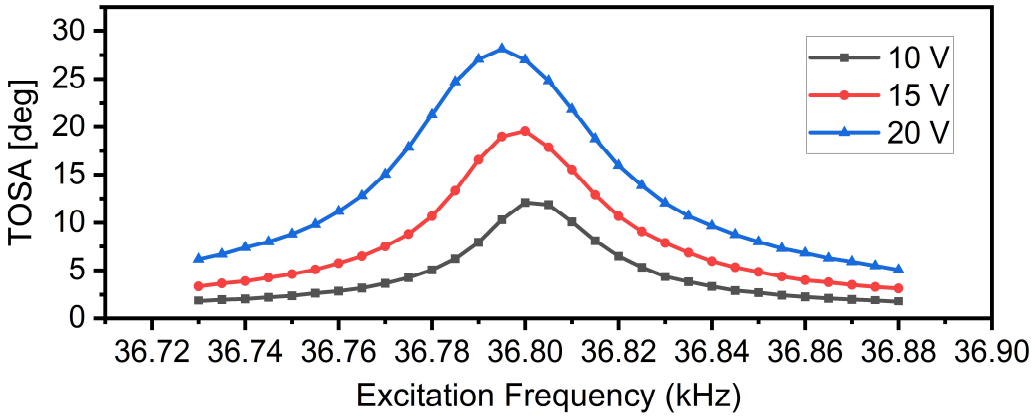

Figure 16. Resonance angle characterization of piezoelectric MEMS.The response of three diferent voltage inputs are illustrated namely, V1in=10 V , V2in= 15 V and V3in= 20 V with respective resonances at f1=36.805 kHz f2=36.801 kHz and f3=36.795 kHz.

3.2 Thermal MEMS

Considering the MEMS device as the sole tool for laterally translating the light-sheet, a limitation may be arising with the limited angle range of the PZ MEMS static rotation. In this section, an alternative MEMS design will be introduced with larger static rotation angles. A 2D electrothermally actuated MEMS will be used in a second LSFM design will again be responsible for the generation of a scan line and orthogonal

positioning of the light-sheet, while also allowing the potential for a static offset in the resonant axis.

3.2.1 Thermal MEMS Design Characteristics

The electrothermal (ET) actuated mirror is illustrated in Figure 17 (a). The design has a 1.4 mm diameter mirror surface which is surrounded by four actuators with a three-beam geometry. The beams are spaced with a 50 μm distance between them. The design features a slight variation in the actuators beam length between actuators on orthogonal axes. Specifically, the pair of actuators that are on opposite positions of the perimeter have exactly the same length of either 1800 μm (x axis) or 1700 μm (y axis). The 100μm change is expected to separate the eigenfrequency of the two orthogonal rotation axes and limit off-axis movements during the fast rotation of the mirror [96]. A connecting beam with length equal to 450 μm and width equal to 60 μm connects the actuator design to the 1.4 mm diameter mirror via a serpentine spring. The design enables a voltage to be applied to the two outer beams of the chosen actuator. The electrical current that passes through the two beams will cause Joule heating and cause them to thermally expand. The constrain created by the connecting beam in conjunction with the electrically isolated and therefore un-heated central beam will cause an out-of-plane movement to the mirror through their connection as is illustrated in Figure 17 (b). The out-of-plane movement of the actuators translates to a rotation of the mirror surface.

The four actuators can be used either for a static or resonance rotation depending on the input voltage signal, providing both 2D control and scanning capabilities in one device. When compared to the PZ mirror, the thermal MEMS does not incorporate a similar dedicated resonance actuation technique. In contrast, eigenmode resonance movement can be achieved by actuating the static actuators of the desired axis at the relevant device eigenfrequency.

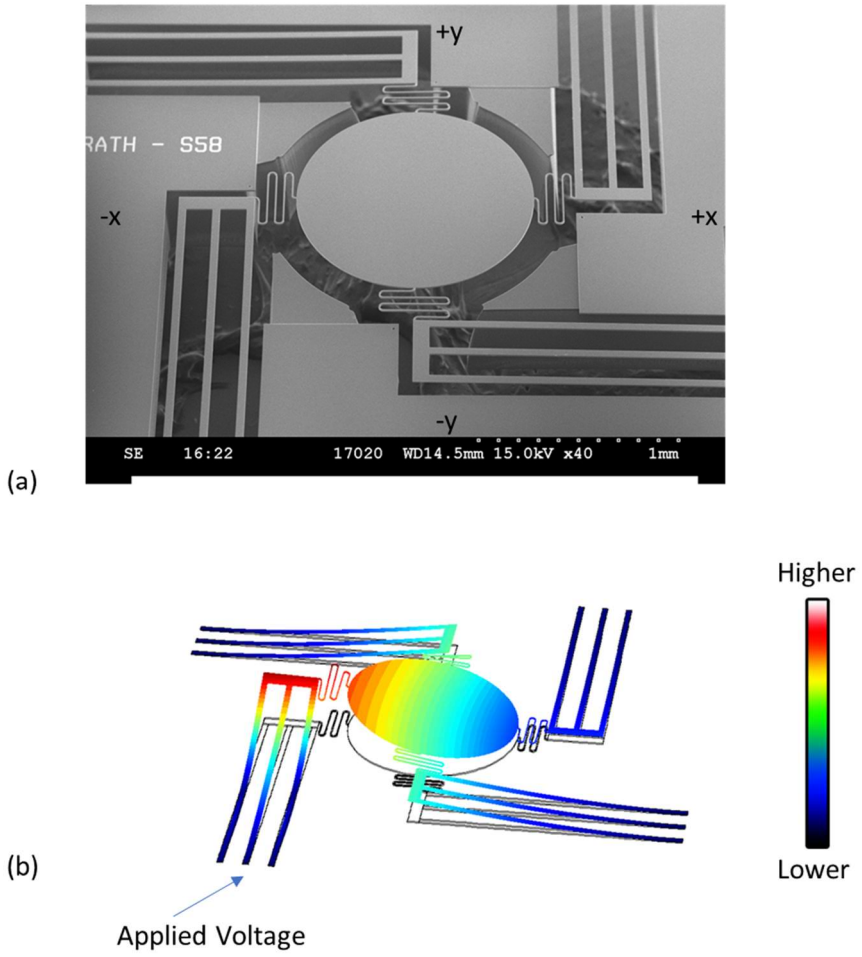

Figure 17. (a) SEM figure of ET MEMS [96] and (b) schematic of working principle for MEMS static rotation.

The MEMS mirror was designed by colleagues in the research group and fabricated by the commercial foundry MEMSCAP Inc (currently part of Science Corporation [119]) using their SOIMUMPs process. The fabrication process includes a base single-crystal silicon substrate with 400 μm of thickness with a thin layer of oxide deposited on it for electrical isolation. A top layer of single-crystal silicon with 10 μm thickness is deposited as device layer. It is important to note that the device exhibits curvature in both the actuators and the mirror as part of the design direction. The curvature is consistent through the MEMS as it is a result of the doping and the in-built stresses that occur after this process in a fully released device. In terms of the actuator the curvature offers a beneficial feature as it inherits them with a predefined direction, allowing the whole mirror to move upwards following the process that was described

in the previous paragraph. In contrast the curvature of the mirror is not a designed and desired feature but an overall outcome of the commercial foundry process.

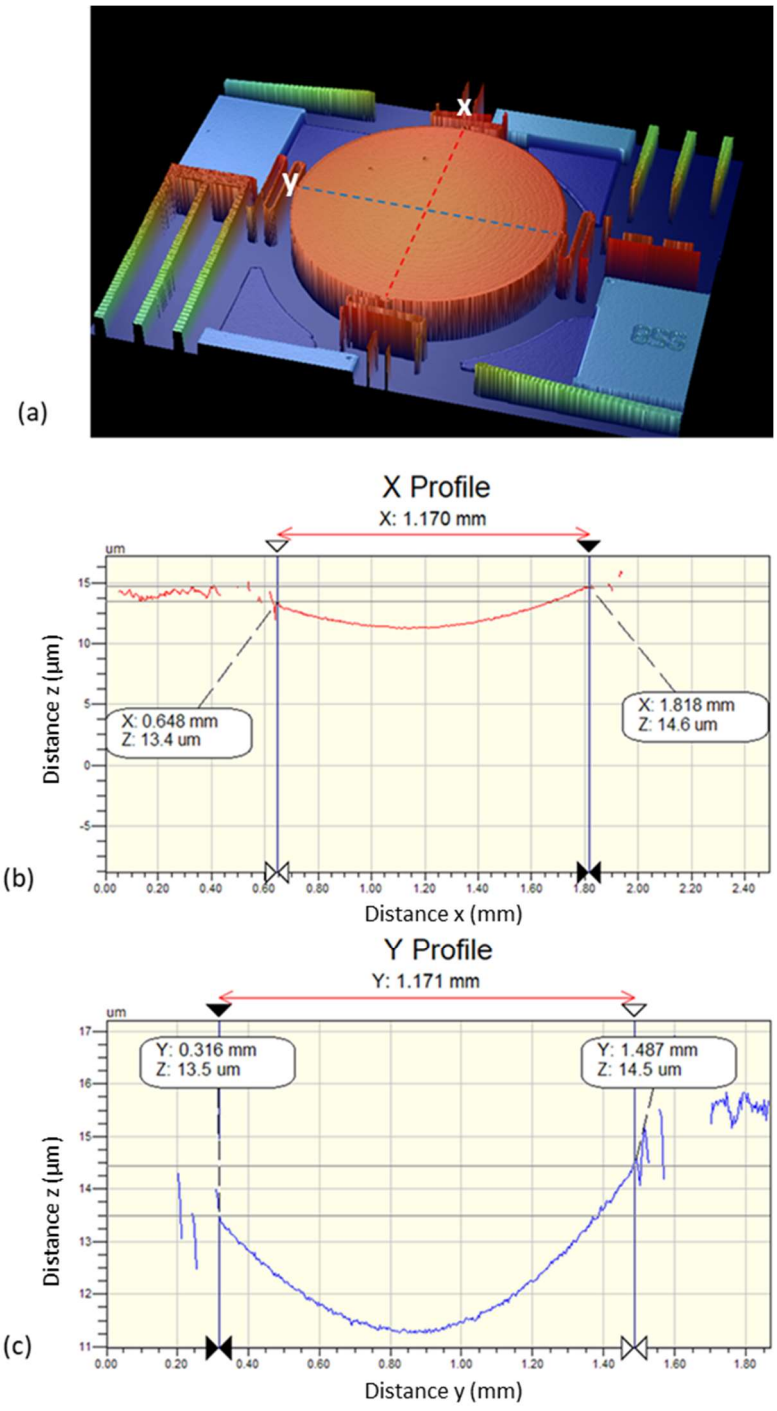

Figure 18. (a) 3D schematic of profile measurement of Thermal MEMS mirror and diagram of surface curvature along the diameter of the mirror for (b) x axis and (c) y axis. Graphs show a radius of curvature equal to 65mm.

The surface characteristics of the mirror have been measured using the VEECO NT1000 optical surface profiler with the same VSI settings as in 3.2.1 and 2.5x magnification (Figure 18). The mirror features a curved surface with an overall radius of curvature of 65 mm. Reflectance of the device is increased with a layer of gold (200 nm) deposited on its surface through a post-process thermal evaporation done by colleagues at the University of Strathclyde.

3.2.2 Thermal MEMS Angle Characterization

Characterization of the static angles of the mirror is achieved using the test screen method introduced in chapter 3.1.2. The results for the static rotation following a DC voltage actuation are illustrated in Figure 19. The mirror angle response has a threshold behaviour around 3 V with a maximum TOSA of 4° being achieved for a voltage input of 15 V. The reason behind the threshold-like behaviour of the angle for lower magnitude inputs can be attributed to the materials response to the heat increase. The maximum voltage range was defined by the maximum acceptable temperature that the device can operate without causing structural damage to the actuating beams or coating on the mirror surface. A secondary identical MEMS has been used to define actuation limits for the design. It was observed that for voltage inputs above 15 V on a single actuator the device actuator beams would glow bright orange, indicating an incandescent behaviour. For temperatures above 525 °C solids instigate the emission of electromagnetic radiation with the exact colour of the radiation signifying a temperature range from dark red (>525 °C) to bright white (>1300 °C) [120]. With the silicon melting point being at 1410 °C it was concluded that the temperatures above the aforementioned range should be avoided as the device could suffer thermal damage.

The slight difference between the achievable angles between the two axes can be attributed to the difference in the actuator beam lengths, with higher angles given by the longer actuators and slightly smaller angle being a result of the shorter actuators.

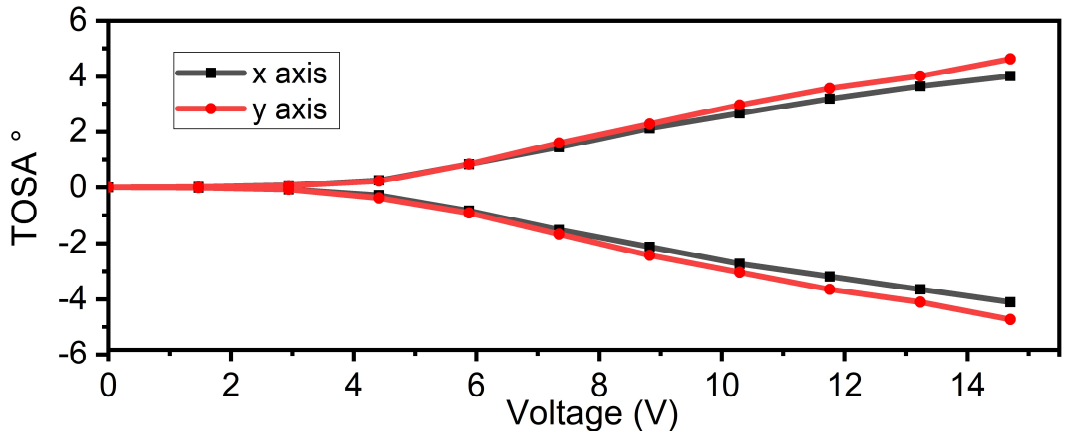

Figure 19. Characterization of thermal MEMS angles in x and y axis for positive and negative angles.

The resonant angle of the mirror was also characterized for the smaller static angle axis and the results are illustrated in Figure 20. The mirror was characterized with three sinusoidal voltage inputs of 9 V, 12 V and 15 V over a frequency range from 2100 Hz to 2400 Hz with a frequency step size of 10 Hz. The highest achievable angles for the three different amplitudes reached a maximum of 5.5°, 7° and 8°. It is important to note that for a rise in frequencies over 2290 Hz the scan line shape stops following a straight-line. This was observed during the screen test measurements where a further increase of frequencies showed that the line gets reformed into an oval shape. This is a result of the resonance movement above this frequency coupling into the resonance movement of the secondary perpendicular scan axis of the mirror and therefore exciting a coupled movement. Only inputs up to 9 V (and respective frequency below 2290 Hz) ensure that the resonance of the chosen axis does not get affected by the perpendicular axis and the control signals for the resonant movement therefore result in the expected scan line. The response time needed between small voltage steps is estimated in the 10 ms range [121].

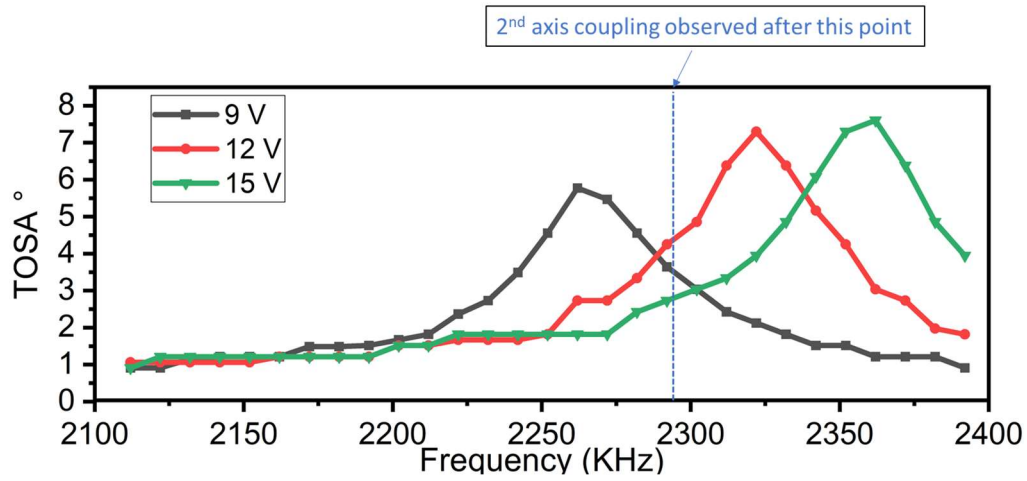

Figure 20. Characterization of resonant angle for thermal MEMS. The response of three different voltage inputs are illustrated namely, V1in=9 V, V2in= 12 V and V3in= 15V with respective resonances at f1=2262 Hz f2= 2322 Hz and f3=2362 Hz.

Finally, an important observation for the characterization of the MEMS is the resonant response of one axis while the static axis is also actuated. As it is illustrated in Figure 21 and in contrast with the operation of the MEMS in section 3.1.2 the resonant frequency does not remain the same with the change of static angle on either the positive or the negative axis. This can be attributed to the heating induced in the orthogonal axis during actuation and the temperature related properties of the material that change the value of the resonant frequency as the temperature of the device increases [122].

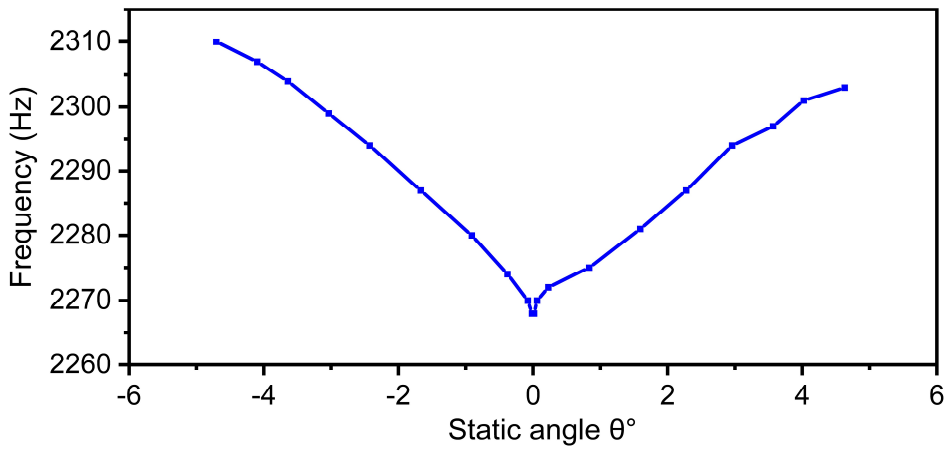

Figure 21. Set of resonant frequencies needed to achieve maximum scan line for each static angle for a sinusoidal voltage input of 9 V.

3.3 Tunable Lenses

The use of electrical tunable lens in LSFM as either detection refocusing elements [63], [123], [124] or axial light-sheet translation mechanism [56], [125] has been demonstrated in various occasions and been introduced in chapter 2.2. Here the electrical tunable lenses will take part in both processes. Specifically, the tunable lens in the illumination path of the LSFM system acts as varifocal element, allowing the light-sheet to be moved axially along the propagation axis. In the imaging path of the LSFM system the tunable lens achieves the purpose of refocusing the imaged plane synchronously with the position change of the illuminated plane. Two different tunable lenses have been used in this thesis. A description of their design and operational characteristics is presented below.

3.3.1 Optotune EL-3-10 Design and Operation Characteristics

The electrical tunable lenses used are manufactured by Optotune and can achieve a focal length change due to their shape changing technology. The lens contains optical fluid sealed behind a glass cover slip in a container with an elastic polymer cover membrane. The clear aperture of the lens is equal to 3 mm. An electromagnetic actuator incorporated in the lens can apply pressure on the membrane container and thus change the curvature of the lens. The operating voltage for the EL-3-10 lens (Figure 22) is specified from -1V to 1V.

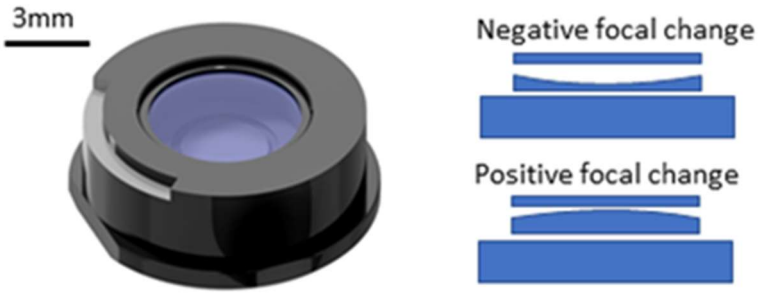

Figure 22. Schematic and working principle of EL-3-10 tunable lens as illustrated on the webpage of the product [126].

The applied voltage creates a current in the voice coil actuator and can transform the lens from concave to convex. The tunable lens operates for a current ranging from -120 mA to +120 mA. As it is illustrated in Figure 23 the optical power of the lens increases to positive values up to 23 dioptres with the maximum positive current. Equally when the lens is driven with negative current the optical power can reach up to -23 dioptres. The response time between current steps is <2 ms.

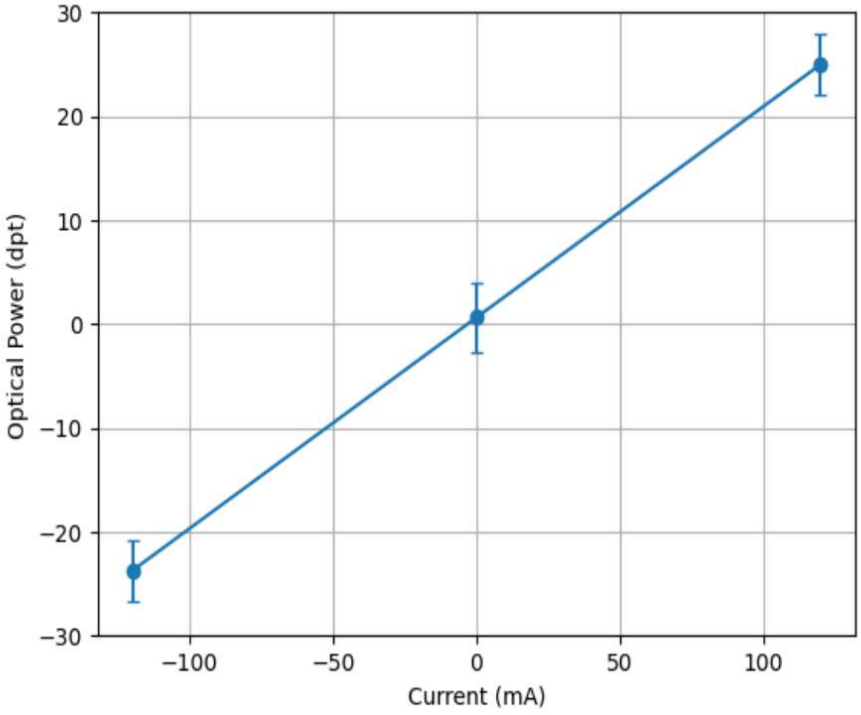

Figure 23 . Optical power graph for EL-3-10 [126].

3.3.2 Optotune EL-10-30 Design and Operation Characteristics

A second tunable lens responsible for adjusting the focal plane of the imaging arm in the microscope system detailed in later chapters is the Optotune EL-10-30. The lens has a larger clear aperture of 10 mm. The shape changing lens working principle (Figure 24) is similar to the previously introduced lens as it also consists of an elastic polymer container with optical fluid. An electromagnetic actuator is used to apply the pressure on the container fluid relative to the electrical current input. This will result to a change in the curvature of the lens as the fluid gets redistributed.

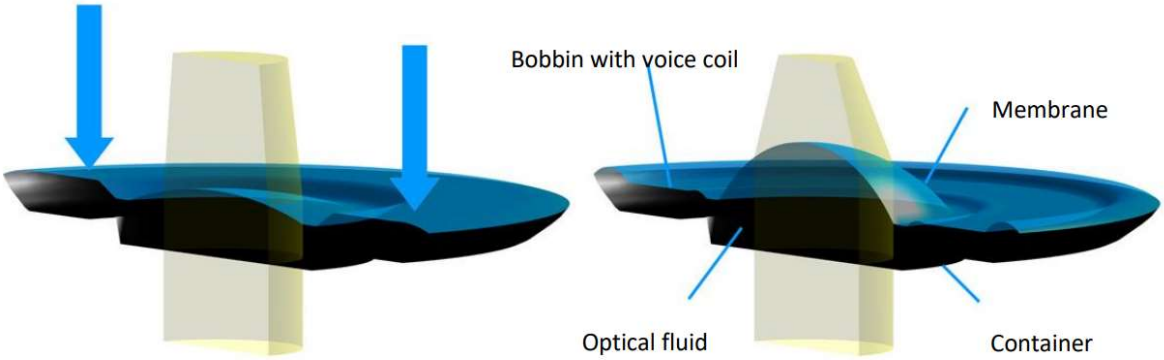

Figure 24. Working principle of EL-10-30 tunable lens [127].

The device can be driven with current inputs up to 250 mA, but only with a single polarity compared to the 3mm lens. The graph illustrated in Figure 25 shows the optical power change relative to positive current input. The initial optical power verifies that the lens has a pre-curved shape with a starting optical power of 8 dioptres up to a maximum attainable power of 20 dioptres. The graphs additionally illustrate two mirrors of the same diameter size group signifying how the use of a suggested 150 mm focal length offset lens can "shift" the addressable optical power range towards negative values for specific application. It is important to note that this has been deemed unnecessary for the designs presented in the following chapter. It is believed that the imaging path of a low-cost microscope will suffer less aberrations when only the absolute necessary number of optical elements are used between the objective lens and the camera sensor. Finally, the documented rise time between current steps of the tunable lens is 2-4ms [127].

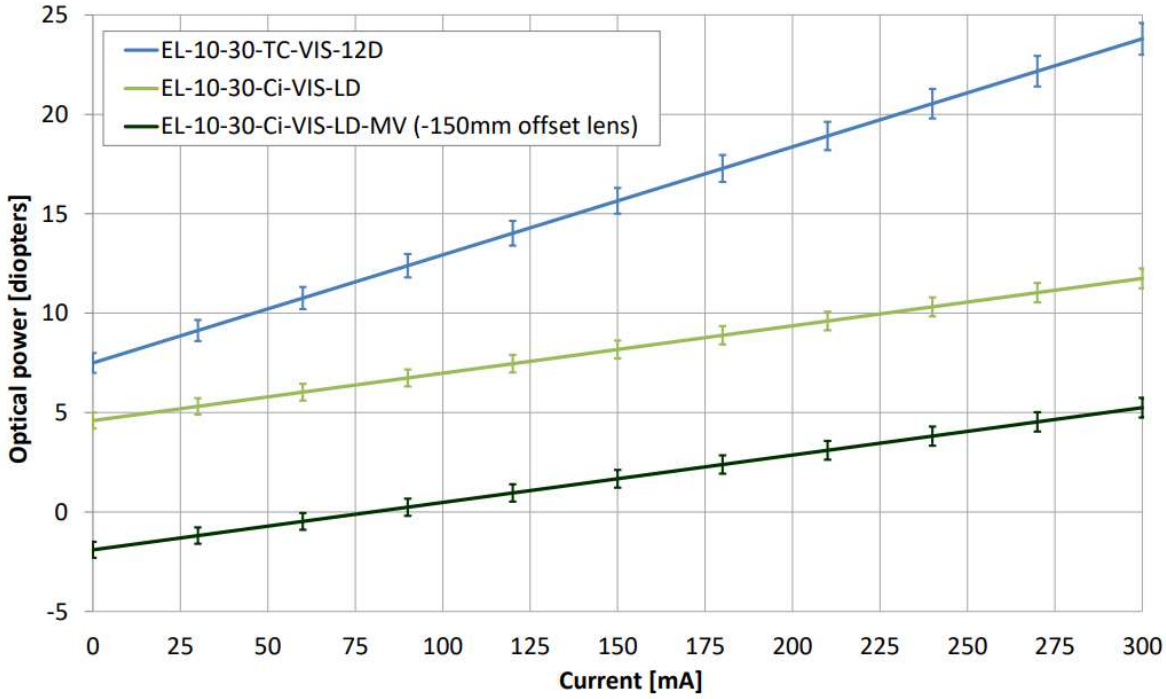

Figure 25. Optical power diagram for EL-10-30- TC-VIS-12D [127] (blue) used in this thesis. The other two lines of the graph EL-10-30-Ci-VIS-LD (light green) and EL-10-30-Ci-VIS-LD-MV (dark green) have not been used in this thesis and show the effect of using the suggested offset lens.

3.4 3D Printed Prism

As is introduced in chapter 2.2.5, LSFM research has shown an interest in allowing to image samples on a microscope slide or larger specimens on an imaging petri dish, as would usually be used with upright or inverted open top implementations. This configuration will essentially need a refractive index matching geometry to limit the optical aberrations that are caused when the light-sheet meets the glass surface of the slide or dish at an angle. Different approaches have been introduced in this effort. The use of a solid immersion lens with an interchangeable immersion medium reservoir to match the two refractive indices has been demonstrated recently [128]. In more practical approaches a water-filled prism [129] manages to correct the angle of incidence for water dipped samples thus limiting the aberrations.

A custom design 3D printed prism is designed for this project in order to target this issue in a cost-effective way. Its goal is to minimize the effect of refraction when traveling between two different mediums with different refractive index at an angle.

3.4.1 Design of 3D Printed Prism

In order to understand the need for introducing a prism in this design it is beneficial to firstly explore the geometrical optics of the imaging area before its inclusion. Specifically, in the imaging area the first medium of the beam path is air and the second is the microscope coverslip with refractive indices equal to 1 and 1.515 respectively. Additionally, an angle is introduced as the beam travels from one medium to the other. The angle is defined by the position of the microscope slide towards the illumination path axis. In this case the angle is 30°. Equally a secondary angle of 60° is created between by the coverslip and the imaging path on the perpendicular axis. As it stands both the illumination beam and the image collected by the objective will be affected by aberrations due to refraction.

The effect of refraction can be limited with the inclusion of a prism as is shown in Figure 26. The right-angle prism with 30° and 60° angles ensures that no additional angle is introduced on the beam path. Additionally, the refractive index of the material used during fabrication is equal to 1.5403 that closely matches the refractive index of the coverslip. With the two mediums attached to each other during imaging the refraction effect will be resolved with aberrations being critically minimized. Coupling of the coverslip with the prism is done by using the Sigma Aldrich I0890 immersion oil with refractive index equal to 1.518. Finally, the matching of the refractive index is completed with the sample and mounting medium that is used. For this reason, the test samples that have been prepared for the microscope are embedded in the Thermofisher antifade glass with refractive index of 1.52. More details of the samples and mounting mediums that have been used are given in the following chapters. It is important to note that the approach of the 3D printed prism applies only to fixed and cleared samples with refractive index of 1.52 – 1.54. For water immersed samples the materials of engineering a similar approach should have refractive index similar to 1.3. Fluorinated ethylene propylene (FEP) is a material that has been used as part of

imaging implementations for zebrafish studies in LSFM and could be the base of a potential water immersed prism design for such samples.

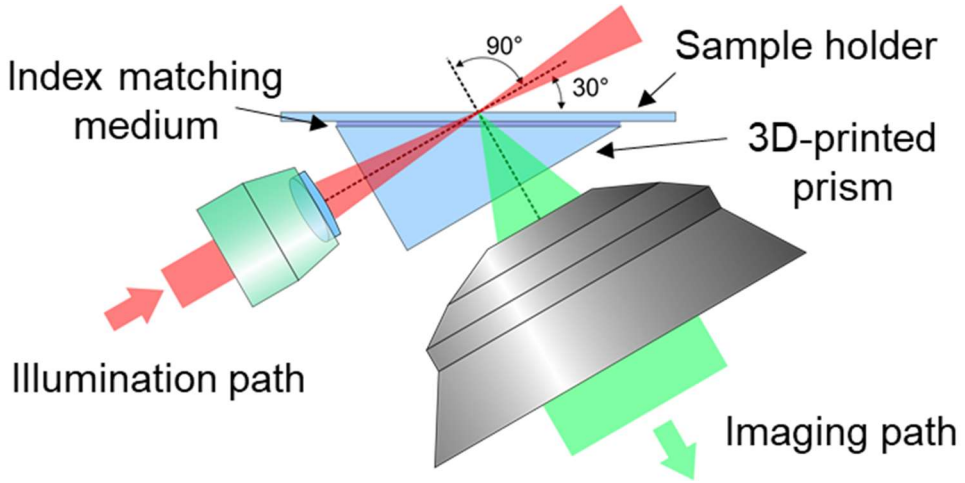

Figure 26 Top view of imaging area with the inclusion of the prism.

The dimensions of the prism are designed according to the geometrical constrains of the sample area. The prism needs to be small enough to fit in the limited available footprint between the two optical paths but equally be large enough to not limit the performance of the illumination and imaging path. Specifically, for the side facing the illumination path, it is important that the maximum translation of the beam is smaller than the prism side taking into account that the beam size will be wider at the prism entrance point. Equally the side of the prism that face the imaging path needs to allow the whole FOV to be collected by the objective. As a result, the side needs to be large enough to allow the opening angle of the light to fully pass through the prism. The chosen side lengths of the prism to overcover these requirements are 2.9 mm, 5 mm, 5.8 mm. The length of the prism is 30 mm to allow convenient use during imaging.

3.4.2 3D Printing of Prism

The 60°/30° prism is fabricated with an optical 3D-printing approach based around a desktop 3D-printer. A Form 3 laser printer by Formlabs using their clear resin material option is chosen for this purpose. The printer uses the stereolithography printing technology to produce solid polymer objects from a monomer liquid resin tank. In this technique the object is produced layer by layer using a photochemical process where

the light causes the monomers to crosslink together in order to form polymers [130]. Specifically, in this device the Formlabs RS-F2-GPCL-04 is used in its liquid form as the base monomer to produce an approximate optical transparent object with the optical processing unit being responsible of projecting the laser accordingly to each layer of the 3D design. The resolution step of each layer is user defined at 25 μm.

The interface of the slicing software is illustrated in Figure 27. Slicing is the software method responsible for separating the designed object into a stack of individual layers. As mentioned above the 3D printer will require a file with the layer information to implement the stereolithography process. Added supports is equally an essential part of the printing to ensures the rigidity of the item as well as its accurate printing result. In a non-supported print, the object is directly printed onto the print plate with the possible side effect of overprint residue being present in most cases.

For this specific design, the prism is sliced into 1,337 layers, including the support structure consisting of a set of rods with a touchpoint equal to 0.40 mm. Additionally, printing of sensitive structures requires the introduction of a 10° - 20° tilt of the object's flat surface. Besides reducing the printing time as the surface area decreases, the tilt will also reduce the build forces occurring while the build platform raises with each layer.

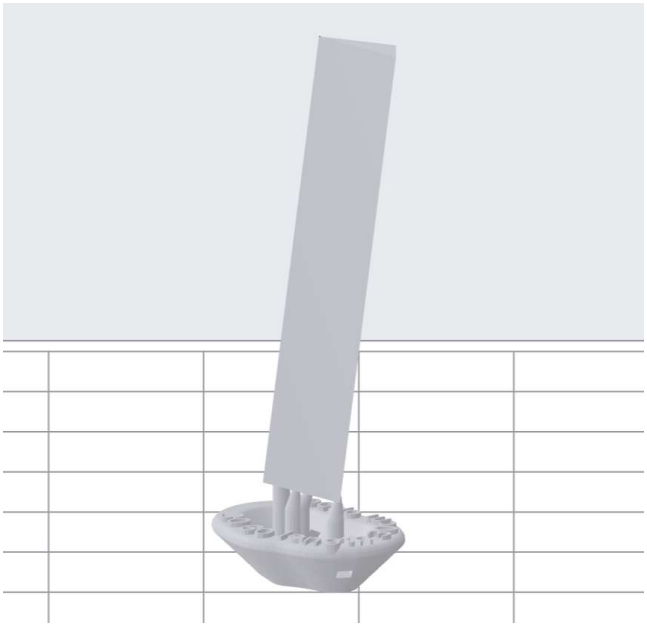

Figure 27. 3D printed prism design orientation in Formlabs PreForm 3D Printing Software.

In order to achieve a high-quality transmission through the prism it is important to follow a set of post processing steps. The main goal of this process is to ensure that the prism is clean while enhancing the surface quality in order to match the quality of a glass surface.

The prism is removed from the platform and placed into an IPA container to remove excess resin. The cleaning of the prism can be further enhanced with the placement of the IPA/prism container into an ultrasonic bath for up to 15 minutes. At this stage the prism is cleaned and surface coatings on the optical sides can be added to create an optical quality surface. A small layer of liquid resin (~5 ml) is deposited on a standard microscope slide. The slide is positioned into a spin coater (Ossila Spin Coater) for 30 seconds at 850rpm ensuring that the liquid resin is uniformly distributed on the microscope slide surface with a layer thickness off <500 μm. The prism is then safely positioned on the liquid resin layer and transferred together with the slide in a UV curer where the liquid resin will cure and merge to the prism. The prism is detached carefully from the slide using a scalpel to cut around the edges of the coated area. This process will be repeated for the remaining sides of the prism. The surface smoothness results after post-processing are illustrated in Figure 28. The data is captured using the Veeco NT100 optical profiler introduced in chapter 3.1.1. Using the VSI method and magnification of 2.5x. It shows an overall uniformity level with variations on the surface limited below 0.1 μm. The optical transmission of the prism was also measured using a 488 nm laser source and a Thorlabs pm100d power meter. For all 3 sides the results were the same with transmission of 94%. Transmission is measured with both 473 nm and 488 nm laser sources. An evaluation of the prism performance in the imaging path is provided in a later chapter where two images of the same sample are presented with and without the use of the 3D printed prism.

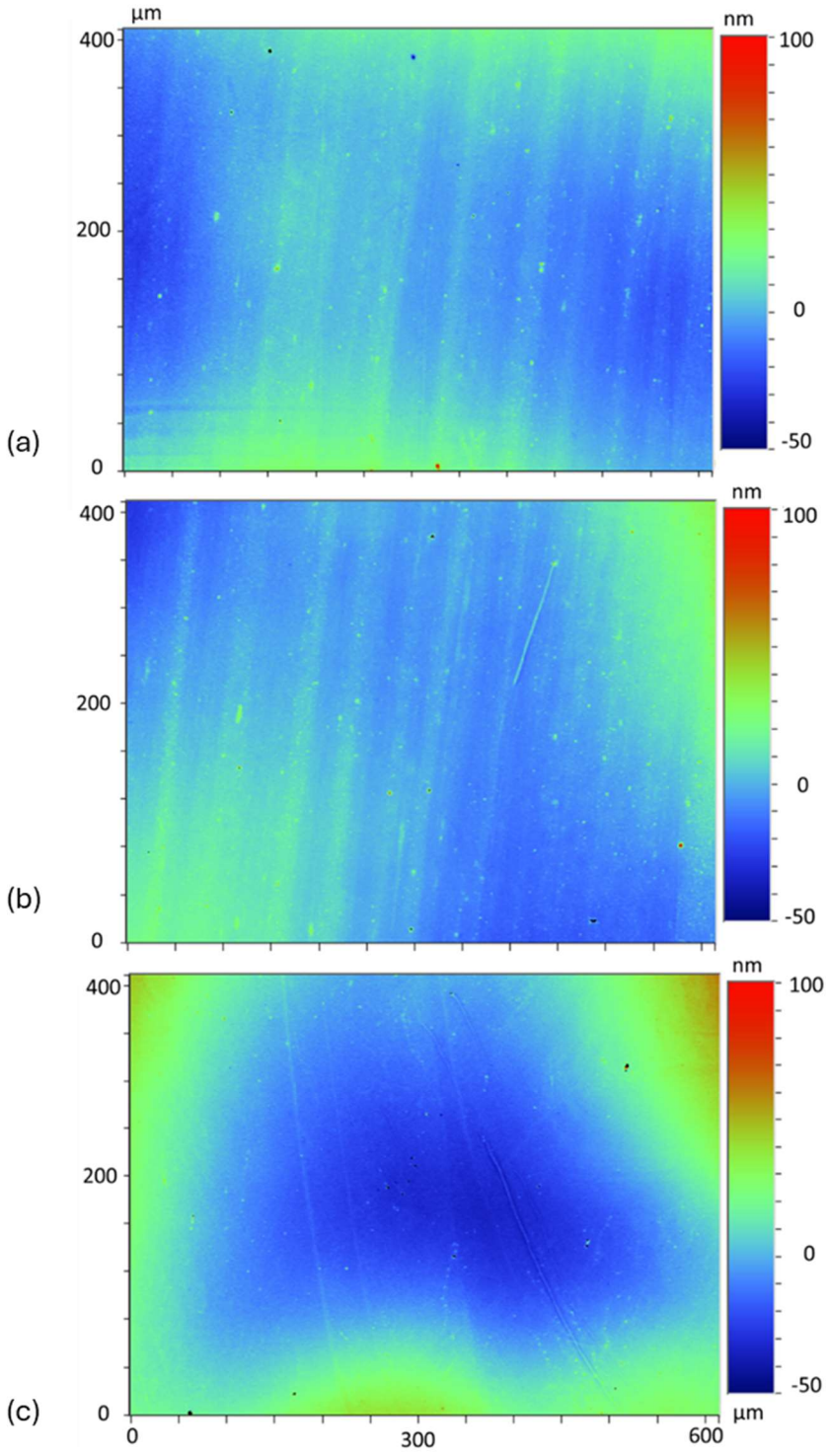

Figure 28. Veeco NT100 Surface roughness measurement on microscope slide side with roughness limited below 100 nm for all sides of the microscope for the 3 different sides (a) sample side (b) imaging side and (c) illumination side.

3.5 Summary

A characterization of the optical elements and custom parts that are enabling the active control and miniaturization of the targeted LSFM implementations is presented in this chapter. The 2D piezoelectric MEMS presented in this chapter can be used for the generation of the light-sheet using one axis, with the ability of translation of the light-sheet on the orthogonal axis. The fabrication characteristics of the MEMS are briefly introduced that enable the piezoelectric actuation of the two axes through a 2 μm PZT layer deposited on both the spiral shape actuators and the ring shape mirror frame actuator. At the same time the 1.1 mm diameter of the mirror surface was analysed to reveal a flat surface profile with variations less than 0.03 μm. The characterization showed a maximum achievable static angle range of 3° when the device was driven with input voltage from -20 V to 20 V. The fast/resonant axis shows that the mirror highest angle of 27° can be achieved at a resonant frequency of 36.8kHz.

An alternative to the use of the piezoelectric MEMS mirror is the electrothermal MEMS mirror design also introduced in this chapter. The MEMS has four actuators separated by 90° in the perimeter of the mirror. The set of actuators located on the same axis differs in length by 100 μm with the orthogonal actuator set to avoid matching of resonant frequencies. As a result, one of the axes is used for the fast /resonant movement of the mirror and the other one for the slow quasi-static axis. The maximum achievable angles in the static axis show an improvement over the PZ MEMS with the achievable range extending to 8° for an input of 16 V. The second axes can be used with frequencies up to 2262 Hz to avoid nonlinear scanlines with an addressable range of 6° degrees when 9 V are applied to a single actuator, less than what it was achievable with the PZ MEMS.

Additionally, the chapter shows the characterization of two different tunable lenses in terms of the addressable focus shift range. The two lenses have the same operation methodology while their specific characteristics vary in their 7 mm aperture difference. The optical power distribution is different in the two cases with the 3 mm lens ranging from negative to positive values as the 10 mm lens range starts from close to 0 and extends to the positive range.

Finally, the chapter presented the design, fabrication, and characterization information of a 3D printed prism. The prism is an essential part of the optical paths when a sample mounted on a microscope slide is being imaged at an angle. The prism is used to correct both the illumination path and the imaging path divergence and reduce optical aberrations like astigmatism. The fabrication of the lens was shown with a 3D printer able to print clear plastic and a post processing protocol that provided optically clear results and glass surface quality matching.

The optical elements analysed in this chapter enable the design of a miniaturized microscope meeting the requirements of light-sheet generation, active control of the optical paths and aberration correction in a compact and low-cost package with its details shown in the next chapters.

4 Piezoelectric MEMS Enabled Light-sheet Microscopy

4.1 Introduction

This chapter covers the complete design and analysis of a miniaturized piezoelectric (PZ) MEMS enabled LSFM. This includes the overall optical design of the microscope (Figure 29), along with the choice and application of the individual components that have been used in the imaging and illumination paths. The two optical paths are linked to a specific axis when it comes to the explanation of the designs in both this and the following chapters. The imaging path relates to the optical path of the z axis and the illumination path to the optical path of the x axis.

After the system overview, the analysis of the capabilities of each optical path is presented. On the excitation side, an exploration of the use of the PZ MEMS within the microscopy system is given, together with evaluation of critical parameters for the design. On the imaging side, specifically the use of the Optotune EL-3-10 tunable lens is analysed as an active element for varying the focus in the imaging arm. Following the independent characterisation of each optical paths, the overall imaging performance is presented.

4.2 Design

The working principle of the microscope is based on the DSLM concept introduced in chapter 2.2.3. The schematic overview of the system is shown in Figure 29. The generation of the light-sheet is a result of the fast, resonant PZ MEMS rotation being relayed into the sample through a telecentric optical geometry. The orthogonal slow rotation axis of the PZ MEMS allows shifting of the light-sheet illumination plane with a continuously adaptable step size. For the imaging path the illuminated 2D slice of the sample will be captured by the 20x objective, combined with the Optotune EL- 3-10 which will readjust the imaging focus position and allow capturing each of the

illuminated planes selected by the MEMS. A synchronised sweep of the MEMS slow axis and tunable lens with defined step size will provide an imaging stack that correspond to the imaged 3D volume. In this way 3D LSFM can be enabled by all-optical scanning and without the use of a mechanical translation stage during imaging.

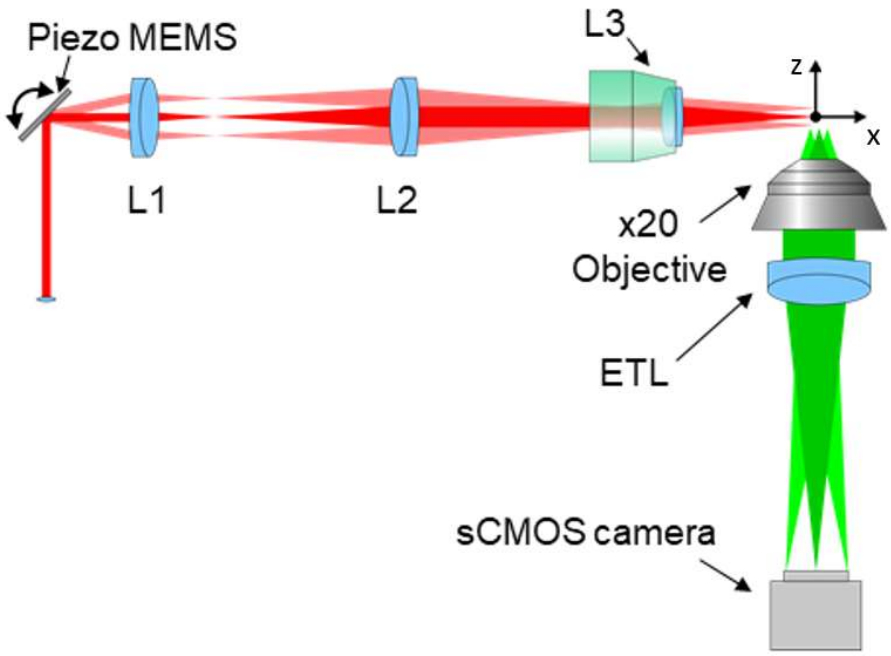

Figure 29. Top view schematic of miniaturized LSFM highlighting the components of the illumination (red) and imaging (green) path. The illumination path consists of the 45° placed MEMS mirror folllowed by lenses L1(f1 = 7.5 mm) L2 (f2 = 30 mm) and L3 (f3 =7.5mm) creating a telecentric digitally scanned light-sheet. The imaging path includes an economy x20 microscope objective closely followed by the electrical tunable lens and sCMOS camera at the finite conjugate distance.

4.2.1 Imaging Path Design

In the first instance, the concept behind the design of the imaging path revolves around the common trade-off between a large FOV and high resolution while keeping costs at a minimum. Both of those requirements are mostly related to the choice of objective, making it the most fundamental element in the imaging path. As it has been introduced in chapter 2.2 the geometry of LSFM requires a thoughtful selection of the imaging objective to not physically interfere with the optics of the illumination path and allow

a long enough working distance to enable imaging of samples mounted on microscope slides and other flat-bottomed standard sample holders. In other words, the objective has to either feature a slim design and/or have a large working distance. Objectives that meet the three requirements of FOV, magnification and size exist in the market and have been used in examples of LSFM but they don't meet the final requirement of cost that the microscopes developed in this thesis requires. As a result, the objective selection resulted to a Newport MVC-20X objective with a price of £100, that has a 20x magnification, 8.72 mm working distance and 0.4 NA that is expected to provide single micron resolution and a horizontal FOV of over 400 μm. It is important to note that an estimation of the FOV is not only a subject of the design specifications of the objective but it will additionally be affected by the camera sensor size and the tube diameter of the microscope. A simplified estimation of the FOV can be done as follows for a fixed magnification M, and a camera sensor size H. Taking as example the Thorlabs CS2100m sCMOS camera with a 2/3'' sensor and 5.04μm pixel size the resulted FOV will be.

$$FOV = \frac{H}{M} = \frac{Sensor\ size}{20} = \frac{9.6768\ \text{mm}\ x\ 5.4432\ \text{mm}}{20} = 0.484\ \text{mm}\ x\ 0.272\ \text{mm} \quad (5)$$

In contrast the diffraction limited resolution can be defined in relation to the NA using Rayleigh [131] equation. The resolution can be estimated for GFP stained samples using a λ=510 nm emitted fluorescence signal as:

$$Resolving\ power = \frac{0.61\lambda}{NA} = \frac{0.61 \times 510\ \text{nm}}{0.4} = 777.8\ \text{nm} \quad (6)$$

An active control of the focal plane is required to capture every focal plane during the translation of the light-sheet through the sample with the slow axis of the MEMS. The active element responsible for synchronizing the focus of the imaging path to the change of the illuminated plane is the Optotune EL-3-10 with 3 mm clear aperture and potential to create positive and negative focal shifts. The lens is positioned as close as possible to the back surface of the imaging objective to minimise vignetting and significant reductions of the imaging resolution. A 1920 x 1080 sCMOS camera

(Thorlabs CS2100M-USB) is positioned at a 160 mm distance from the objective, equal to the specification of the objective. A fluorescence emission long pass filter (Thorlabs FELH0500) is attached in front of the camera to block scattered illumination light during imaging. All the optical elements of the imaging path are housed in a 1-inch diameter lens tube. The tube ensures both the secure alignment of the path as well as the protection from ambient and stray light reaching the camera sensor.

4.2.2 Illumination Path design

The requirements behind the design of the illumination path is to create a thin light-sheet in a telecentric beam configuration. Additionally, it is important to consider the working distance between the illumination and imaging path. Equally to the design of the imaging path, the working distance needed for the illumination optics can be a compromising factor in the design. Choosing to use microscope slides as the main form of sample holder demands a sufficient working distance when the slide is positioned at an angle of 30° towards the imaging path and 60° towards the illumination path. The choice of a smaller angle towards the imaging path is made due to the physical size difference between the imaging objective and the compact light-sheet focusing lens as it was adjusted to be the angle that can accommodate the microscope slide. The slide placement should be implemented in a safe way during imaging avoiding any contact with the optics used on the two paths while the point of focus for both optical paths reaches the sample area (Figure 30).

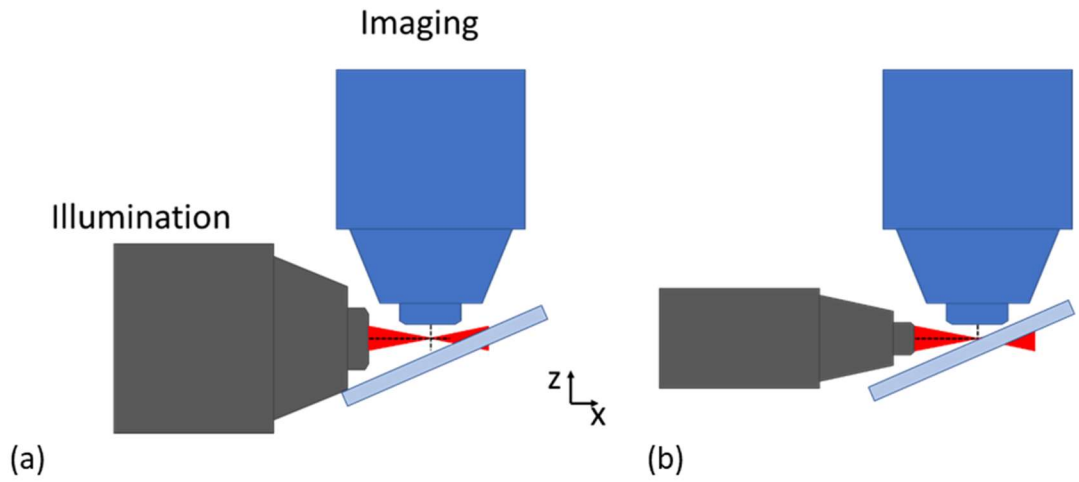

Figure 30. Slide positioning example in LSFM. Replacing the, (a) relatively bulky, standard illumination objective with (b) a small diameter focusing lens can extend the working area and allow for a safer slide integration.

Choosing to use an illumination path consisted of small diameter lenses provides an effective alternative to the much bulkier and expensive solution of a dedicated excitation objective when it comes to making use of the working area and resources for this system.

The excitation side design concept is simulated with Optalix, a ray tracing and wave-optics simulation tool, as illustrated in Figure 31. Optalix serves as an optimization tool for parameters of interest such as beam waist characteristics, the relationship between input and output beams using a variable collimator, the telecentricity of the beam for parallel optical paths during MEMS actuation, and the expected field curvature. In technical terms, the physical characteristics of the optical elements used in the system are entered into the software as constants, as they are either off-the-shelf products or elements with predefined characteristics. The relative distances between the elements are set as variables. These values, along with the aforementioned parameters, serve not only as a tool for analysis but also as a practical guide for the optical alignment of the system, which is presented in the relevant chapters. The software utilizes ideally collimated beams, while optical elements are defined according to manufacturer specifications and positioned in mathematically correct positions along the optical axes. It is reasonable to assume that under real conditions, it is challenging to replicate such accuracy. What is both possible and helpful,

nonetheless, is having these characterization values as targets during alignment. These can be used both for troubleshooting and as a guide for striving to get as close as possible to the simulated optimization presented in this section.

The used lenses are off-the-shelf achromatic doublets with a maximum diameter of 12.7mm to ensure that the physical dimensions of the microscope remain small as well as the optical requirements for a tightly focused beam and telecentricity are met. Specifically, the Optalix design consists of the following parameters with the ideal physical and optical properties described as followed. The input beam is a 473 nm laser with the diameter defined by the used optical collimator. The chosen collimator package (Thorlabs CFC2-A) provides a collimated beam with measured diameter of 400 μm FWHM. The beam is directed towards a 45° placed mirror that represents the PZ MEMS described in chapter 3.1 with mirror diameter of 1.1 mm. The choice of collimator reflects the requirement of the output beam being smaller than the diameter of the MEMS mirror. The MEMS will reflect the beam towards the first lens (Thorlabs AC050-008-A) with f = 7.5 mm and an aperture of 5 mm with their distance between them being equal to the back focal length of the lens at 5.2 mm to ensure telecentric collection of the scanned beam. The second lens is a f=30 mm achromatic lens (Thorlabs AC127-030-A) with an aperture of 12.7 mm. Based on the desired 4F configuration it is placed at a distance of 36.4 mm. The non-scanned beam exiting the 2-lens telescope system is collimated with a 4x magnification factor defined by the ratio of the two lenses. A second f= 7.5 mm focusing lens (Thorlabs AC050-008-A) is placed again at 2f distance from the second lens in order to complete the telecentric setup in the sample space. According to the simulation the distance between the two lenses is 25 mm. A PMMA surface matched with a water surface is inserted after the focusing lens. The surface couple is part of the optical design in order to align with the experimental method introduced in the next chapter, where a cuvette is used in the same position for analysis of the light-sheet. Additionally, the PMMA surface itself is serving as a simulation for the prism that is used in the imaging experiments.

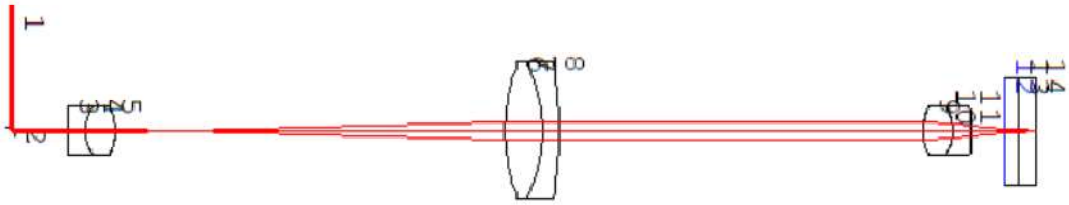

Figure 31. Optalix ray tacing schematic of the designed illumination path, starting after the collimation of the incoming laser beam at position 1 until it reaches the focus at position 14.

The methodology of the simulation was to keep the physical dimensions of the lenses constant, as they are off the shelf products, and vary the distance between them in order to obtain the optimized telecentric setup. The optimized design gives a wave optics simulated point spread function PSF cross section of the focused beam at the centre of the illumination path as illustrated in Figure 32. The simulated FWHM of the beam is 2.28 µm. The focus plane is located 5.8 mm away of the focusing lens.

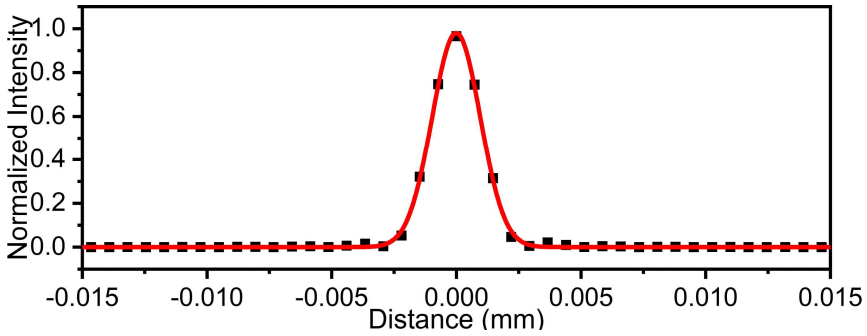

Figure 32. Simulated Gaussian excitation beam cross-section in the illumination focal plane using an Optalix simulation, with a measure FWHM of 2.28 µm.

According to the specifications for the Thorlabs CFC2-A collimator, the collimation of the 473 nm input beam is possible to be diverging from the expected diameter of 400 µm. The relationship between the starting beam diameter and the FWHM of the beam in the focal plane is presented in Figure 33. A range of input beams of diameters between 0.2 mm and 0.6 mm was used in the simulation to extract the PSF FWHM for each scenario. The graph showcases a rapid decrease of the focal point FWHM with increasing input beam diameter. As a result, the actual PSF and FWHM value of the

excitation beam will be verified experimentally during the characterization of the illumination path.

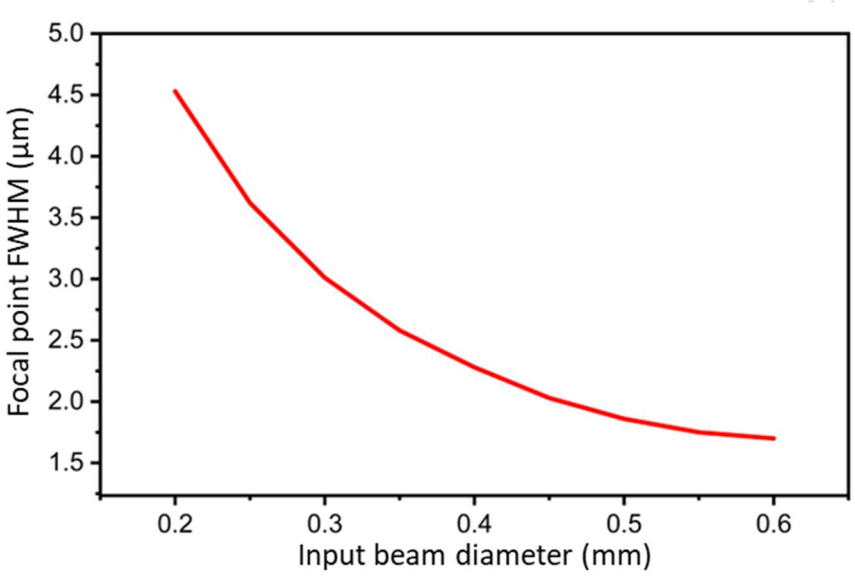

Figure 33. Relationship between output beam diameter of the Thorlabs CFC2-A collimator and FWHM of the resulting PSF for the illumination path. The graph is an outcome of Optalix simulations over the range of expected input beam diameter values in the setup.

Initially the mirror is at rest when positioned in the 45° configuration. It is possible to simulate the equivalent beam paths for a set of different angles ranging from 43.5° to 46.5° that respond to the TOSA of the mirror along the slow axis. The results are illustrated in Figure 34. The simulation confirms that the design geometry realises beam paths that are parallel towards the target plane. The effect of field curvature due to the use of achromatic lenses instead of fully corrected scan and tube lenses is also visible as part of the angle change. The field of curvature at the focal plane is calculated at a 60 µm difference between the central path and the maximum paths.

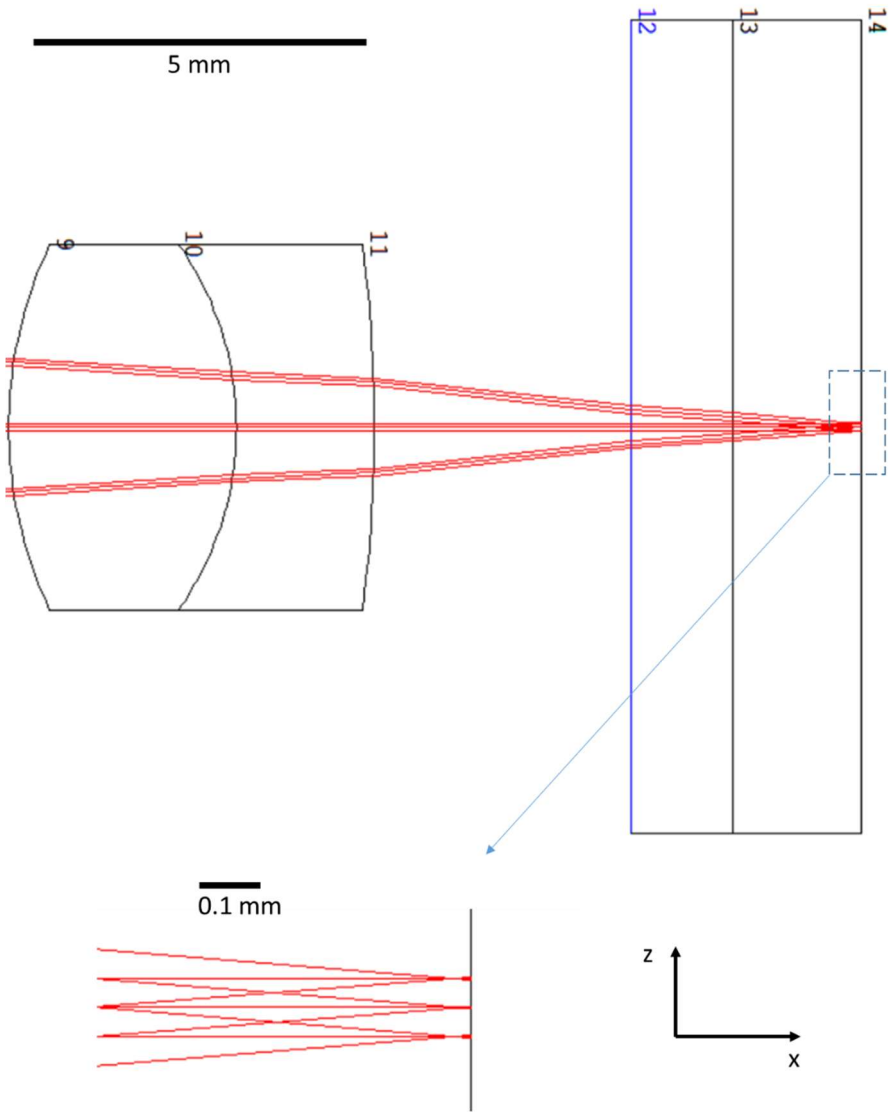

Figure 34. Top view (xz) of focusing lens from Optlix ray tracing simulation. Three different beam paths are presented at once for three different angles for the slow MEMS axis. The zoomed-in view of the focus area illustrates the parallel beam paths resulting from the telecentric setup.

The same process can be followed to observe the telecentricity along the fast axis of the MEMS, where the TOSA of the mirror is ranging up to 27°. According to the Optalix simulation the optimized result for fast axis scan can be seen in Figure 35. Again, it is possible to quantify the effect of field curvature along the x axis by observing the focal distance difference between the optical paths that result from a TOSA of 0° and a TOSA of -13.5°/13.5°. In this case the maximum beam paths focus at 140 µm distance shorter than the central path.

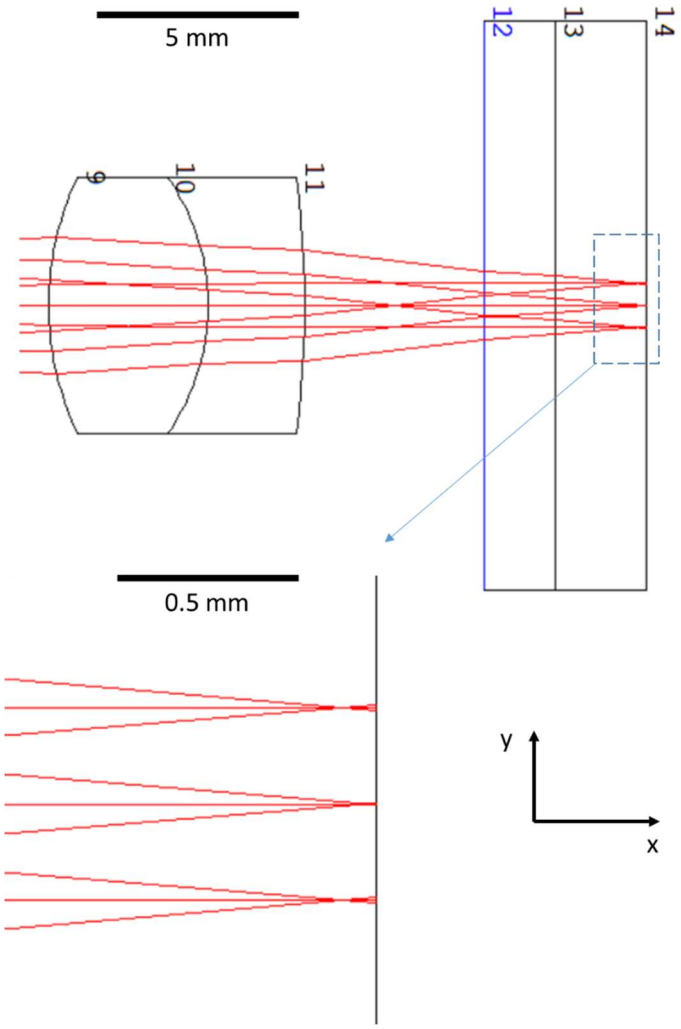

Figure 35. Side view (xy) of the focusing lens in the Optalix ray tracing simulation. Three different beam paths are presented at once for three different scan angles of the fast-resonant MEMS axis. The zoomed-in view of the focus area illustrates the parallel beam paths resulting from the telecentric setup.

4.2.3 Design Implementation

The illumination source for the setup consists of a 473 nm CNI laser source (CNI-473 nm) with a $1/e^2$ diameter of 0.7 mm. The maximum optical power of the source is measured at 50 mW. A 10x microscope objective lens is used for focusing the output beam into a single mode fiber (Thorlabs P1-460B-FC-1), with the tip of the fiber being mounted onto a 5D stage with positioning and tip/tilt motion to ensure the best possible coupling efficiency. The coupling efficiency after alignment was found to be at 15%.

In order to ensure repeatability and robustness of the system, the excitation arm lenses are placed in 3D printed holders and aligned into a half-inch lens tube (Thorlabs SM05L20C) according to the Optalix results. The custom printed holder used for the two f=7.5mm lenses is presented in Figure 36. The design concept ensures that the 5mm diameter lens is slotted in the holder while a 2mm grub screw secures the fit. On the other end of the holder the design expands to a half-inch diameter cylinder that can be fixed into the lens tube, making use of two retainer rings (Thorlabs SM05RR) intended for fixing half-inch lenses in the tube. An important feature of the design is the cutaway sides. The sides are cut with a 30 ° angle in order to ensure that the sample holding microscope slide is safely positioned and correctly aligned near the holder. The holder was 3D printed with a Formlabs Form 3 printer following the methodology introduced in chapter 3.4.2 but without the surface post processing technique.

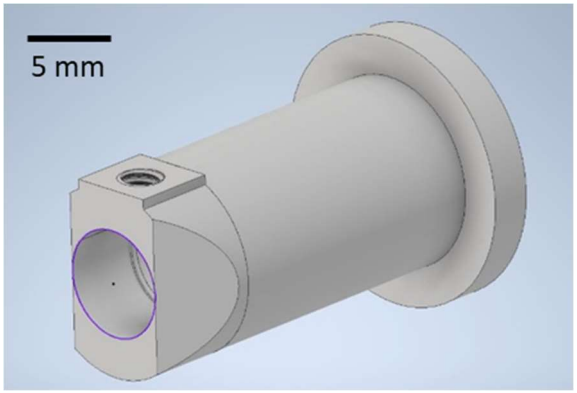

Figure 36. Schematic for 3D Printed holder used for the two 5 mm diameter lenses of the illumination path. The base of the holder is designed to fit a half-inch tube lens while being secured by two retaining rings. The lens is sloted through the front opening and secured by a a 2 mm top screw.

The complete implementation of the miniaturized LSFM is illustrated in Figure 37. The optical and mechanical components that have been described in the design of the microscope are aligned and positioned onto a Thorlabs MB2530/M breadboard. The footprint of the microscope measures an area of 20 cm × 28 cm while the height is defined by the mechanical postholders and in the current implementations measures 13 cm.

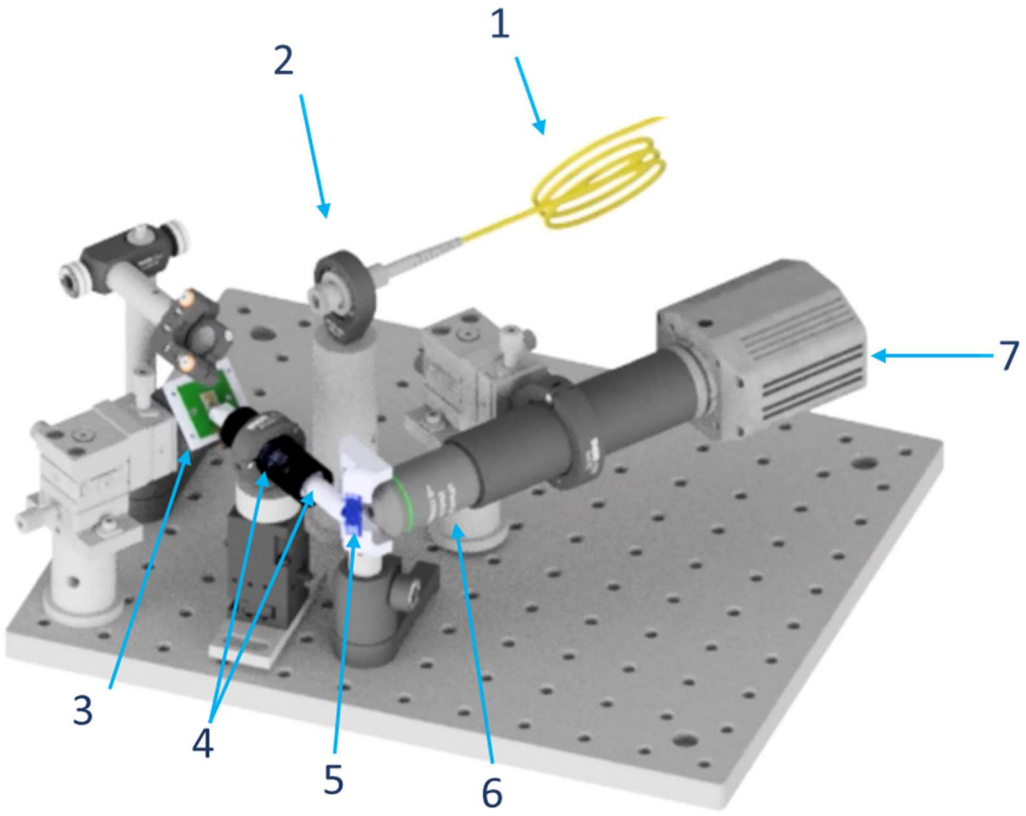

Figure 37. 3D schematic for the implemented Miniaturized LSFM: 1 - Fibre, 2 - Collimator, 3 - PZ MEMS, 4 – Illumination lens tube and focusing Lens, 5 – 3D Printed Prism, 6 – Imaging Objective, 7 – Camera.

4.2.4 Imaging Path Characterization

The first step towards analysing the imaging capabilities of the system is to calibrate the pixel/micrometre ratio of the camera in the given setup. This can be accomplished by imaging a sample with known dimensions, such as a microsphere or a resolution test chart. The measured length (FWHM) of the object in pixel is then divided with the specified dimension, giving the unit transformation ratio of the system. In order to derive the ratio a 15 µm fluorescence bead target (ThermoFisher FocalCheck™ Fluorescence Microscope Test Slide #1) was initially used. The microspheres are ring stained with three layers of orange, far red and green fluorescent dye with a specified diameter of 15 µm.

Prior to placing the slide in the sample area, the coupling of the fixed sample with the 3D-printed prism is achieved using immersion oil (Sigma Aldrich I0890) and tape at the top and bottom of the long side of the prism. The slide is placed in the sample area using a post-clamp and mounted on 3D translation stage for more accurate positioning at the imaging area. It is fixed at the 60°/30° angle configuration at the working distance of the objective. The intensity profile of the mid-section of the beads is acquired using a single line intensity plot along a set of beads. The profile plots for a set of five beads are shown in Figure 38. The results are recorded with 2x2 binning of the camera chip during imaging and exposure time of 50ms. The FWHM is measured at 33 pixels resulting in a micrometre to pixel ratio of 0.453. Based on this ratio the 960 x 540 px FOV is related to 435μm x 246μm in real space. Both the micrometre to pixel ratio and the pixel FOV are calibrated with 2x2 camera binning [132] that was used throughout the imaging presented in this chapter to increase the imaging SNR. It should be noted that in general binning can lead to resolving power loss. In order to minimize this effect, the combined pixel size should still meet the Nyquist criterion and be at least 2 times smaller than the lateral resolution. This is verified with the resolution measurements that are introduced later in this chapter.

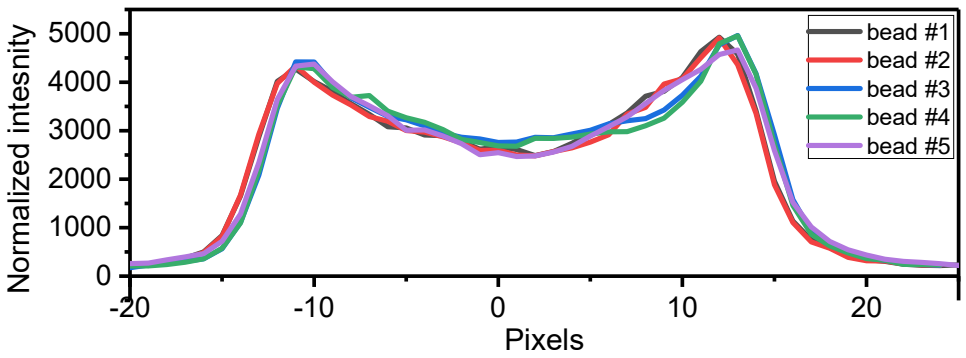

Figure 38. Intensity profile plot for a set of 5 beads of 15μm diameter. The plots are used to extract the calibration μm/pixel ratio of 0.453.

A series of images are presented in Figure 39 for a further quantitative characterization of the imaging path. The sample for this analysis is a USAF 1951 resolution target (Thorlabs R3L1S4PR), which consists of 120 nm thick chrome lines on a standard microscope side. The FOV displays a black and white target area. The attainable

resolution is derived based on the line spread function and edge response of the imaging system [133].

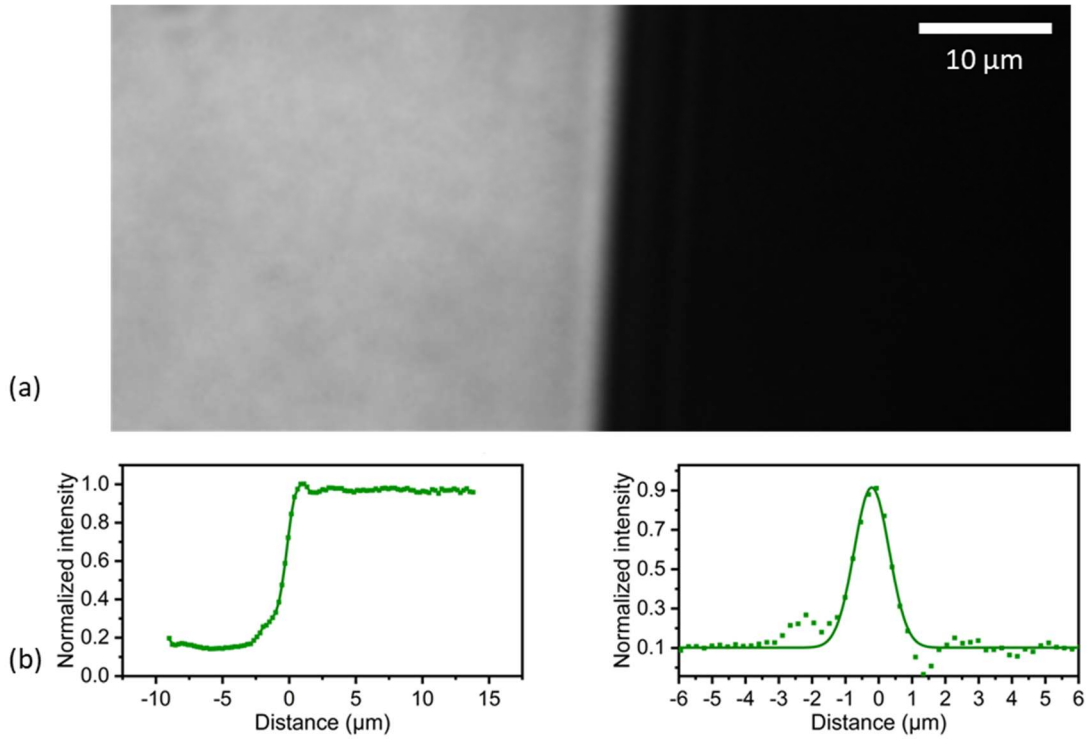

Figure 39. (a) Edge Spread Function ESF used for edge test. (b) Line spread function LSF derived from ESF resulting in the lateral resolution of FWHM=1.1µm for the imaging system.

The lateral resolution of an imaging system can be measured by extracting the Edge Spread Function (ESF) of a single line in an area defined by a sharp change in contrast (black to white). An example of such area is also illustrated in Figure 39 (a). The first derivative of the ESF is the Line Spread Function (LSF) (Figure 39 (b)) which is identical to the equivalent PSF of the system. The FWHM of the LSF is chosen to represent the resolution of this system.

It is important to note at this point the details of the functional fitting of imaging data, shown for the first time in the LSF plot of Figure 39 (b), as this process is utilized on several occasions in this thesis to provide quantitative results. The Gaussian fit shown in this figure, and in similar figures in later sections, is a functionality provided by the data analysis software, Origin. The software offers the capability to fit various functions to plotted data. The Gaussian function [134] has been predominantly used throughout this thesis for fitting purposes. The fitting process takes into account all

datapoints of the plot, with the tails of the plot approximating the background level of the graph. When referring to the FWHM in terms of the fitted plots, it denotes the halfway value between the peak and the background, as provided by the software's analysis.

The characterization of the resolution of the imaging system has been measured along the centre and edges of the FOV when focusing on the USAF target group 7 (Figure 40), in order to verify the linear response of the system during actuation of the tunable lens which allows focusing on different imaging planes of the 30° angled target. The images display that an actuation range of up to 95 mV of the tunable lens leads to a displacement of the focal plane from -50 μm to 50 μm. At z=0 μm the tunable lens remains unactuated. The three presented figures display that the lateral resolution of the system is measured at 1.1 μm throughout the FOV for the 30° angled slide configuration.

The same edge method measurements have been repeated after removal of the prism from the USAF target in order to evaluate its impact on resolution. The FHWM results of the LSF show an identical resolution of 1.1μm throughout the three chosen locations along the full range of the tunable lens, confirming that the prism has no adverse effect in lateral resolution. An evaluation of the astigmatism reduction cannot be performed with this specific target as the chrome plated line groups are located on the surface of the slide, allowing imaging with no astigmatic features in both cases. The effect of astigmatism without the use of a prism is presented in later examples (Figure 50) where fluorescence beads mounted in antifade mixture are being imaged. It is important to note that the shadowing effects observed in the set of images in Figure 40 (b-d) are a factor of the angled target orientation and the LED back illumination that were used in the experiment. This effect is expected to be absent during light-sheet imaging with the orthogonal configuration of the optical paths.

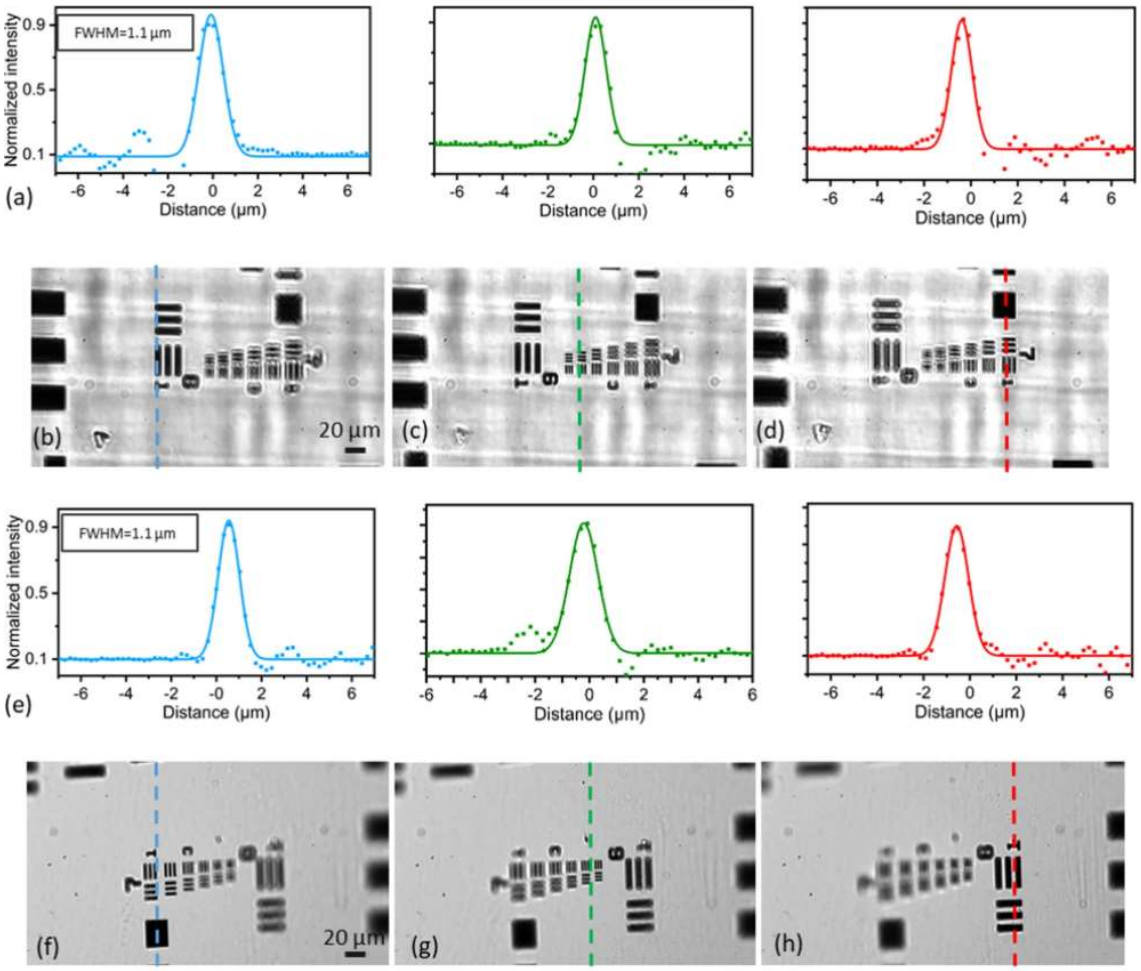

Figure 40. (a) LSFs derived at three different (b) – (d) locations of the FOV for the USAF 1951 target resulting from refocusing of the tunable lens. FHWM= 1.1 µm remains the same throughout the variation. The respective areas of the measurement are highlighted (b) z= -50µm (c) z= 0 and (d) z=50µm. (e) The same process is repeated with the removal of the prism with the respective LSFs resulting in FWHM= 1.1µm. The areas of the measurements are highlighted for (f) =-50µm , (g) z= 0 and (h) z= 50 µm.

Finally, the tunable lens is characterized within the imaging system for its full focal plane displacement potential. A target is placed in front of the objective lens and onto a 3D stage. Actuation of the lens will cause the focal plane to be translated along the imaging axis. The distance covered for a defined actuation range is recorded and illustrated in Figure 41. For the chosen range of -400 mV to 700 mV the lens can achieve a focal displacement of linear fashion. The total axial focal plane change of the imaging path is 1080 µm.

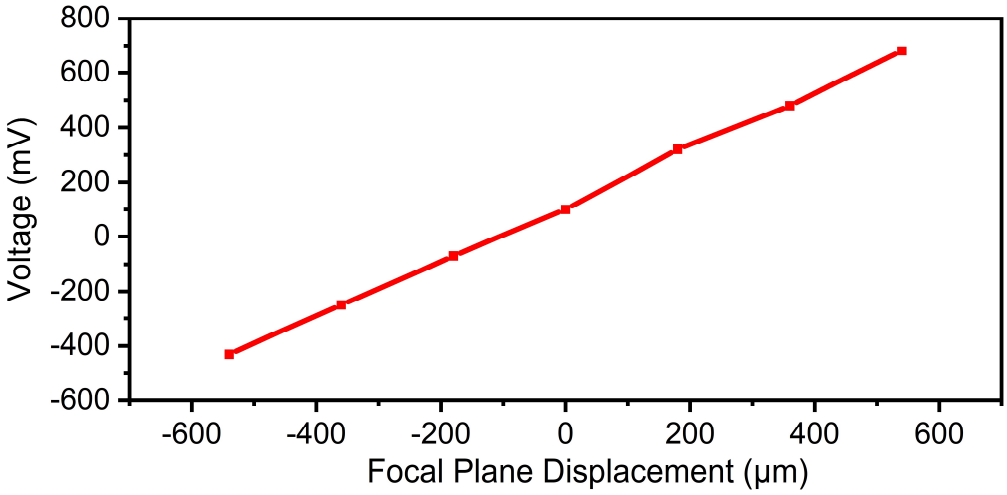

Figure 41. Charactierization of EL-3-10 tunable lens achievable focal plane shift in the setup.

4.2.5 Illumination Path Characterization

The illumination path has been characterized for its performance following a set of experimental tests. A cuvette containing fluorescein salt (Sigma Aldrich F6377) diluted in de-ionised water is placed in front of the final focusing lens in the sample space between the imaging objective and excitation lens. The cuvette is used to extract the physical information of the beam as only the part of the fluorescein mix that the beam propagates will create a fluorescence response. The imaging path characterised in chapter 4.2.4 is used for recording the results. The beam propagation without actuation of the fast MEMS axis is illustrated in Figure 42. The FWHM at the beam waist without actuating the slow MEMS axis is measured equal to 3.8 μm by plotting the profile of the single line vertical to the beam propagation axis as is shown in the Figure 42 (b) at position x0. The resulting PSFs of two more points are given as an example of comparison between the beam waist at two locations of x=50 μm and x=95 μm away along the beam propagation direction. The Gaussian characteristics of the beam can be confirmed across the FOV range.

Following this measurement method across the propagation axis will result in the graph illustrated in Figure 42 (c). The confocal parameter of the beam, extracted from the graph, is measured at 76 μm and defines the length over witch the beam radius will

increase by a factor of √2 compare to the beam waist. One additional parameter to complete the characterization of the illumination path was to observe any possible changes due to field curvature when the beam path changes between maximum actuation values in the z direction (slow MEMS axis movement). According to Figure 42 (a) the focusing point occurs with a difference of <1 μm between the central, maximum positive and maximum negative actuation, resulting in a sub-resolution difference in the different illuminated planes across the range.

The characterization of the light-sheet is achieved with actuating the fast-rotating mode of the PZ MEMS at the resonance frequency of 36.8 kHz and imaging this time the propagation beam along the y-axis. The light-sheet can reach a maximum height of 550 μm (knife edge measurement) with a voltage input of 20 V and sheet waist width equal to the beam waist FWHM of 3.8 μm.

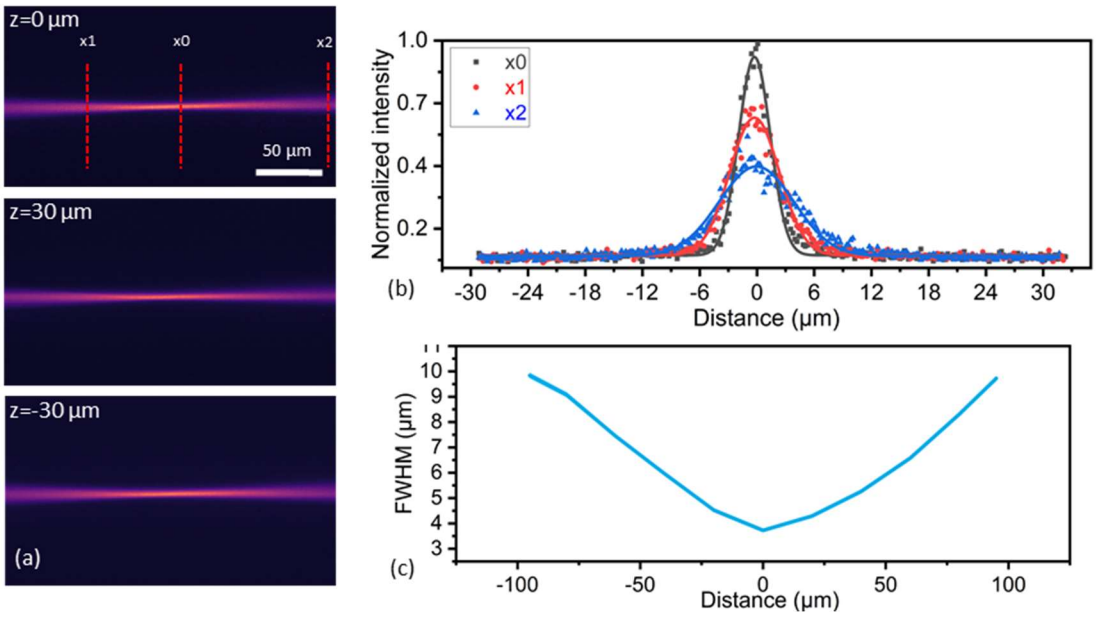

Figure 42. (a) Beam propagation through fluorescein cuvette for 3 different parallel beam paths in planes z = 0 , z=30 μm and z =-30 μm. (b) Profile plots of beam intensity along three loccations x0=0 μm x1 = -50 μm and x2 = 100 μm. A Gaussian fit has been applied to the plots with FWHM in the focusing point being equal to FWHM=3.8 μm. (c) Beam waist plot within the FOV with a derived confocal parameter of b= 76 μm.

4.3 Imaging and Results

4.3.1 Imaging Methodology and System Control

Imaging with the miniaturized LSFM system can be accomplished with a combinational movement of the optical elements in the illumination and imaging path in order to access the different planes that comprise the 3D object under investigation. This is accomplished with a software that combines the movement of the MEMS mirror and tunable lens. Achievement of this task requires control of the driving electronics for both the tunable lens and the Piezoelectric mirror, as well as synchronization of the camera to create the 3D stack. The overview of the electronics responsible for the control can be seen in Figure 43. Both the MEMS and EL-3-10 inputs are controlled with the help of an Arduino software script. Specifically, the actuation of the MEMS static rotation requires the digital commands/signals to be converted with a digital-analogue-converter (DAC) chip and amplified in order to provide the required range of operation voltages as specified in chapter 3.1.2. This is done for both the positive static angle (command “D1P”) and the negative static angle (command “D1N”). The two outputs are connected via BNC to the relevant MEMS actuator connections on either side of the MEMS. In a similar fashion the actuation of the ETL-3-10 is controlled through the same method controlling the range of the tunable lens. A second amplifier is used to achieve the range of output within the specified operation requirements. The output is then available in the form of a BNC and connected to the EL-3-10 input wires. It is important to note the resonant axis of the MEMS is controlled externally with a signal generator and sinusoidal waveform input.

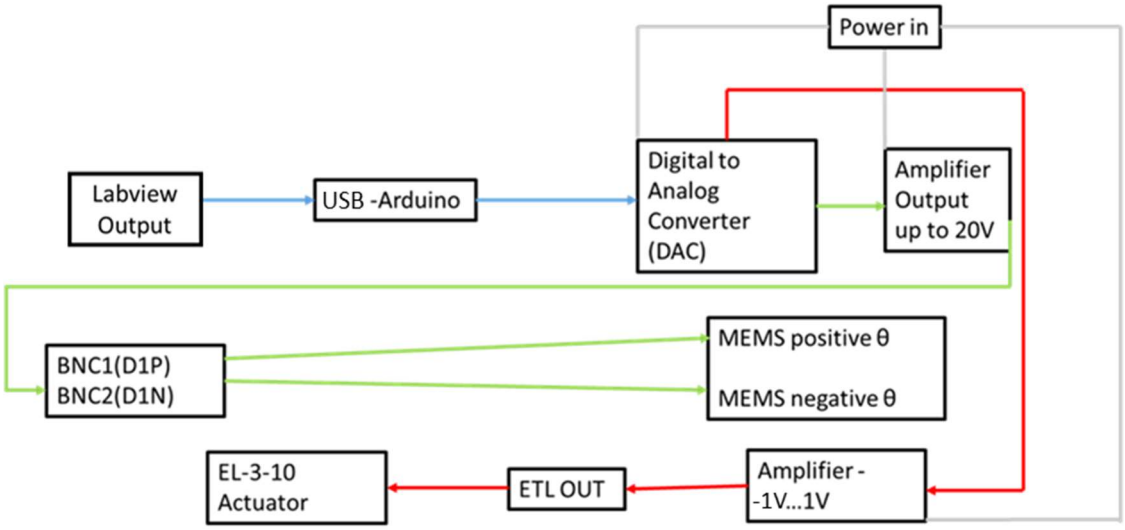

Figure 43. High-level schematic of the electronics for control of the PZ MEMS light-sheet system. (This was co-designed with Dr. Ralf Bauer.)

All of these processes are synchronized with NI LabVIEW 2016. The software methodology concept for capturing the complete 3D stack of an image is illustrated in Figure 44.

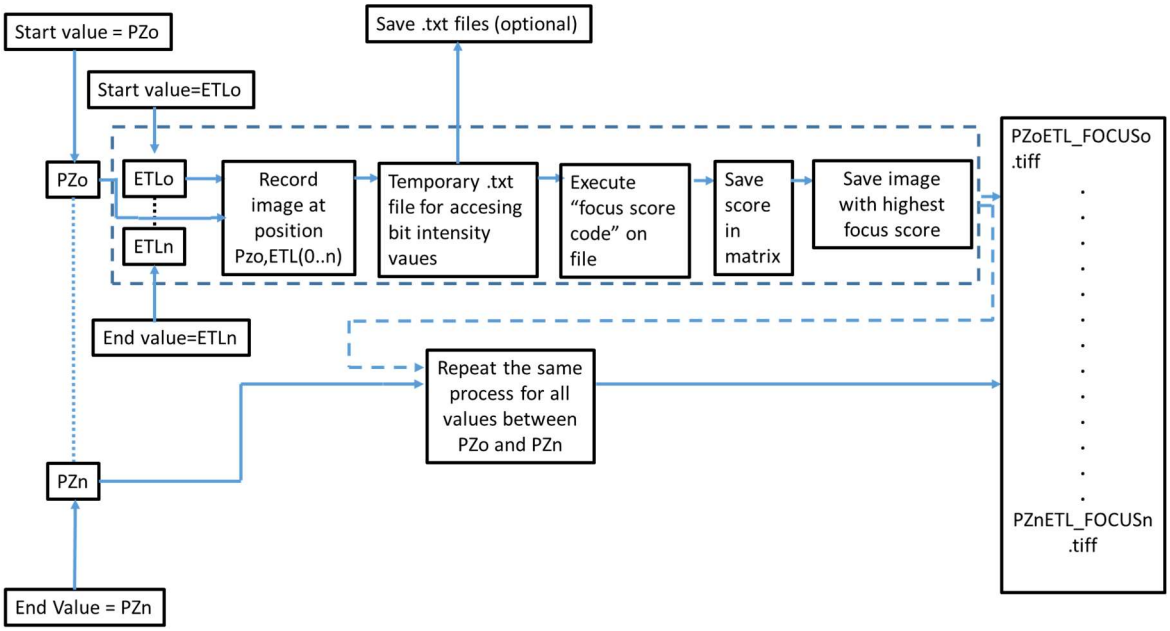

Figure 44. Flow chart/diagram of the designed LabVIEW program for image acquisition. The program is responsible for controlling the active elements of imaging while saving a stack of images within the selected range. PZo : starting value of PZ MEMS, PZn : End value of PZ MEMS, ETLo : Starting value of ETL, ETLn : End value of ETL, Dashed box : loop of collecting images with PZ value kept stable,

Dashed line: Iterative flow for the next PZ value, Temporary.txt : the image file containging the bit values.

The software works on the basis of iterative movement of the two active elements while performing an image sharpness analysis on the go for recognizing which of the images of a full imaging path focus sweep are in focus. For instance, with a given start value PZo for the piezoelectric MEMS driver, the software will run through a set of values for the tunable lens within a given range and a defined step size. The images will be evaluated on the go in terms of their sharpness based on an external MATLAB function [135], [136]read by LabVIEW. A score is given to each image and the image with the highest score is saved and considered to be the "in focus" image for the specific illuminated plane. The same process will be repeated for the next value of the PZ MEMS with a step size defined by the thickness of the light-sheet. The code will repeat itself until the last plane has been illuminated and the stack of images is saved for further analysis. It is important to note that the methodology chosen for the acquisition of the stack aimed to evaluate the non-linear relationship between the MEMS and tunable lens positioning. Manual selection of images had to be performed in cases where the MATLAB algorithm failed to recognise the in-focus slices of the stack. The acquisition of images presented in this chapter utilizes a combination of the sharpness algorithm and manual selection. This approach ensures that each z stack comprises in-focus images. It is important to note, however, that while this process successfully assigns an in-focus image to every newly illuminated plane, it does not address the non-linearity of the z stack induced by the MEMS characteristics. A dedicated post-processing correction for this non-linearity is investigated at the end of section 4.3.3, using MATLAB and the ability to shift pixel rows along a straight line. The LabVIEW user interface (UI) for the software is presented in Figure 45.

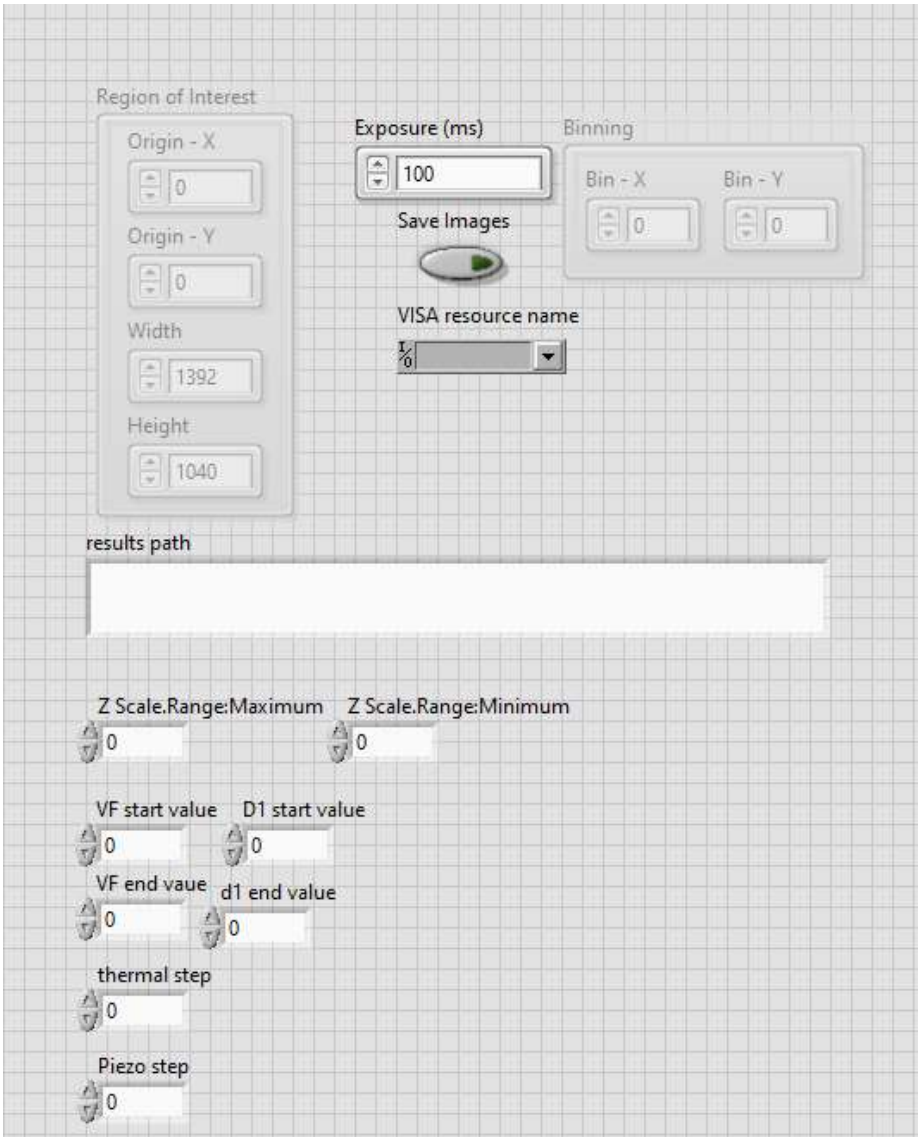

Figure 45. LabVIEW automated acquisition UI for the LSFM setup.

Synchronized 3D imaging of 15 µm beads

3D fluorescence imaging with the miniaturized LSFM setup was characterised using the Invitrogen™ FocalCheck™ Fluorescence Microscope Test Slide #1. The slide is comprised of 6 defined areas of stained microspheres ranging from 0.5 µm to 15 µm. The 15 µm diameter ring-stained microspheres are used for this experiment in order to showcase the sectioning capabilities of the light-sheet and image a set of planes for reconstruction of a 3D voxel.

Imaging of the 3D stack is centred around the z = 0 and x = 0. According to the characterization of the two optical paths this is the point where the light-sheet is focusing with the slow axis of the MEMS being unactuated. At the same time the centre of the FOV is positioned around the focused light-sheet while the plane is focused without actuation of the tunable lens.

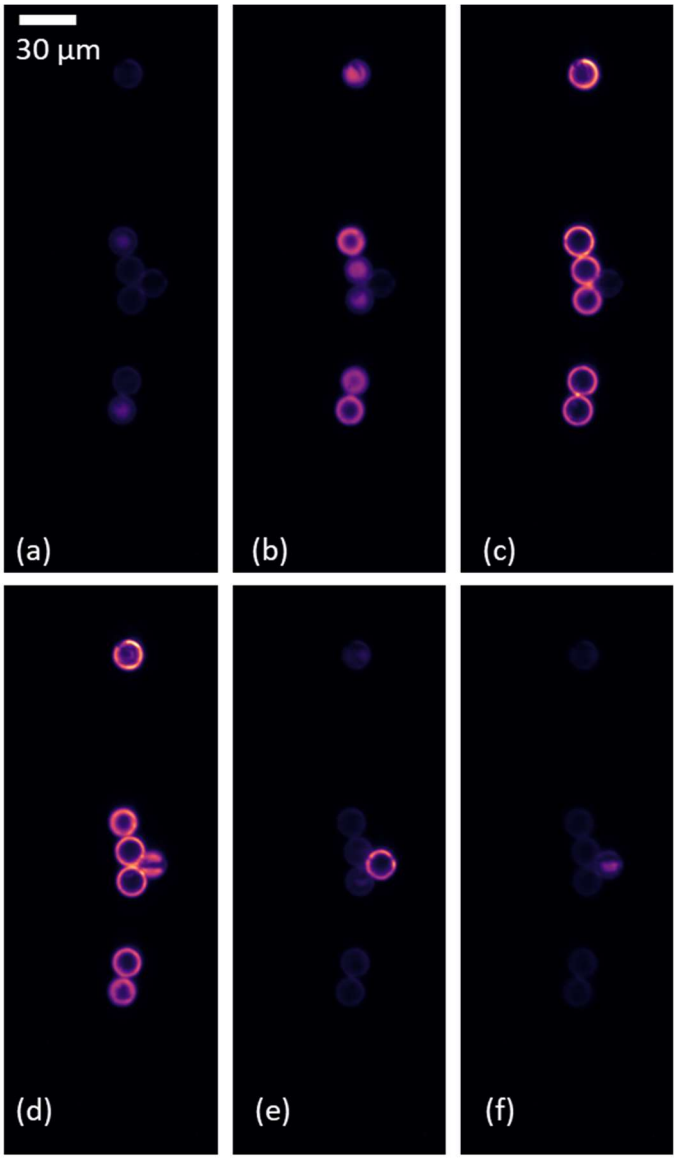

Figure 46. Progression of the light-sheet through a set of 15 µm ring stained beads at different depth location presented at points (a) z = -11 µm (b) z = -6.6 µm (c) z = -2.2 µm (d) z = 2.2 µm (e) z = 6.6 µm and (f) z =11 µm.

Once the path has been aligned the software is ready to start and collect the images along the target FOV. A set of images of the "in focus stack" is presented in Figure

46. The figure shows the progression of the scan for a group of 15 µm beads. The images shown have a difference in depth of overall 22 µm from Figure 46 (a) to Figure 46 (f) where the interval between each image of Figure 46 (a)-(f) being at 4.4 µm. It is important to note that the images are representative of a denser stack where images are collected in steps of 0.6 µm. The choice satisfies the required step size based on the Nyquist criterion for the reconstruction of a 3D image using a stack with the step size in z being not more than half of the light-sheet thickness.

The progression of the light-sheet in a single scan can be observed where planes of the beads get gradually illuminated with the slow axis movement of the PZ MEMS and are presented as in focus captures following the LabVIEW methodology presented above. The scanning fast axis is configured to provide a light-sheet height of 350µm overcovering the maximum y direction of the FOV in order to preserve uniform light-sheet intensity across the FOV. The measured power at the sample area is 0.3 mW for the 473 nm excitation laser while the combination of 2 by 2 binning and exposure time of 70 ms is set for the camera.

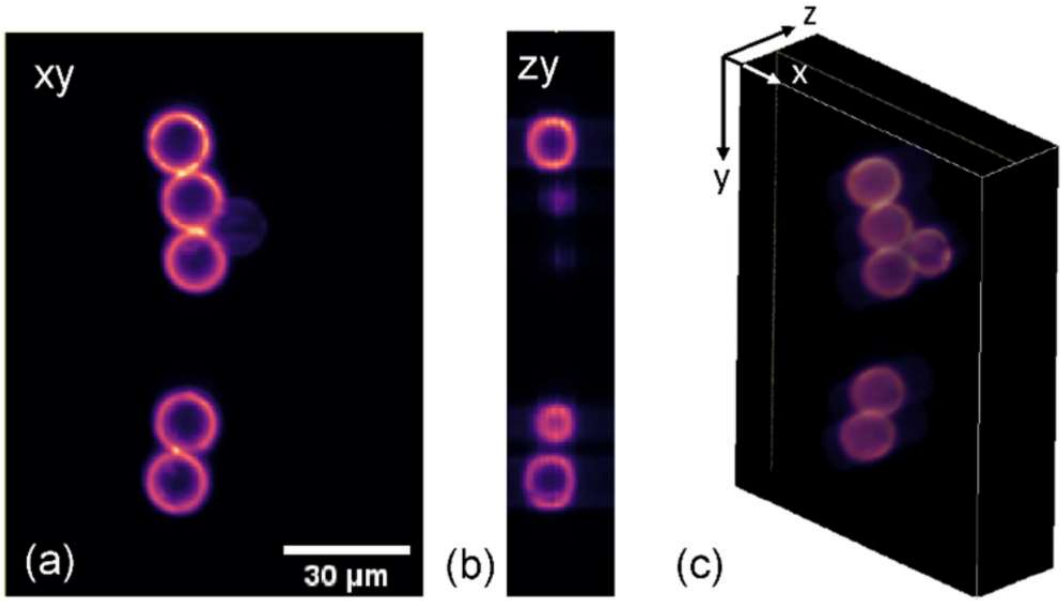

Figure 47. 15 µm bead target imaged at an angle; (a) xy slice (b) zy slice (c) xyz volume view.

Transitioning from a stack of images to a 3D volume is done using the image analysis software Fiji. A selected cropped section of the FOV is presented in Figure 47 (a) for a region of interest (ROI) of 122 μm x 165 μm. The ROI contains a group of six microbeads while their 15 μm diameter allows for a 3D reconstruction with a step size of 0.6 μm. Using the "reslice" operation of Fiji it is possible to reimage the xy coordinate stack in the zy FOV. Figure 47 (b) illustrates a selected plane of the zy coordinate plane with a ROI of 165 μm by 30 μm. The properties of the outer stained microbeads are identifiable in this example with the outer ring of the stained spheres being clearly detectable in all cases. It is also possible to use the 3D Volume viewer that provides a whole 3D voxel representation of the section. As it is presented in Figure 47 (c) the complete volume that contains the 6 beads can be exported with a combined field of view of 122 μm × 165 μm × 30 μm. Volume acquisition is completed with 0.09 volumes per second (vps). The maximum imaging speed takes into account the exposure time (70 ms), MEMS setting time (~30 ms) and a saving/communication time between the software and the computer (200 ms) for recording each of the 37 slices of this stack. With a manual adjustment of the intensity levels and removal of dead pixels the results manage to show clear sectioning ability with low background.

4.3.2 Axial and Lateral Resolution Measurements with Bead Target

Measuring sub resolution targets allows for a full characterisation of the point spread function and optical transfer function of the system. The selected sample for this experiment is the Fluoro-Max Dyed Green Aqueous Fluorescent Particles G500 sold by Thermofisher. The kit contains green fluorescent microspheres with 468 nm excitation and 508 nm emission properties. The diameter of the beads is 500 nm with less than 0.005 nm variation across the range. The beads come in a ready to use solution as a 1ml package. A protocol has been developed to allow imaging of the beads fixed in antifade solution with a diluted sample in a 3D printed sample holder. The antifade mix is used as a refractive index matching medium with n=1.52 and a similar refractive index to the prism and cover slip used in this experiment. This process aims to reduced optical aberrations that can affect the characterization of the

system. To achieve a sufficient bead density, 0.5µl of the stock solution were diluted by 1:10,000 in ProLong Glass Antifade (P36984, Fisher). The mix is evenly distributed into the nano-wells of the 3D printed holder illustrated in Figure 48. The wells are covered with a rectangular #1.5 microscope cover slip and can be used after the mix is solidified and the targeted refractive index has been achieved. According to the specifications of the antifade solution curing time can vary, with an average time of 60 hours for a mixture placed under a coverslip. The 3D printed holder is designed with the physical dimensions of a microscope slide and can be used in the same 30° orientation used for any of the prior imaging experiments.

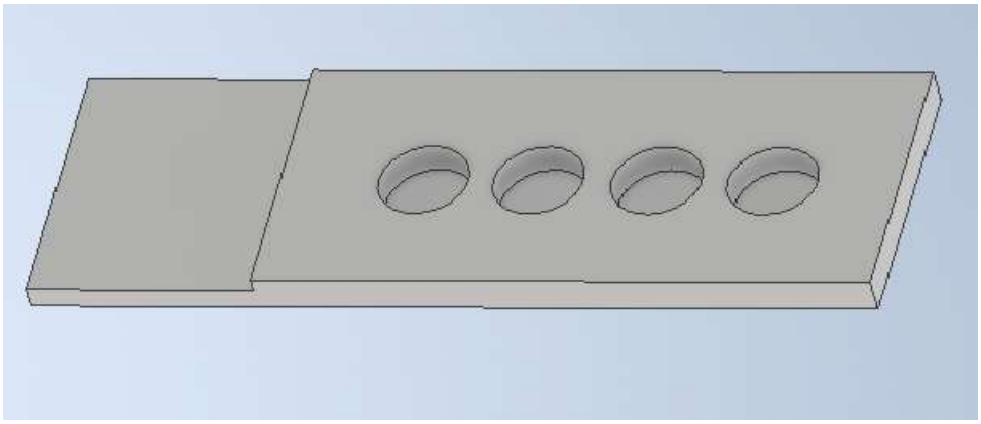

Figure 48. Custom 3D printed array of wells with the external dimensions of a microscope slide.

A single image of the target in the z plane is illustrated in Figure 49. The figure represents one slice from a stack of 40 images taken and illustrates the fluorescence outputs of the sub-resolution beads with the light-sheet positioned at a roughly 50µm depth from the cover slip. A concentration of the beads can be seen in the centre of the FOV where the synchronisation of the two active elements allows the in-focus imaging of the specific plane. Imaging of the nanobeads was implemented with a 0.3mW laser power, camera exposure of 50 ms and axial steps of 0.7µm

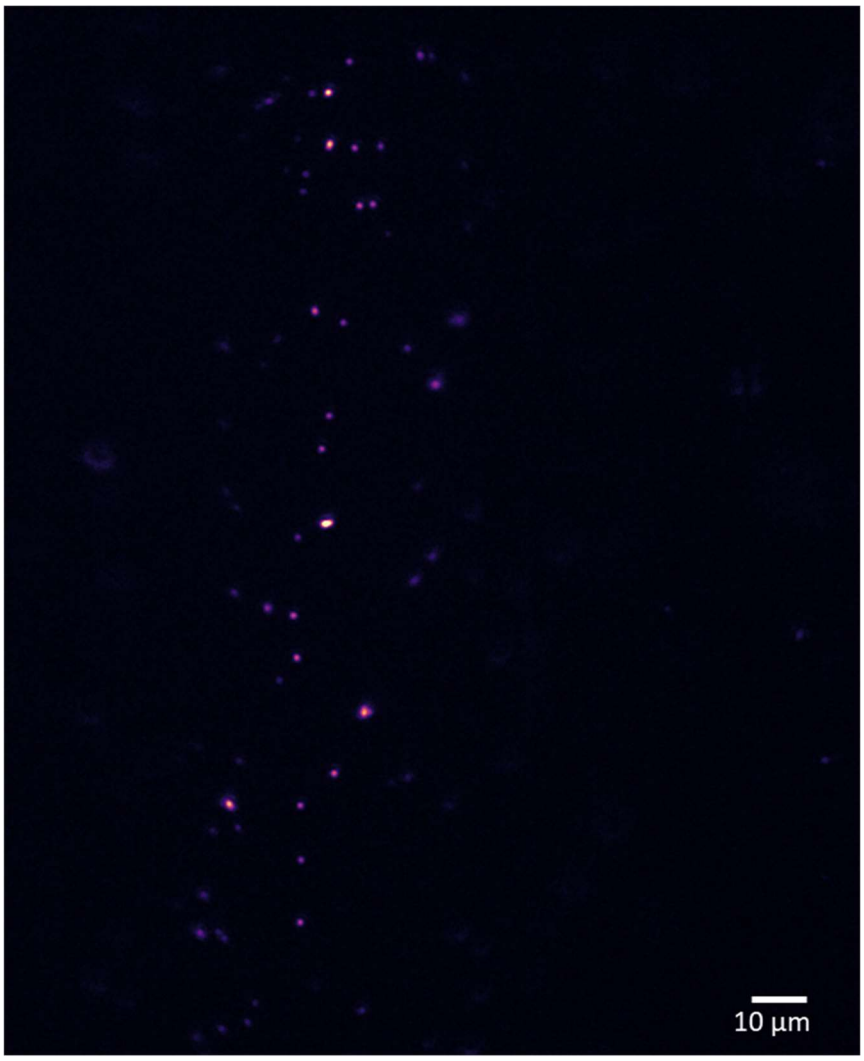

Figure 49. Single xy slice of the G500 beads.

A different way to visualize information from the whole FOV is by using the "maximum intensity projection" tool from Fiji. Here, using this test target, it is possible to evaluate directly the effect of the 3D printed prism in the system as it can be observed in Figure 50. It is evident from the results that the inclusion of the optical element in the system improves to a great extent the optical aberrations that can occur once the change between the refractive index of air and coverslip happens at an oblique angle.

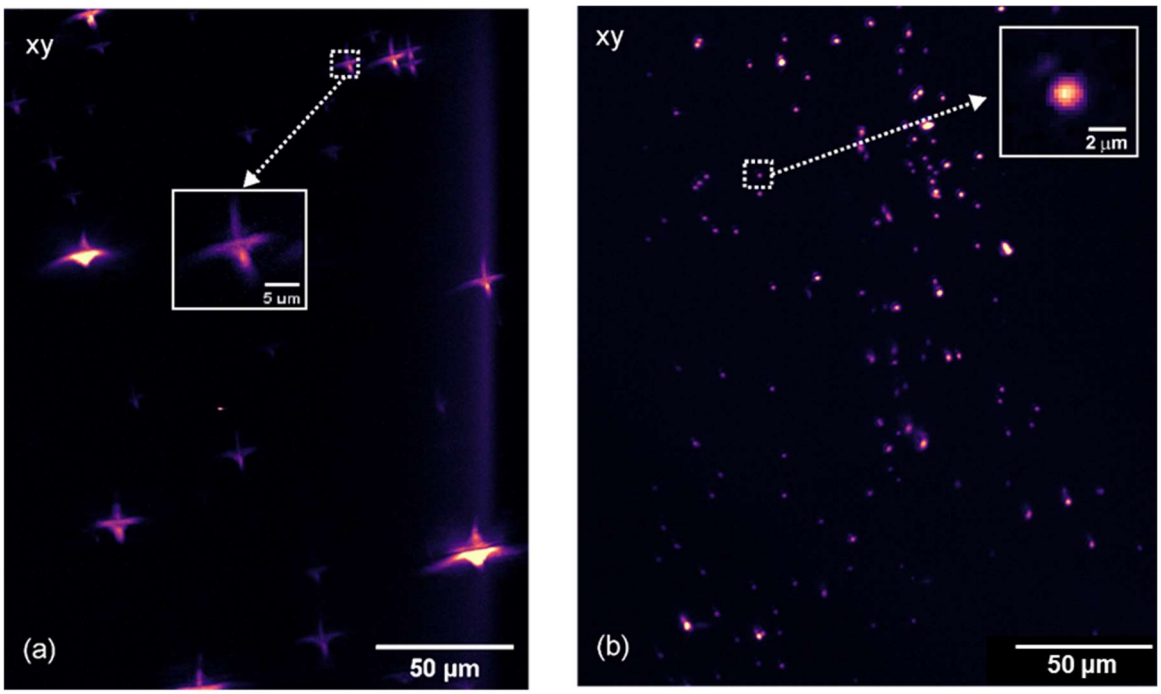

Figure 50. Comparison of nanobead images with and without the inclusion of the 3D-printed prism. (a) xy maximum intensity projection of the system without the prism showing strong astigmatism originating from the 30° angled imaging of the cover-slip mounted sample. (b) xy maximum intensity projection of the system including the 3D-printed prism.

Equally, the maximum z projection ROI presented in Figure 51 (a) provides an overview of the illuminated beads throughout the imaged volume.

To evaluate the point spread functions during fluorescence imaging, a distribution of 5 beads are analysed. An exemplary bead is illustrated in Figure 51 (b). The image contains a maximum projection of the bead in the xy plane and can be used to derive information on the lateral resolution of the imaging system. Evaluating the axial resolution of the system requires the visualization of the nanobead from the respective axis. Figure 51 c) and Figure 51 d) present a maximum intensity projection of the same bead along the xz and yz planes. Both figures are outcomes of the “reslice” tool of Fiji that reconstructs the 2D image of the chosen axis based on the 3D stack.

The intensity profile across the centre of the beads in the three figures will result to the respective PSF graphs that are illustrated in Figure 52.

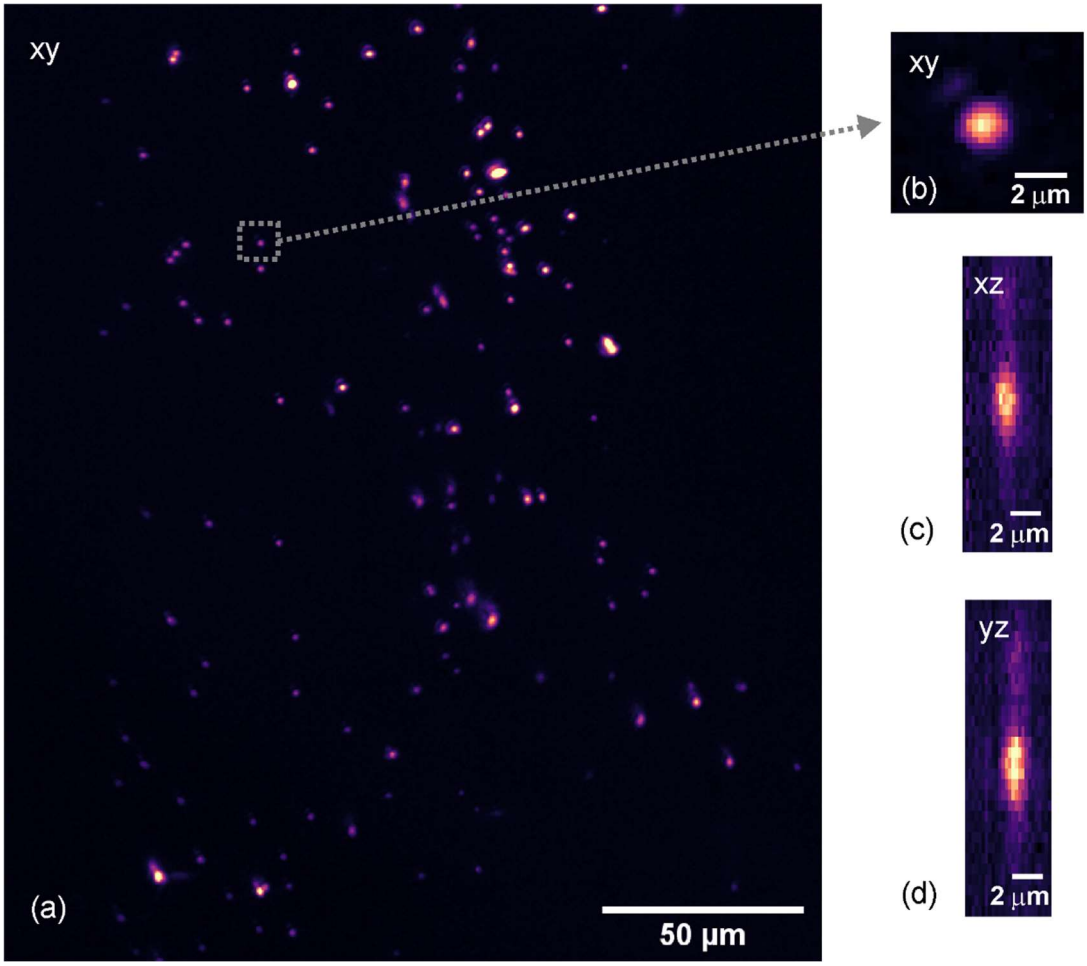

Figure 51 a) maximum projection of nanobead volume b) Single bead in xy c) xz d)yz plane.

The FWHM of the PSF for the xy plane equals to 1.1µm, which is also the lateral resolution of the system. The respective point spread functions of xz and yz planes are providing information regarding the axial resolution of the system with their PSF FWHM equal to 3.76 and 3.89 µm respectively. It is important to note that the stack of images in this experiment is processed without binning to allow a more accurate characterization of the axial and lateral resolution with a micrometre to pixel ratio of 0.225 µm.

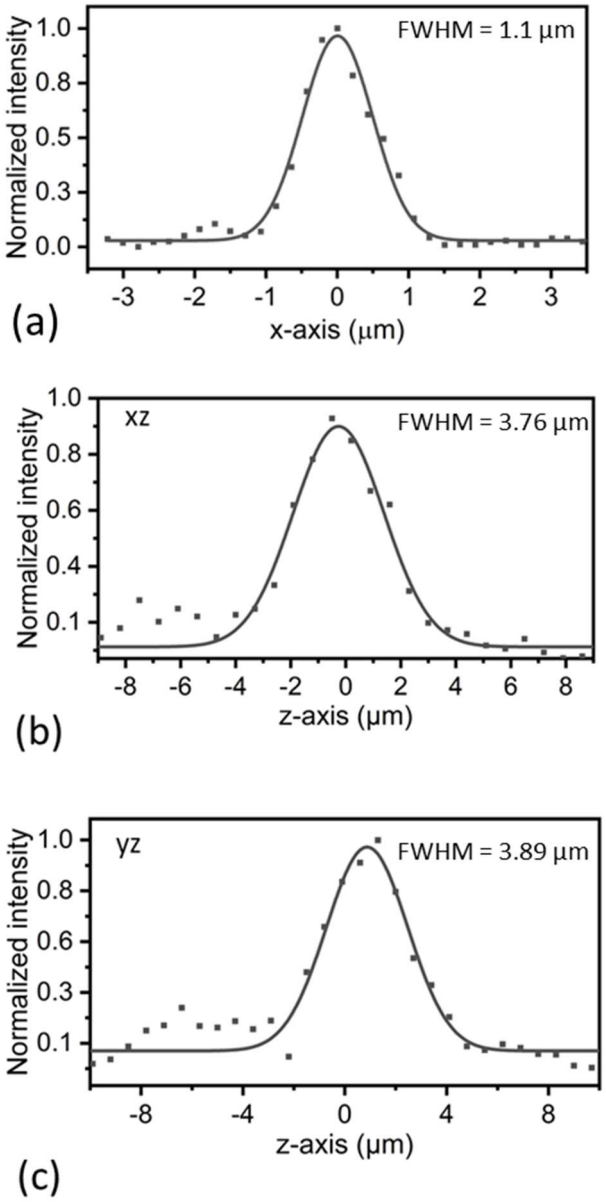

Figure 52. PSF Graphs for planes a) xy b) xz c) yz.

The lateral resolution of the system can also be used to estimate the actual numerical aperture of the imaging path. This can be done using the following formula introduced in 4.2.1:

$$NA = \frac{0.61\ x\ \lambda}{Lateral\ resolution} = \frac{0.61\ x\ 0.51\ \mu m}{1.1\ \mu m} = 0.28 \qquad (7)$$

In theory the expected NA of imaging should closely match the specified number of 0.4 on the objective lens. It is shown that in practice this number can vary and is always important to estimate it. The reason of such variation can be mainly attributed to the

manufacturing quality of an objective with such a low price, introducing aberrations in the system. The aberrations believed to cause the decreased performance of this objective are not exclusively issues of low-cost objectives but are thought to be more pronounced in them. Generally, spherical aberrations are expected when air microscope objectives are used to image samples on microscopy slides. The primary cause of this is the mismatch between the refractive index of air (n=1) and the coverslip (n≈1.5). Light rays emanating from the non-central part of the lens follow different paths due to refraction, compared to central rays. This results in different focus points for different rays, thus producing images with degraded quality. Efforts to address this issue have been proposed, such as the addition of chambers that mimic the wavefront of the detection optics using a meniscus lens [85]. Furthermore, manufacturers may incorporate correction optics within the objective lens to mitigate such aberrations, as exemplified by the Multiphoton Apochromatic Objectives with Correction Collar product line from Thorlabs. In this case, manual adjustment of a collar can be employed to correct aberrations at specific focal depths. Although such options can be beneficial, they typically necessitate a more complex optical design compared to the standard low-cost objective used in this project. This complexity is reflected in the price difference, which can span two orders of magnitude.

4.3.3 Imaging of Cell Slide

Imaging Conditions

The sample chosen for the experiments is the FluoCells® prepared slide #1 (F36924) by Thermofisher. The slide contains bovine pulmonary endothelial (BPAE) cells stained with three different fluorescent dyes. The mitochondria are stained with a red excited dye (Mitotracker Red) whereas the nuclei are stained with a blue excited dye (DAPI). Green excited fluorescent Alexa Fluor 488 phalloidin is used for staining the F-actin network with a 495 nm emission and 518 nm excitation peak. The laser power at the sample is measured at 0.3 mW. The Thorlabs CS2100M camera settings remain the same throughout the length of this subchapter with a 30 ms exposure time and 2 by 2 binning to enhance light collection from the detector and allow imaging close to Nyquist sampling.

Since the sample is contained within a standard microscope slide it can be used in the similar 30° configuration with a 3D-printed prism as coupling element as has been already introduced previously in the chapter. The previously introduced methodology also applies to the use of microscopy immersion oil for coupling the prism to the slide and positioning it in the sample area.

3D imaging

To create a 3D image of the cell slide, the combined movement of the static tilt axis of the MEMS and the change in curvature of the ETL will be used, identical to the image generation described previously. As the sample has only a thickness in the range of a couple of microns to sub-micron, the 60° angled light-sheet will only illuminate a small slice of the sample at any given time. To exemplify this, the progression of the light-sheet along 5 different planes can be seen in Figure 53. They show the light-sheet progression from a minimum light-sheet position of -30 μm in z to a maximum position of +30 μm through the static tilt angle of the MEMS. The light-sheet width increase that is observed towards the edge of the positions is only an outcome of the angled positions of the slice in the xz plane creating a depth response at different lateral positions. Specifically, as the light-sheet is scanned along z, the location of fluorescence emission is moving along different x positions for each slice. And since the light-sheet is formed by a Gaussian beam where the thickness increases away from the waist, the different xz locations show an increased thickness as well.

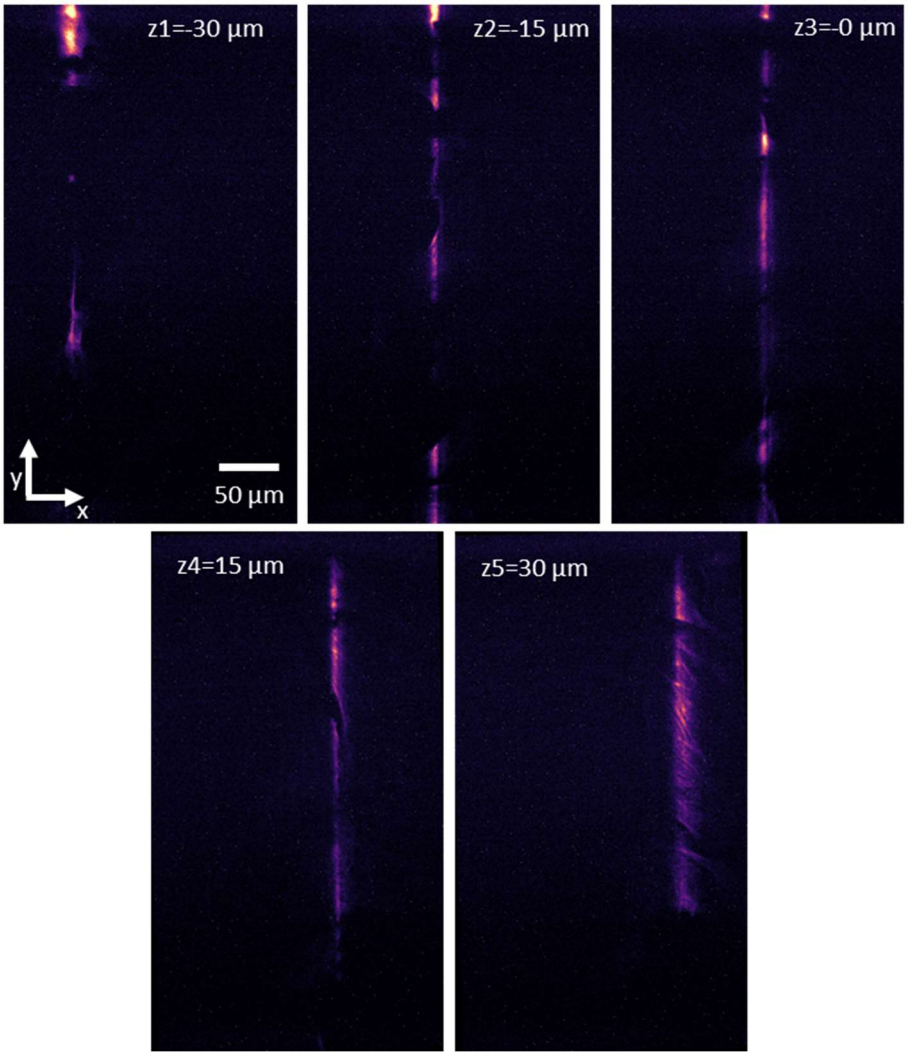

Figure 53. Light-sheet progression along different depths of the sample. The covered range in x due to the angled orientation equals 140 µm.

The fundamental tool to access information throughout the whole volume of the sample is by performing a maximum intensity projection of the image stack recorded by capturing images throughout different z-positions. The maximum intensity projection is illustrated in Figure 54 (a). The figure is rotated with y axis being the longer axis for visualisation purposes and x the shorter. The stack used for the maximum intensity projection consists of 100 images with z-steps of z = 0.6 µm. As a result, the complete imaged volume is equal to 140 x 435 x 60 μm^3. The light-sheet scanning is accomplished in 30 seconds per volume speed. The refocusing operation from image n=1 to image n=100 of the stack is addressed with a total tunable lens voltage shift equal to 0.05 V. On the illumination path the PZ MEMS slow axis input voltage used is equal to the maximum defined capability of the device with the

amplitude ranging from 15V in one actuator, to 0V, and up to 15V for the opposite actuator, for a TOSA of 3°. A closer look at a small area of the maximum intensity projection can reveal more information of the imaging system capabilities using the F-actin network. Figure 54 (b) shows the cropped highlighted area in Figure 54 (a). A 2D intensity plot over the width of the F- Actin fibres show the intensity profile illustrated in Figure 54 (c). A Gaussian function is fitted on the profile with the FWHM of 1.18 µm closely matching the lateral resolution of the system.

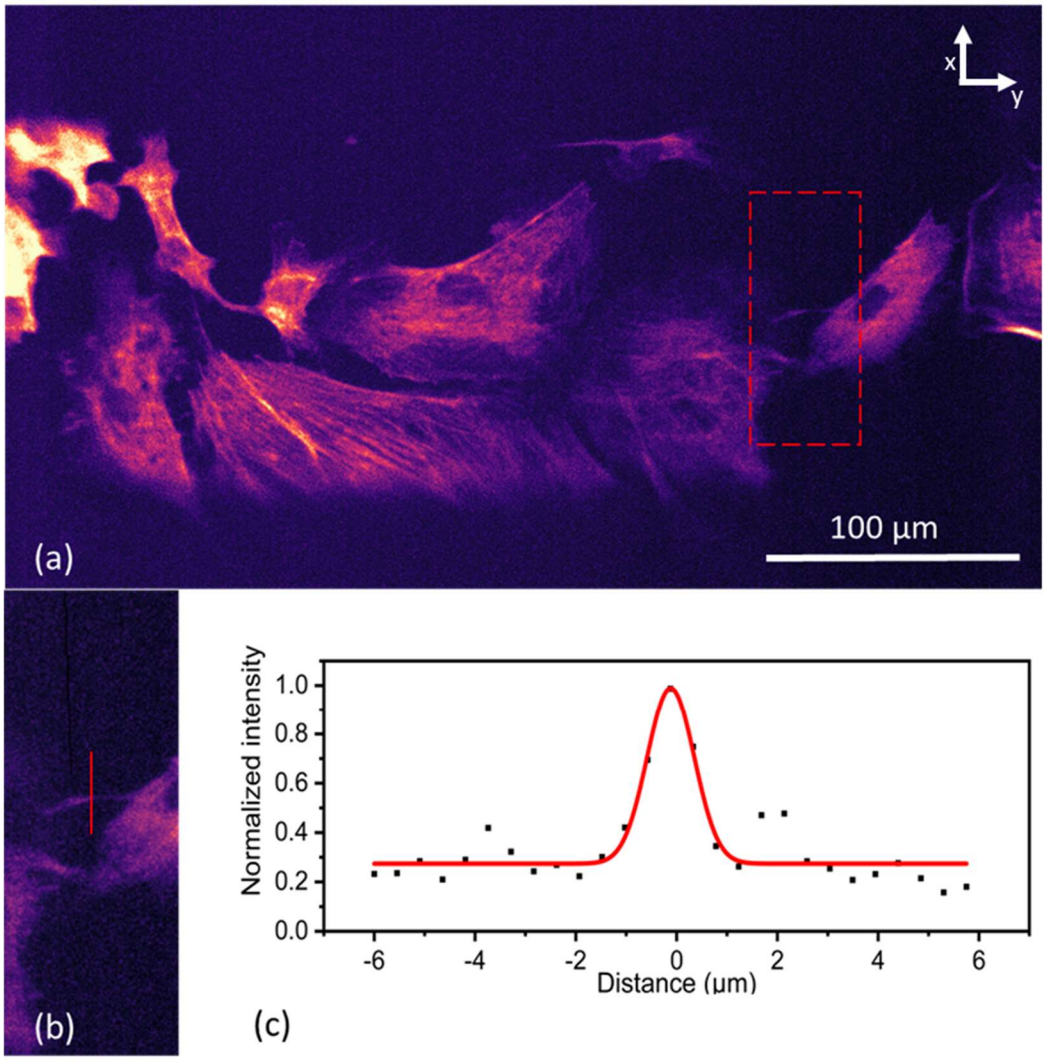

Figure 54 (a) Maximum intensity projection result for 435x140x60µm^3 volume of FluoCells® prepared slide #1. (b) ROI for F-Actin analysis (c) Intensity profile plot and Gaussian fit of F-Actin strand thickness.

Similarly, to the processing that was introduced in chapter 4.3.1 additional views of the sample can be accessed relating to the (x,z) and (y,z) view.

The maximum projection of y,z is presented in Figure 55. This view displays the angled position of the slide relative to the two optical paths. The projection is derived from a left re-slice operation (step size of 0.6μm) of the initial stack and a maximum projection of the resulted stack of n=540 figures.

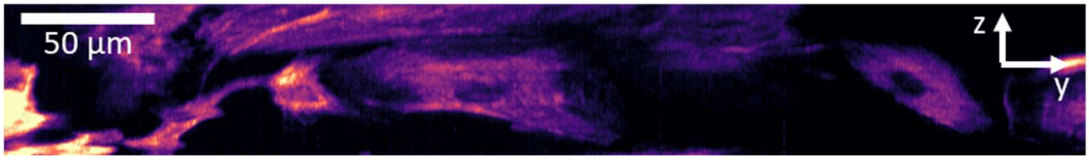

Figure 55. yz projection of the cell image in the microscope coordinate system.

Due to the physical characteristics of the sample regarding its small thickness, the zy view results in a compressed version xy view. This is mainly attributed to the almost two-dimensional sample and the angle of the slide with respect to the imaging and illumination. As there is not any resolvable information in z, the stack simply consists of the two-dimensional information transformed in the zy system. An explanatory diagram is provided in Figure 56.

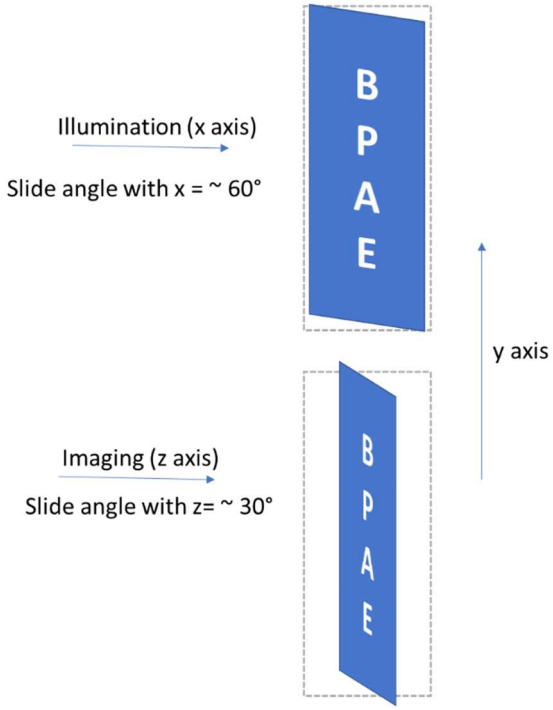

Figure 56. Explanatory schematic of the angled projection for both the xy and zy views.

A top reslice of the original stack with the same step size will result in the (x,z) maximum intensity projection (seen in Figure 58 (a)). The xz projection should ideally represent a linear response with slices being recorded at an equal rate throughout the samples volume. The sigmoid response observed is an outcome of the MEMS static angle response non-linearity as it has been noted in chapter 3.1.2. In practice this means that the MEMS angle increases near the edges of the FOV (large static angle) causing larger z steps in this area compared to the smaller steps in the central area (small static angle). A correction to this effect is applied in MATLAB. For each image of the stacks the pixel lines (x) are shifted towards the line that defines the start and end of the response using a linearization table. The outcome of this process can be seen in Figure 57 (b). The value of the measured angle is 23°.The difference between the 23° and the 30° is attributed to alignment tolerances.

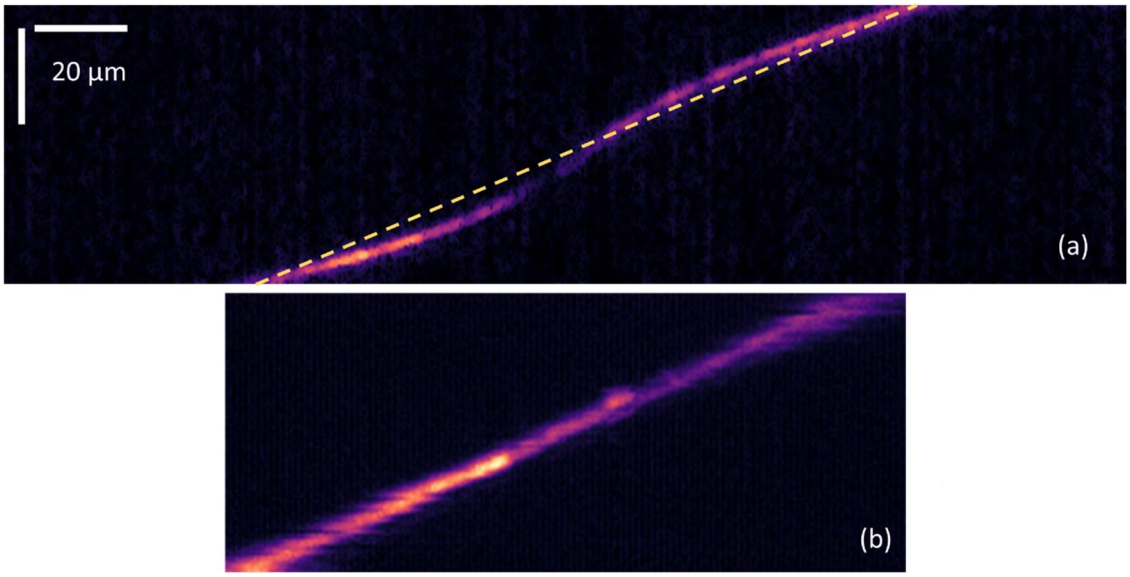

Figure 57. (a) Single xz stack image (b) xz maximum intensity projection after linearization of the response.

4.3.4 Coordinate Transform of Maximum Intensity Projection

It is important to note that even though the direct maximum intensity projections provide an understanding of the sample in the three-dimensional view of the imaged volume, their interpretation is made more complex by the fact that the instrument coordinate system deviates from the local coordinate system of the sample, which a

system user would be more used to. The imaged sample area can be defined by two coordinate systems (z , x, y) and (z' , x', y) with the first one representing the original imaging system coordinate system, defined by the imaging and illumination path, and the second one being the coordinate system defined by the microscope slide sample as it is illustrated in Figure 58. The difference between the two coordinate systems arises from the angled position of the microscope slide in the imaging area. A coordinate transform between the two systems attempts to visualise the imaging data in an alternative way better tailored to the sample in question rather than the microscopy axes. The processing method that is used to coordinate transform the imaging results is accomplished using the angled reslice operation of Fiji.

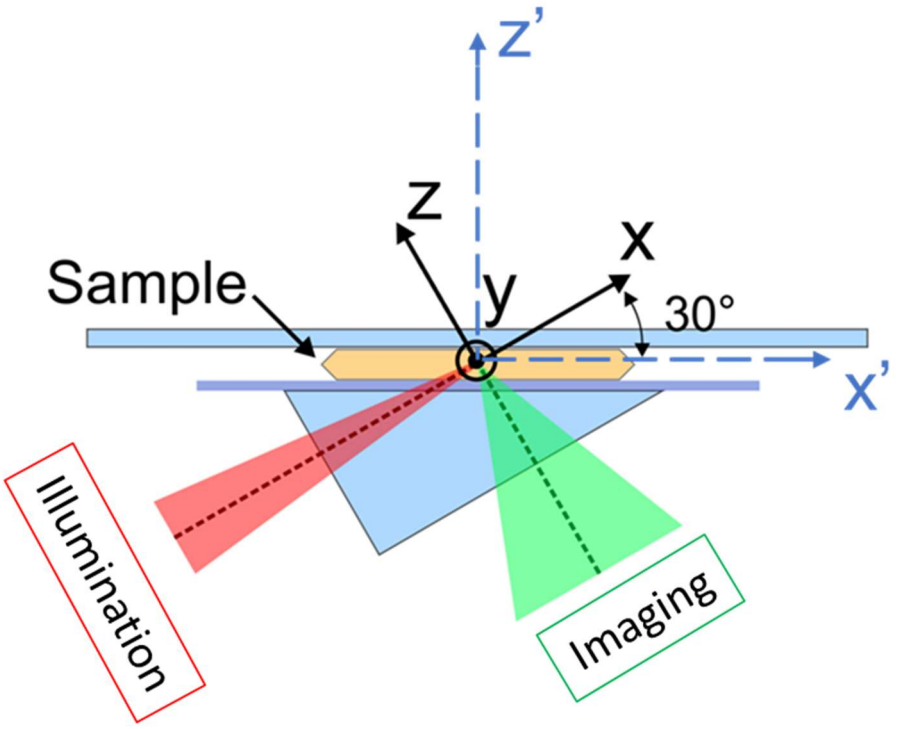

Figure 58. Coordinate transform schematic from microscope coordinate system (z, x) to slide coordinate system (z', x').

Considering microscopy as a sample centric tool it is important to create a coordinate system where the sample axes define the presentation of the results. In this way the sample physical characteristics will be viewed in their truest form and avoid possible confusion during the interpretation of the result. The way to do this is by performing a coordinate transform of 23° according to the methodology presented below.

The first step is to acquire a homogenous voxel size for the stack. Scaling of z by 1.3274 will result in a homogenous voxel size of 0.452 µm³. This will result in Figure 59 (a). An angled re-slice can now be acquired for the stack by plotting a line parallel to the xz response at the angle of 23°. The line should be long enough to match the length of response in order to avoid cropping during the rotation. The step size of the re-slice is kept equal to the voxel size at 0.452 µm. The result of the re-slice can be seen in Figure 59 (b). The relationship between x/x' is by a factor of cos (23°) = 0.94 making x'y' = 148.9 µm x 435 µm. Accessing the depth characteristics of the sample in z' is possible with the reslice operation as it is illustrated with the 'left reslice' used for Figure 59 (c).

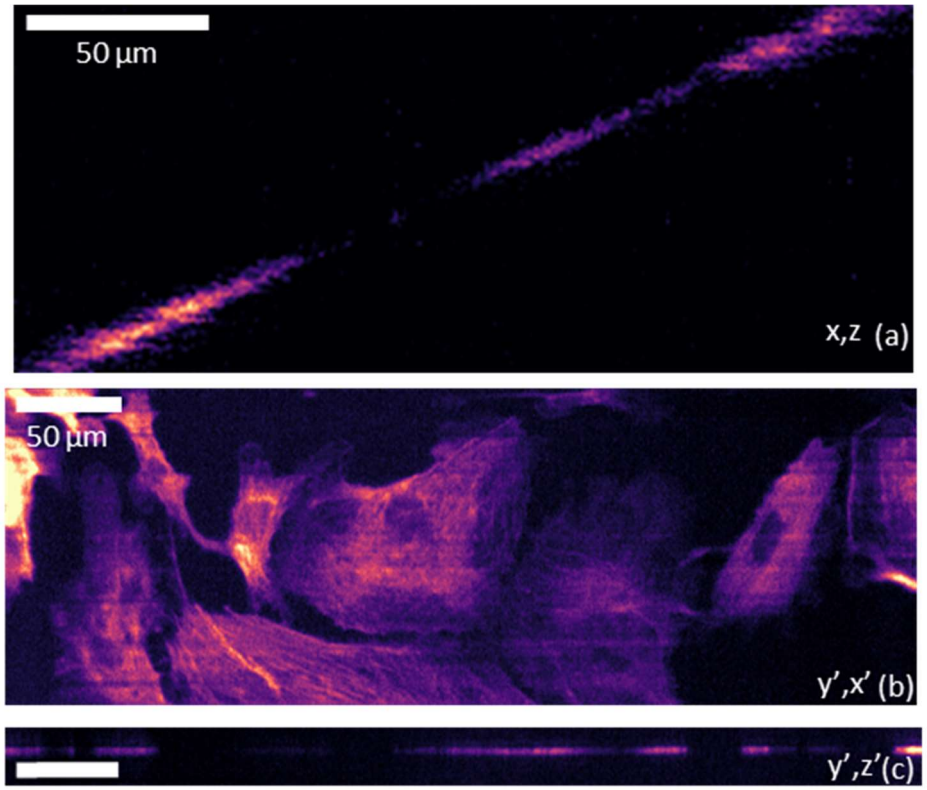

Figure 59 (a) zx slice with scaled z to attain homogeneous voxel size. (b) Outcome of 23° angled top re-slice of zx resulting in the transformed coordinate system of x'y'. (c) y'z' projection (scale bar of 50 µm).

The attained results show the BPAE cell slide imaged using the coordinates of the sample allowing for a more typical view of the sample. Using the y'x' maximum projection as an example and comparing it with the maximum projection obtained in the original coordinate transfer, it is evident that the rotation of the stack by the 23°

angle has mainly affected the ratio of the view as expected. In the case of the y'z' projection the expectance of the information received in that case is relating to the physical characteristics of the sample along its "depth" after the performed rotation. Unfortunately, in the case of as thin samples as the 2D monolayer used, the thickness of the sample is below the light-sheet width, making it challenging to estimate this value.

4.4 Summary

The first sections of this chapter covered the steps needed towards the design of a miniaturized LSFM system with the use of a PZ MEMS as the active element for the generation and lateral translation of the light-sheet in the illumination path, and a tunable lens as the active element of refocusing in the imaging path. Specifically, the optical design simulation was presented with the simulation outcomes on the beam focusing, telecentricity and field-curvature. Additionally, the chapter covered the equipment and methods used in the implementation of the microscopy system. Furthermore, a complete characterization of the two optical paths was presented with a focus on the integration and performance of the two active elements used respectively. Finally, the methods and outcomes of imaging a set of samples was presented with a focus on the evaluation of the system's characteristics and performance. Nanobeads were used to evaluate the lateral and axial PSF of the system whereas a cell sample was used to investigate the 3D capabilities and imaging options that this solution can provide.

5 Axially-scanning MEMS Light-sheet Microscopy

5.1 Introduction

This chapter explores a series of developments implemented to enhance the miniaturized LSFM system presented in Chapter 4, with the aim of improving its performance in specific areas. A primary focus is on extending the maximum achievable light-sheet translation along the z axis, as this directly leads to an expanded imaging volume. To achieve this, the use of an alternative MEMS mirror capable of larger TOSA angles without compromising light-sheet height generation is proposed. The electrothermal mirror introduced in Chapter 3.2 meets these criteria and is thus selected as the active element responsible for both light-sheet generation and translation in this new iteration of the microscopy system. A key innovation investigated in this version of the miniaturized LSFM is the integration of an electrically tunable lens in the illumination path, complementing the existing tunable lens in the imaging path. This additional lens aims to provide precise control over the beam waist position, enabling the generation of thin light-sheet slices across the entire imaging FOV. This enhancement addresses the challenge of Gaussian beam expansion towards the FOV edges. For this purpose, the Optotune EL-3-10, previously described in Section 2.3.1, is employed. Additionally, the lenses comprising the 4f system in the illumination path are replaced to achieve a more balanced FWHM of the light sheet. This modification aims to implement tiling more effectively and ultimately achieve a more homogeneous thickness across the FOV, as will be explored in later sections. Furthermore, a redesign of the imaging path is presented, incorporating an alternative camera and tunable lens combination. This modification explores potential improvements in imaging results, particularly in noise reduction and aberration correction. A camera with a larger sCMOS sensor is utilized to capture an expanded FOV, as detailed later in this chapter. The EL-10-30 tunable lens, introduced in Section 2.3.2, serves as the primary active element in the imaging path for refocusing. Its larger

aperture is designed to accommodate the increased FOV and mitigate the possibility of image propagation issues. Additional enhancements include the integration of a new 488 nm laser source to improve illumination beam stability. The optical path in the illumination arm has been redesigned to accommodate these newly introduced elements, optimizing overall system performance. Finally, changes are implemented in the image acquisition and processing workflows. A new LabVIEW program aims to reduce device synchronization times and increase automation during imaging. Similarly, a new protocol for the correction of non-linearities and presentation of the 3D volume in the traditional microscopy axes is provided, aiming to achieve a more efficient and user-friendly solution. These design choices collectively address specific limitations of the previous system while expanding its capabilities, potentially leading to improved imaging quality and a more versatile LSFM setup. The following sections will provide detailed analyses of each modification, their implementation, and their impact on system performance.

5.2 Design

The 2D schematic of the scanning LSFM system is illustrated in Figure 60. The design of the microscope is based on the DSLM light-sheet method with the light-sheet being an outcome of the fast-axial rotation of one axis of the thermal MEMS mirror. The 20x microscope objective is responsible for collecting the image generated at the illuminated plane and transmitting it towards the camera detector. The design of this setup aims on improvements in the implementation of two paths with the active elements that are being used. The thermal MEMS mirror has the ability to translate the light-sheet in the z axis, accessing planes parallel to the original scanned light-sheet illumination that can be imaged with the addition of a refocusing tunable lens in the imaging path. The combined movement of the two elements will enable 3D imaging without the need of a translational stage, identical to the concept in chapter 4.

Additionally, the tunable lens that is incorporated into the illumination design before the final focusing lens can change the beam waist position, providing an option for thinner sectioning especially near the edges of the FOV, where otherwise the tightly focused Gaussian beam will suffer from considerable divergence leading to the illumination of thicker planes and reduced control over the imaged volume. After the

initial 3D imaging scan with the beam waist cantered in the FOV, it is possible to repeat the scan one or two more times with the illumination beam waist axially shifted in 2 or 3 positions along x. With appropriate image stitching the volume will be presented with less Gaussian light-sheet divergence and ultimately be able to show sectioning with improved uniformity throughout the imaged volume.

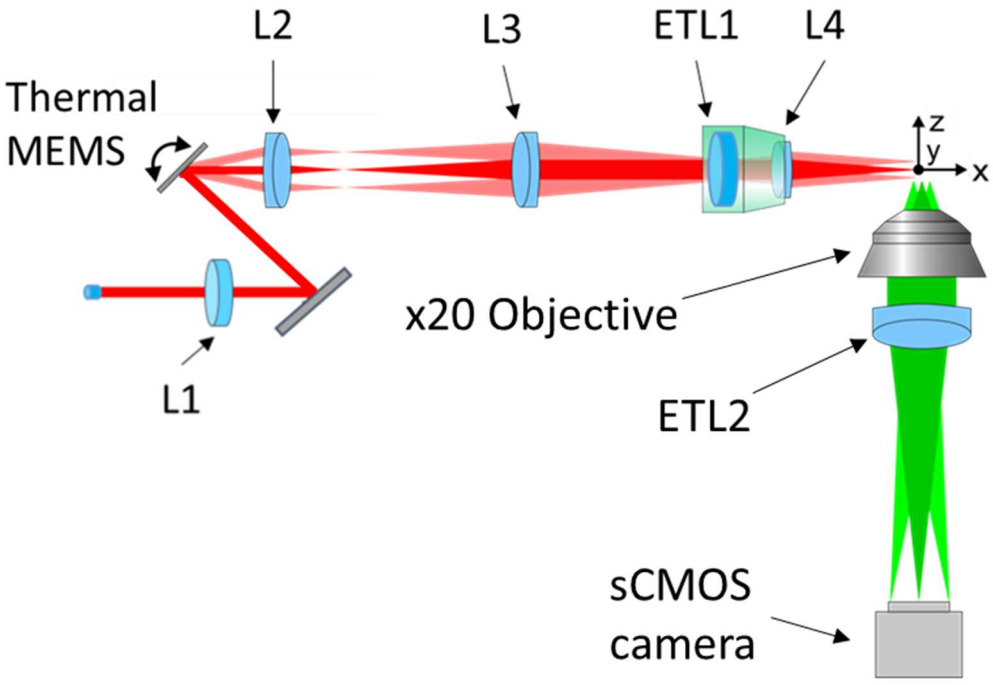

Figure 60. 2D schematic of the "Axially scanning MEMS LSFM system". Illumination path (red): A collimated beam is transmitted towards the curvature correction lens L1 with f = 50 mm followed by a flat mirror positioned at 20°. The optical path will reflect at the 20° angled thermal MEMS mirror and enter the 4f telecentric setup consisting of lenses L2 (f=10), L3 (f =19) and focusing lens L4 (f=10). Tunable lens ETL1 is positioned in the back-aperture before the focusing lens to vary the focus position of the light-sheet. The imaging path (green) is aligned orthogonally to the illumination path with the x20 objective projecting the illuminated plane image onto the sCMOS camera sensor. The tunable lens ETL2 placed between the two elements is responsible for refocusing to the next illuminated plane along z during 3D imaging.

5.2.1 Imaging Path Design

The design of the imaging path follows a methodology similar to that described in section 4.2.1. A series of optical element modifications are implemented to enhance imaging performance, particularly in terms of contrast and field of view. Contrast, as a function of light gathering, was an aspect where the microscope designed in 4.2.1 encountered certain limitations, necessitating the implementation of binning to capture acceptable quality images, especially when imaging cell samples. Furthermore, the potential for a wider field of view in sectioning, resulting from developments in the illumination path, needs to be accommodated in the design. An extended FOV combined with the new sectioning abilities can potentially increase the performance on the system with a larger imaged volume. It is important to note that the increased FOV should not sacrifice the resolving power of the system. The resolving power in theory is only affected by the objective whereas the FOV is a fraction of the sensor size and the magnification. The FOV using a 20x objective and a 1/1.2 inches camera (IDS UI-3060CP Rev. 2) can be estimated as follows. For a direct comparison between the two imaging paths, only the camera and objective lens are taken into consideration for the estimation of the FOV.

$$FOV = \frac{Sensor\ size}{Magnifcation\ factor} = \frac{11.345\ mm\ x\ 7.126\ mm}{20}$$
$$= 0.567mm\ x\ 0.356mm$$

This will lead to an estimated 19 % FOV increase in the horizontal axis and 30 % FOV increase in the vertical axis compared to the Thorlabs sCMOS camera used in chapter 4.

In order to accommodate the larger FOV and additionally aim to increase the signal in imaging, a new tunable lens will be used in the imaging path. The EL-10-30 introduced in 3.3.2 has a larger aperture diameter than the EL-3-10 and will be the active element responsible for refocusing subsequent planes during the translation of the light-sheet along z. The lens will be positioned at the back aperture of the previously used

economy Newport MVC-20 objective. The imaging path will be completed with a Chroma 69401m triple band filter that is coupled in the front threading of the IDS UI-3060CP camera with the distance between the two pairs of elements being set at 160 mm. All the optical elements of the imaging path are housed in a 30 mm diameter lens tube to reduce ambient light entering the camera sensor and ensure undisrupted alignment of the optical path.

5.2.2 Illumination Path Design

The Optalix ray tracing design for the illumination path is illustrated in Figure 61. The optical path is designed with off the shelves optics that meet the basic requirements of being inexpensive and compact.

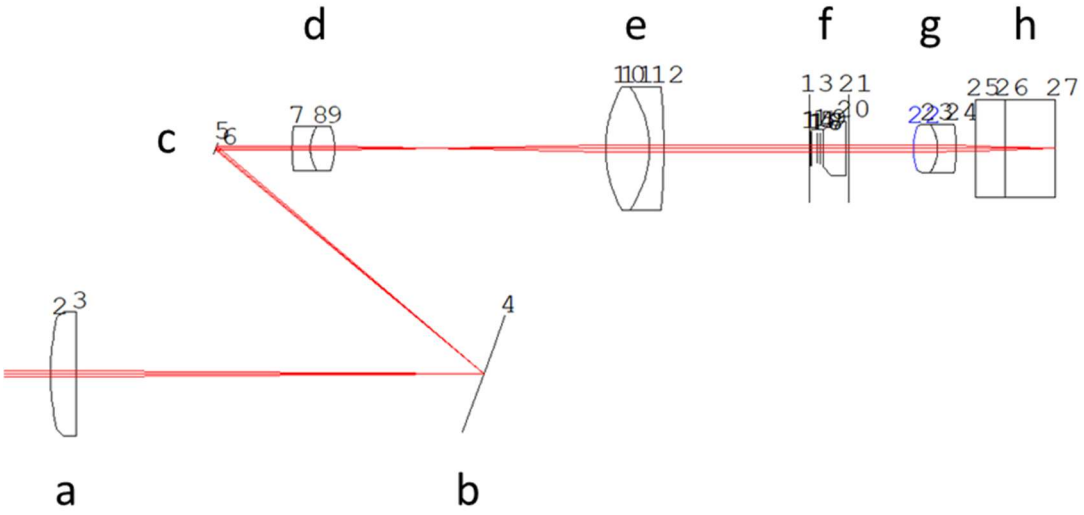

Figure 61. Optalix optical design of the illumination path, optimized to result in a telecentric setup with : a – 50 mm curvature compensation lens, b - mirror, c - 2d electrothermal MEMS, d – 10 mm achromatic lens, e – 19 mm achromat lens, f – ETL, g - 10 mm achromatic lens, h – medium (slide sample).

According to the illumination path design introduced in 3.2.2 the choice of small aperture lenses, over an illumination objective, aims to allow the use of angled microscope slides while keeping the cost low. Furthermore, the lenses should provide adequate working distance to enable imaging in the suggested configuration.

For the purpose of this design, the collimator used is the F110FC-532 that provides an output beam waist equal to 0.65 mm FWHM (1.1 mm $1/e^2$ beam diameter). The collimated beam is transmitted towards a plano convex lens with focal length of 50 mm followed by a flat mirror at 20° angle that reflects the beam towards the thermal MEMS. This plano convex lens / flat mirror configuration aims to pre-compensate for the curved surface of the thermal MEMS by introducing a 2f path and ensuring that the beam is collimated after the MEMS and before entering the telecentric setup. As it has been introduced in 3.2.1 the thermal mirror features a curved surface with a ROC equal to 65 mm. This would mean that any collimated beam that directly reflects off the MEMS mirror would be focused with an estimated focal length of a curved mirror f=ROC/2=32.5 mm.

The 2f distance is theoretically expected to result in an 82.5 mm total distance between the two elements. In Optalix (Figure 62) the f = 50 mm lens is positioned in an optimized distance 42mm away from the mirror which itself has a distance of 36 mm from the curved MEMS accounting for a total distance of 78 mm. The result of this alignment leads to the collimated beam of 0.42 mm FWHM entering the 4f telecentric setup. Differences between the theoretical simulation can be attributed to the introduced angle of the MEMS that can affect the result of the curved mirror focal length with the introduction of possible astigmatism. Even though astigmatism is an undesired effect in the design, the introduced angle between the two elements is deemed essential for the practical implementation of the setup. Limiting the effect of astigmatism can be achieved with the incident angle being kept to the lowest number in practice. For this reason, the 20° angle is chosen.

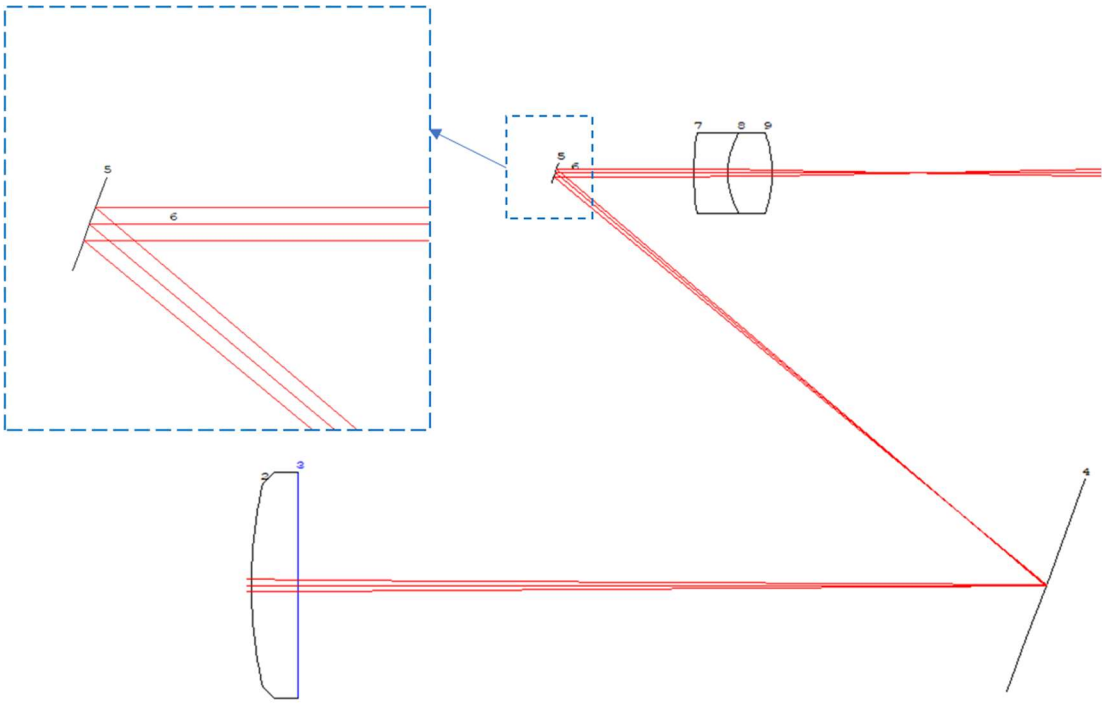

Figure 62. Optalix optical design section showcasing the three elements (f=50 mm lens, flat mirror, and Thermal MEMS) needed for beam collimation. Highlighted is the result of the collimation.

The collimated beam will enter the 4f telecentric setup consisting of three lenses placed at 2f distances between each other and optimized for providing the thinnest beam waist whilst the optical path remains telecentric. The off-the-shelf lenses chosen for the design are the 5 mm diameter, f = 10 mm (Thorlabs AC050-010-A) achromats that are used twice (first and focusing lens) and the AC127-019-A achromat with 12.7mm diameter and f = 19 mm. According to the Optalix optimization the distance between the first f = 10 mm lens and the f = 19 mm lens is set at 27.9 mm, with the focusing lens positioned a further 25.9 mm away. The EL-3-10 is also positioned within the 4f setup in the back focal plane of the focusing lens with the distance between the two elements being set at 6.7 mm. It is important to note that as part of this analysis the ETL is assumed unactuated and has no effect to the optical path. The effect of the ETL as part of the optical path will be analysed in the following sections. The design includes an approximated design of the fluorescein cuvette used for the real-life characterization of the optical path in an effort to closely match the results of the simulation and experimental characterization. The cuvette design consists of a 1.25 mm thick PMMA wall followed by water. The result of the simulation shows an

expected focusing point of the beam at a distance of 9.4 mm away from the focusing lens. The Gaussian beam profile at this point is illustrated in Figure 63. The beam features a FWHM of 6.4 μm that is expected to be the minimum light-sheet thickness at the centre of the FOV.

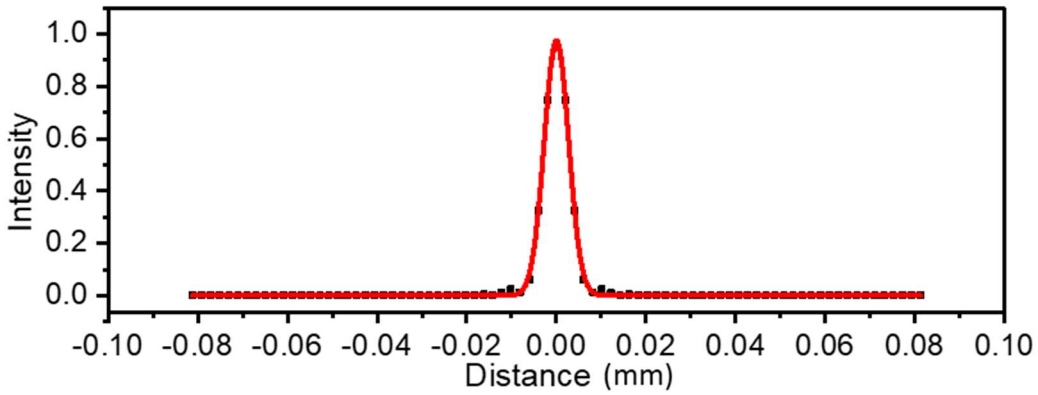

Figure 63. Beam profile cross section from Optalix at the centre of the beam waist showcasing a FWHM of 6.4 μm.

It is important to note that the beam waist thickness actual value can vary to the theoretical one due to factors such as the size of the input beam as it has been shown in the previous chapter, and in this case the curvature and position of the curved mirror in the optical path.

Enabling the movement of the MEMS around a static angle as a variable within the Optalix design will allow an insight in the maximum expected light-sheet translation at the imaging area. Specifically, according to 3.2.2 the thermal MEMS can achieve maximum angles up to 4° TOSA per movement direction that will lead to the maximum translated paths shown in Figure 64. The distance is measured at 0.72 mm for a transition of the MEMS angles of a TOSA equal to 8° (-4 to +4). The maximum translated paths will reach the focus point at a 0.08 mm shorter length compared to the central path.

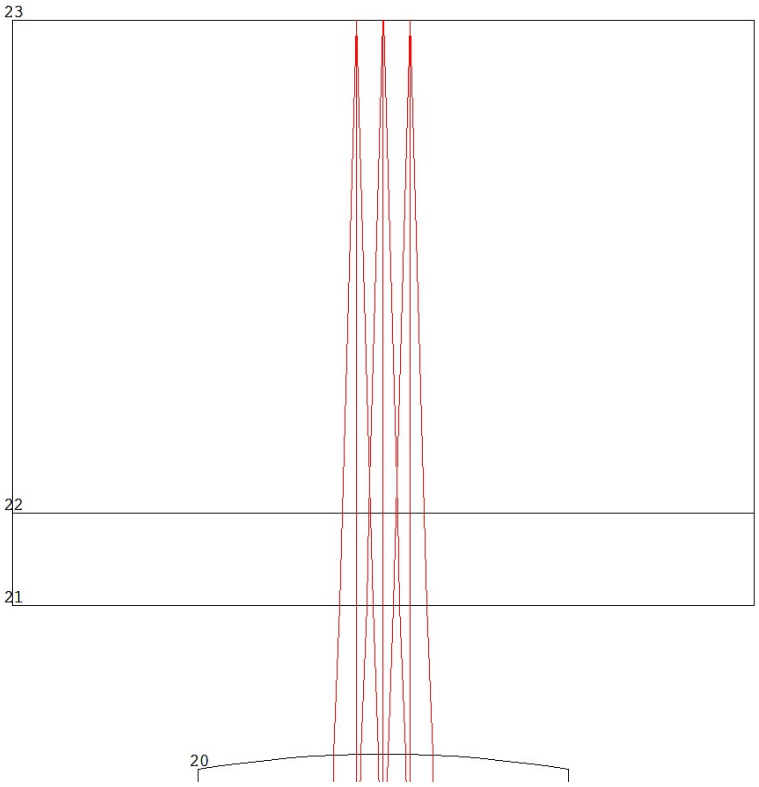

Figure 64. Beam focusing for the three different paths that result when the MEMS mirror is rotated at -4°, 0° and 4°.

5.2.3 Design Implementation

The illumination source chosen for the design is an OdicForce 488 nm source with a controllable power up to a maximum of 60 mW. The laser is fiber coupled using a F110FC-532 fiber.

The implementation of the microscope setup (Figure 65) aims to provide a stable and secure fitting of the components while making use of the limited space available due to the miniaturized footprint. Specifically, all the optical components are mounted on a Thorlabs MB2530/M breadboard with a total available area of 250 mm x 300 mm. Mounting of the optics is accomplished with posts and postholders whereas the optical components are housed either in off the shelf mirror mounts or custom 3D printed designs.

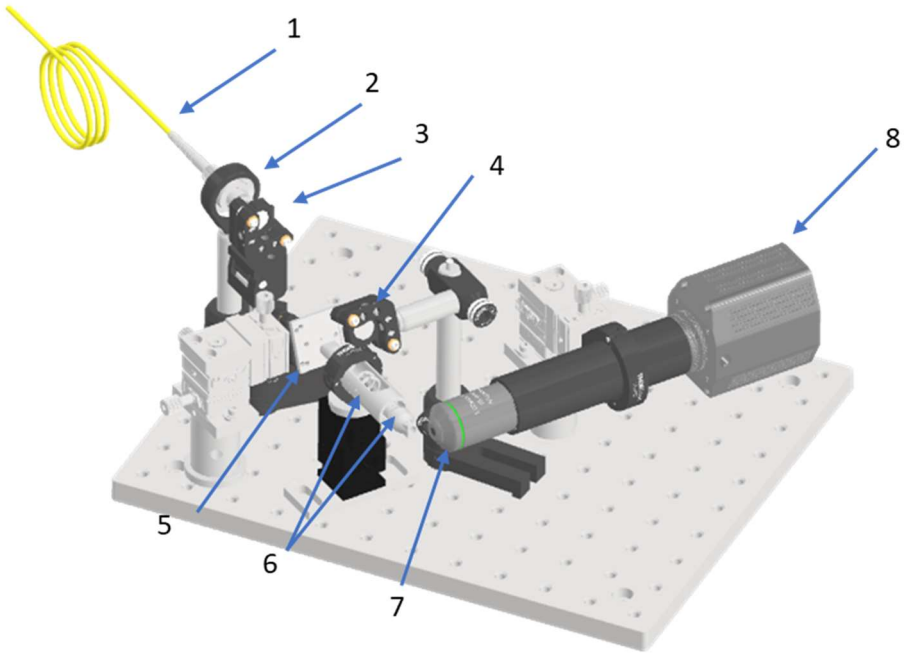

Figure 65. 3D schematic of the microscope : 1 – excitation optical fibre, 2 – collimator, 3 - curvature correction lens, 4 – folding mirror, 5 – thermal MEMS position, 6 – telecentric illumination path, illumination ETL and focusing lens, 7 – imaging objective, 8 – camera.

The 3D printed holder designs are used specifically for the housing of the thermal MEMS and the telecentric lens setup including the excitation side electrical tunable lens. The housing of the MEMS and the first lens of the telecentric setup follow an approach similar to the one introduced in 4.2.3. The telecentric path is housed within a half-inch diameter tube lens (Thorlabs SM05L20C). Housing of both the tunable lens and focusing lens is done with a two-part 3D printed adapter design as it is shown in Figure 66. The first part of the design features a front slot for the 5 mm diameter lens with a secure push-fit. The push-fit feature is also used for the tunable lens slot design with a cutaway arch being used both for fitting the lens and allowing exit for the ETL actuation cable. At the end of the part, four holes are positioned along the perimeter with a 2 mm threading. The second part equally features an identical 4 thread design with a slightly smaller perimeter to ensure a secure fit inside the first part. The 12.7 mm diameter base at the end of the second part ensures that the holder can fit tightly within the lens tube with a retainer ring being able to accurately position the holder in the correct position. The 2 mm screws used for fixing the two parts together allow for

precise alignment of the holder with the remaining components that are located within the lens tube system providing a secure and rigid fit. The designs are fabricated with the Formlabs Form 3 3D printer following the methodology introduced in chapter 3.4.2.

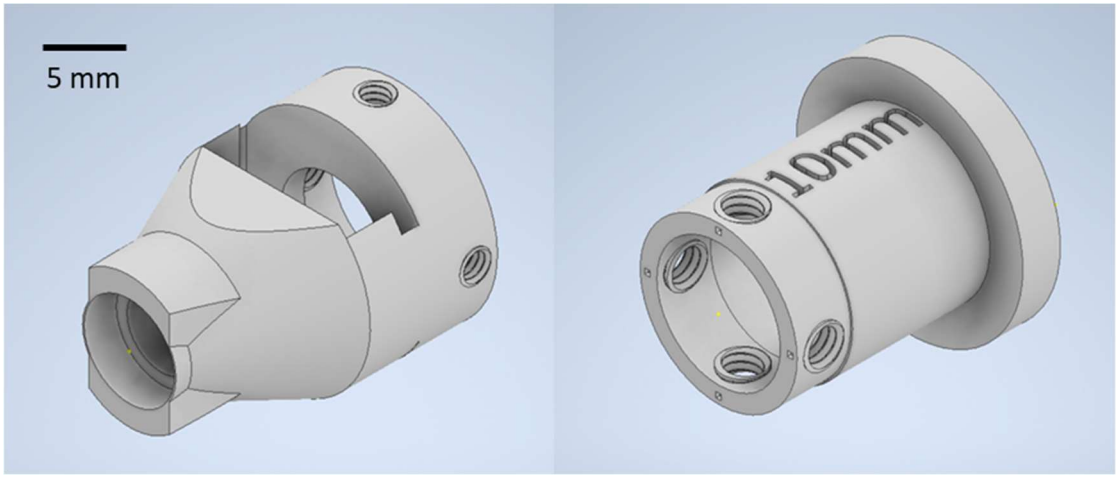

Figure 66. Design concept to combine the focusing lens and illumination ETL at the end of the illumination path.

5.2.4 Imaging Path Characterization

The performance of the optical elements used in the path are analysed as an assembly with a focus on the achievable resolution, FOV and refocusing capabilities using the electrical tunable lens.

The calculation of the pixel to μm ratio of the system is done with the use of 15 μm fluorescence bead target (ThermoFisher FocalCheck™ Fluorescence Microscope Test Slide #1). The microscope slide containing the ring-stained beads is positioned in the 30° / 60° angled configuration introduced previously. The optical prism introduced in chapter 2.4 is coupled onto the slide as described previously using immersion oil (Sigma Aldrich I0890). The intensity graph of the beads is acquired in Fiji using a single line intensity profile along the centre of the microbeads as it is shown in Figure 67**Error! Reference source not found.**. The FWHM mean pixel value is 41.6 which results in a pixel to micrometre ratio of 0.36.

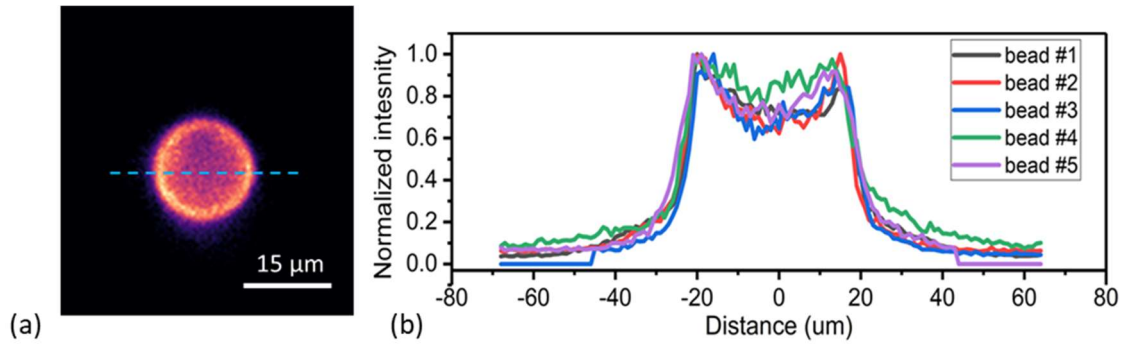

Figure 67. (a) 15µm bead example that was used to plot the (b) profiles that define the pixel to µm ratio with the ETL and sCMOS camera system. The FWHM mean value is 41.6 pixels.

The resolution of the system can be measured following the line spread function approach as it was introduced in the previous chapter. This is performed on the USAF 1951 target microscope slide. The slide is positioned in the imaging area facing the imaging path. A single LED illumination source is positioned at the back of the slide. Figure 68 (a) shows the ROI chosen for evaluating the lateral resolution. The black square chosen for the test has specified dimensions equal to 39.05 x 39.05 µm. The ESF of the system is derived and presented in Figure 68 (b). The resulting LSF is also presented in Figure 68 (c). The FWHM of the system is measured at 1.15 µm. The achievable FOV is measured at 697 µm x 438 µm.

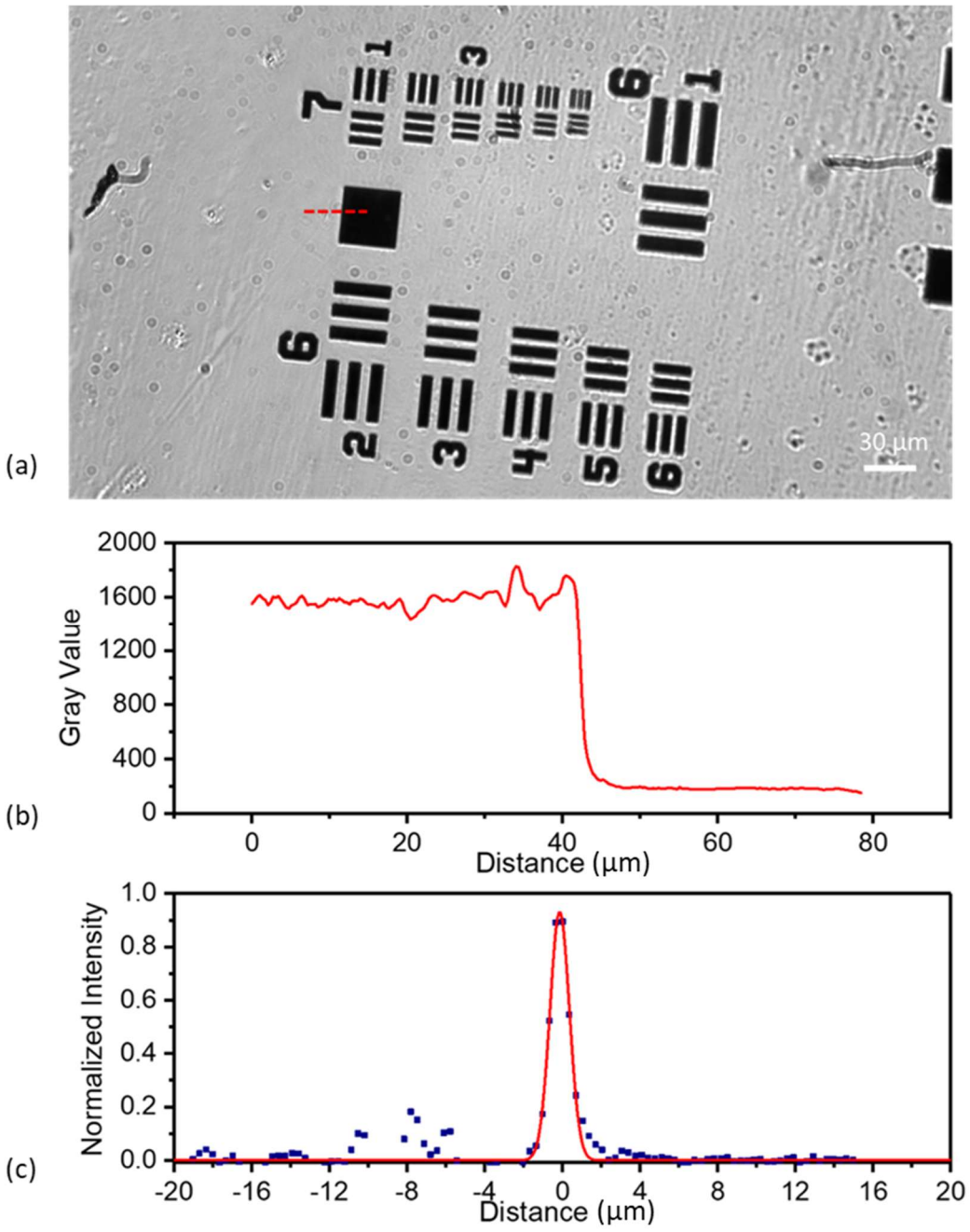

Figure 68. (a) USAF target measurements for the imaging resolution. Highlighted is the location of the edge test. (b) ESF and (c) LSF of the imaging path. The measured FWHM of the LSF is 1.15 µm.

Finally, the focal change capabilities of the system are characterized in the same configuration. Figure 69 illustrates the change in focal length achieved. The tunable lens has a linear response between the change in curvature and the achievable focal plane displacement and when used within the imaging path system it can achieve over 200 µm in focal plane change with a current input of 50 mA. It is important to note

that unlike the EL-3-10 the EL-10-30 only changes curvature in one direction. This explains the chosen range from 0 mA to 50 mA as it keeps the lens closest to its flattest shape in order to minimize spherical aberrations.

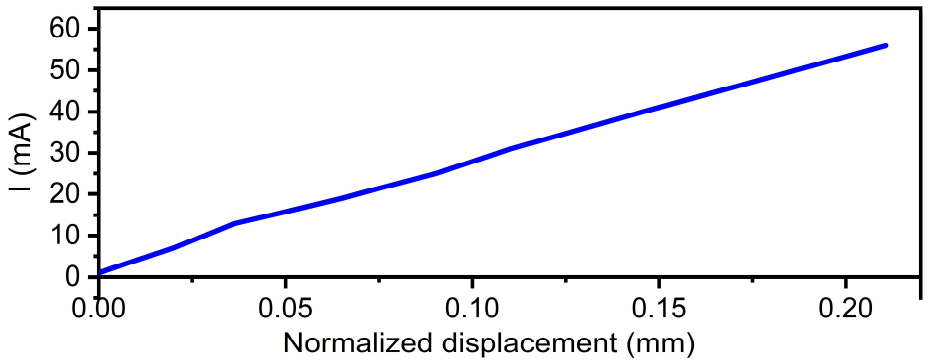

Figure 69. Characterization of EL-10-30 tunable lens for a total focal dislpacement of 0.22 mm.

5.2.5 Illumination Path Characterization

The characterization of the illumination path is done with a series of tests that provide information regarding the beam characteristics within the imaging area and the performance of the active elements as parts of the system. The characterisation follows the same concept introduced in chapter 4.2.4. A transparent cuvette is positioned in the sample area of the miniaturized LSFM system. The cuvette contains fluorescein salt diluted in de-ionized water. The propagation of the beam throughout the cuvette is observed horizontally with the recorded image being presented in Figure 70 (a).

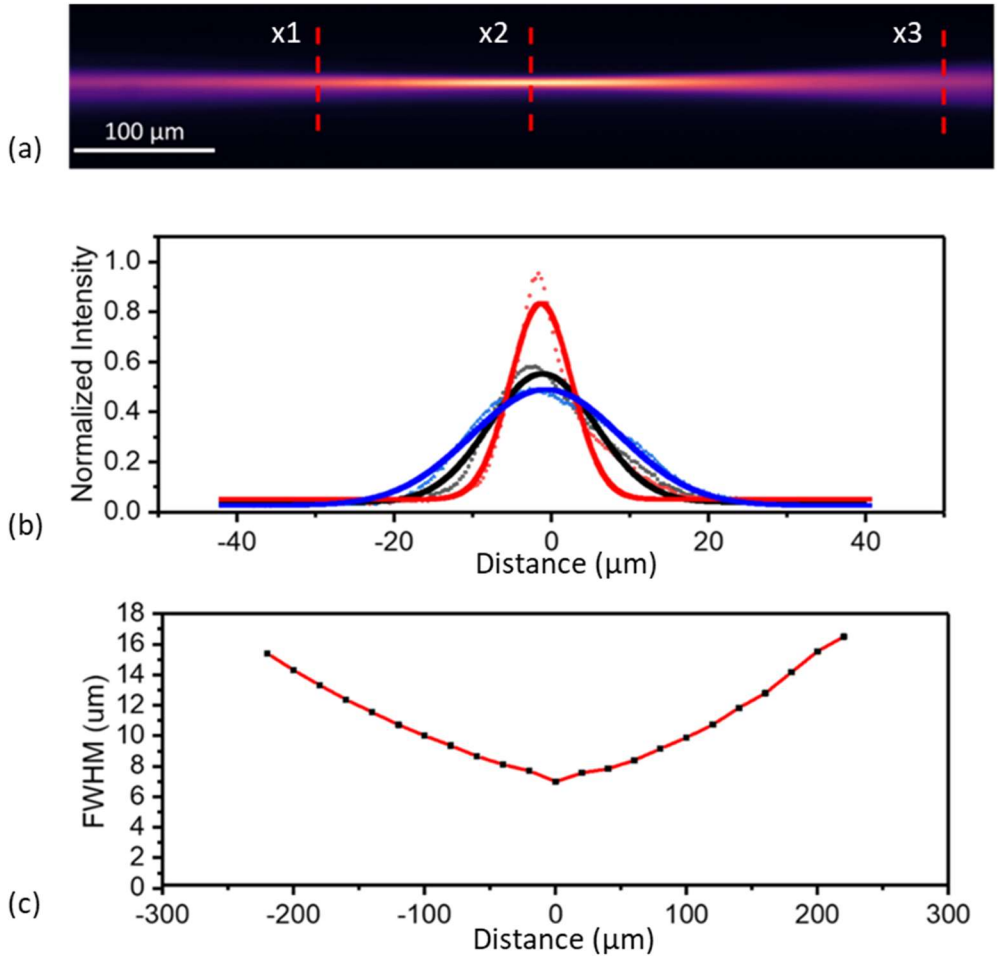

Figure 70 (a) Illumination beam propagation through fluorescein cuvette. (b) Three intensity profile datasets along the focus x= 0µm of the beam and in locations x1= -150 µm and x2 =0 µm and x3 = 300 µm. (c) Beam waist of illumation path with a measured focus FWHM of 7.1µm and a confocal parameter of b=210 µm .

The FWHM of the beam can be measured at the centre of the beam waist to evaluate the minimum achievable light-sheet thickness. This can be done by plotting the intensity profile of a single line crossing vertically the centre of the beam waist with the result of this being presented in Figure 70 (b). The beam waist FWHM is 7.1 µm. Two more example intensity profiles are presented at locations x= -150 µm and x= 300 µm near the edge of the FOV.

The confocal parameter is experimentally measured as the distance between the locations where the FWHM off the beam is √2 times the FWHM at the beam waist. For the beam waist seen in Figure 70 (c) this equates to 210 µm. The FWHM of the

beam at those locations increases to 10.1 μm. Equally the maximum attainable light-sheet height is measured at 412 μm and is achieved with a 6 V amplitude and frequency of 2202 Hz input to both vertical actuators of the thermal. This is in accordance with the limitation of the resonant axis angle introduced in chapter 3.2.2 and it is slightly shorter than the imaging optics FOV height by 38 μm.

With the inclusion of the EL-3-10 to the system, the focus of the illumination beam can actively change with a change to the lens curvature as is shown experimentally in Figure 72. The focal point can change from -xmax to +xmax of the 697 μm FOV with a change from -135 mV to 135 mV. Additionally, a series of 9 steps can be seen as the focal point is scanned axially in the x direction with steps equal to 75 μm. As it has been introduced in chapter 3.3.1 the El-3-10 has a linear curvature change response as the input voltage changes linearly.

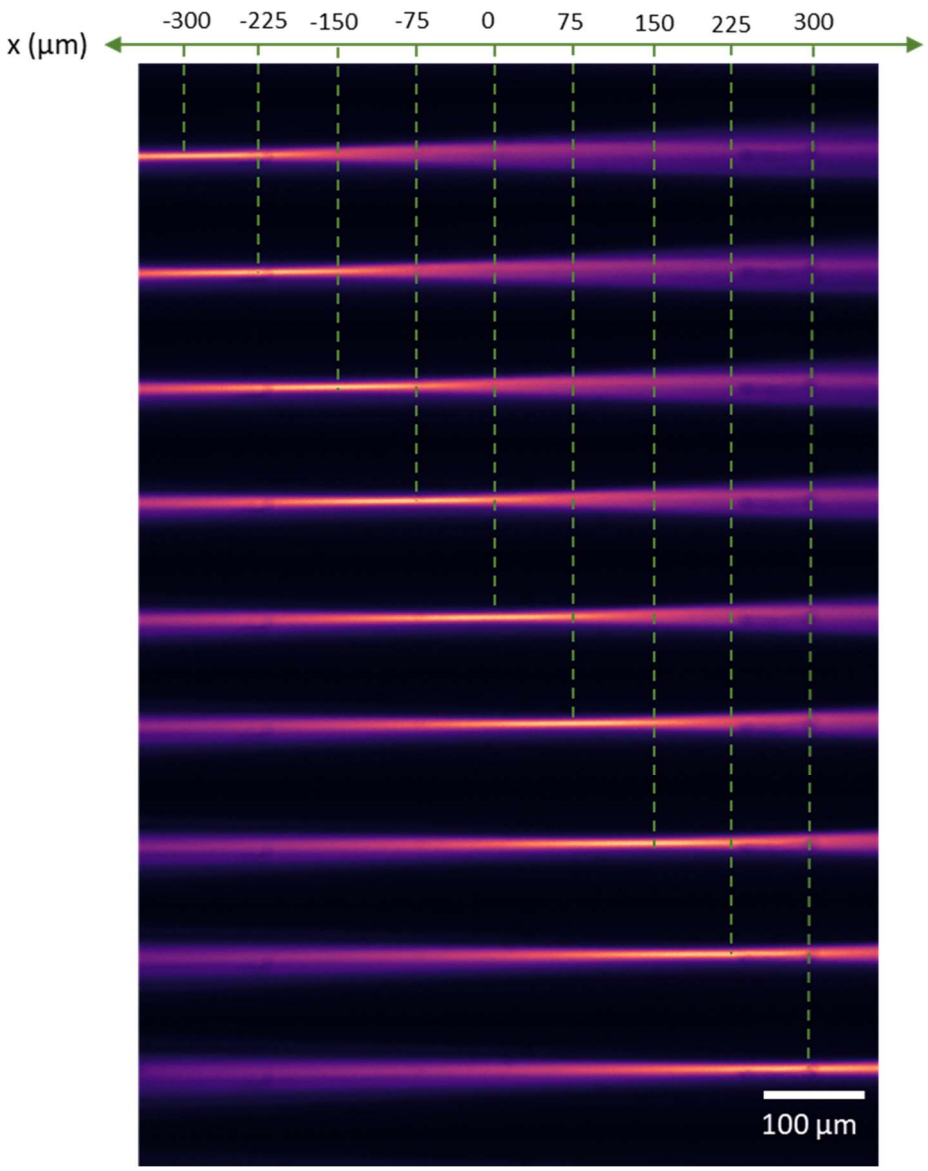

Figure 71. Illumination beam focal point change with tunable lens in 9 steps of x=75 µm.

5.3 Imaging and Results

5.3.1 Imaging Methodology for a Uniform Light-sheet

Light-sheet axial translation and imaging iteration

The fundamental feature of this microscopy setup is to enable light-sheet axial translation that will allow homogenous sectioning throughout the FOV whilst simultaneously managing to increase image quality through increased contrast. For

this reason, the imaging methodology is designed around this concept. Specifically imaging of a sample will take place in multiple cycles where the light-sheet focus changes positions. Making use of the electrothermal MEMS and the imaging ETL, a 3D stack will be collected with steps that satisfy the Nyquist criterion in a similar fashion to 4.3. This translates to a step movement of the electrothermal MEMS of 1.3 μm along the z axis while the synchronized change of focus of the imaging ETL will enable in-focus imaging of the newly illuminated z plane for a total z distance of 263.3 μm. The next cycle of imaging will begin with the illumination ETL setting the focus of the light-sheet to a predefined x position. The same process will then be repeated with the synchronizations of the electrothermal MEMS and imaging ETL recording the stack for the 3D volume.

The number of iterations of the cycle depends on the different scenarios available as the light-sheet is axially translated. Three different scenarios are chosen to demonstrate this feature as presented in Figure 72 in an example schematic. The first scenario shown in Figure 72 (a) showcases the FOV with a single light-sheet position, leading to capturing a 3D volume in the scenario where the illumination ETL will remain unactuated and the light-sheet is focused at the centre of the FOV. Figure 72(b) covers the scenario of two cycles of 3D volume imaging. In this case the first cycle of imaging will begin with the illumination ETL focusing the light-sheet at x1 = -160 μm for a -50 mV imaging ETL input. After the initial volume is imaged, the illumination ETL will focus at the second position of x= +160 μm for a 50 mV input and the process will be repeated for the second 3D volume stack. The two stacks are cropped appropriately along the centre of the FOV and combined as one image using Fiji. This will lead to a stack where the light-sheet thickness is artificially decreased comparing to the stack of Figure 72(a). Similarly, Figure 72 (c) showcases the scenario where the 3 different cropped stacks are combined to represent the 3D volume. The different stacks are a result of the three different positions of the light-sheet focus. The illumination ETL inputs of -68 mV, 0 mV and 68 mV will axially transfer the focus of the light-sheet to x positions of -225 μm, 0 μm and +225 μm respectively. The FOV is divided in three equal parts of 232 μm length. Once the stacks are cropped according to the dimensions, they will be combined to feature the complete 3D volume using Fiji. The new stack will feature again a thinner light-sheet as a result of the stitching process.

To provide a clearer understanding of the benefits of this process to the light-sheet width it is important to quantify the thickness reductions. The scenario of Figure 72(a) without any stitching will feature a light-sheet width ranging from the minimum measured thickness of 7.1mm, to a thickness of 24 μm along the edges of the FOV. The second scenario of Figure 72(b) will feature a light-sheet increase up to 13 μm in the combined stack after the stitching process. This will result in a 45% decrease of the maximum thickness.

Equally in the scenario of Figure 72 (c) each one of the cropped stacks will feature a maximum light-sheet thickness of 10.5 μm that will respectively be the maximum thickness of the light-sheet after combination and production of the final stack. This will result to a 56% reduction when compare to the maximum thickness of scenario Figure 72(a) and a 10% reduction to the already reduced thickness outcome of scenario Figure 72 (b).

It is also important to compare the total time and size of stacks as factors of the three different scenarios to fully evaluate the effects of each. As the process is done on a series basis the total processing time of scenario Figure 72 (b) and Figure 72 (c) will be over 2 times and 3 times respectively when compared to the single stack captured in scenario Figure 72 (a). The same applies to the data file size of the stacks during capturing. Although it is important to note that the final result after tiling will be of equal size for all three figures. It is also important to note that the process of axial scanning can be implemented with other methods that take advantage of the rolling shutter of sCMOS cameras [55], [57], [112]. This methodology can significantly reduce the time restrictions and implement a more efficient imaging strategy but with the disadvantage of such cameras costing one order of magnitude more than the camera that is used in this project.

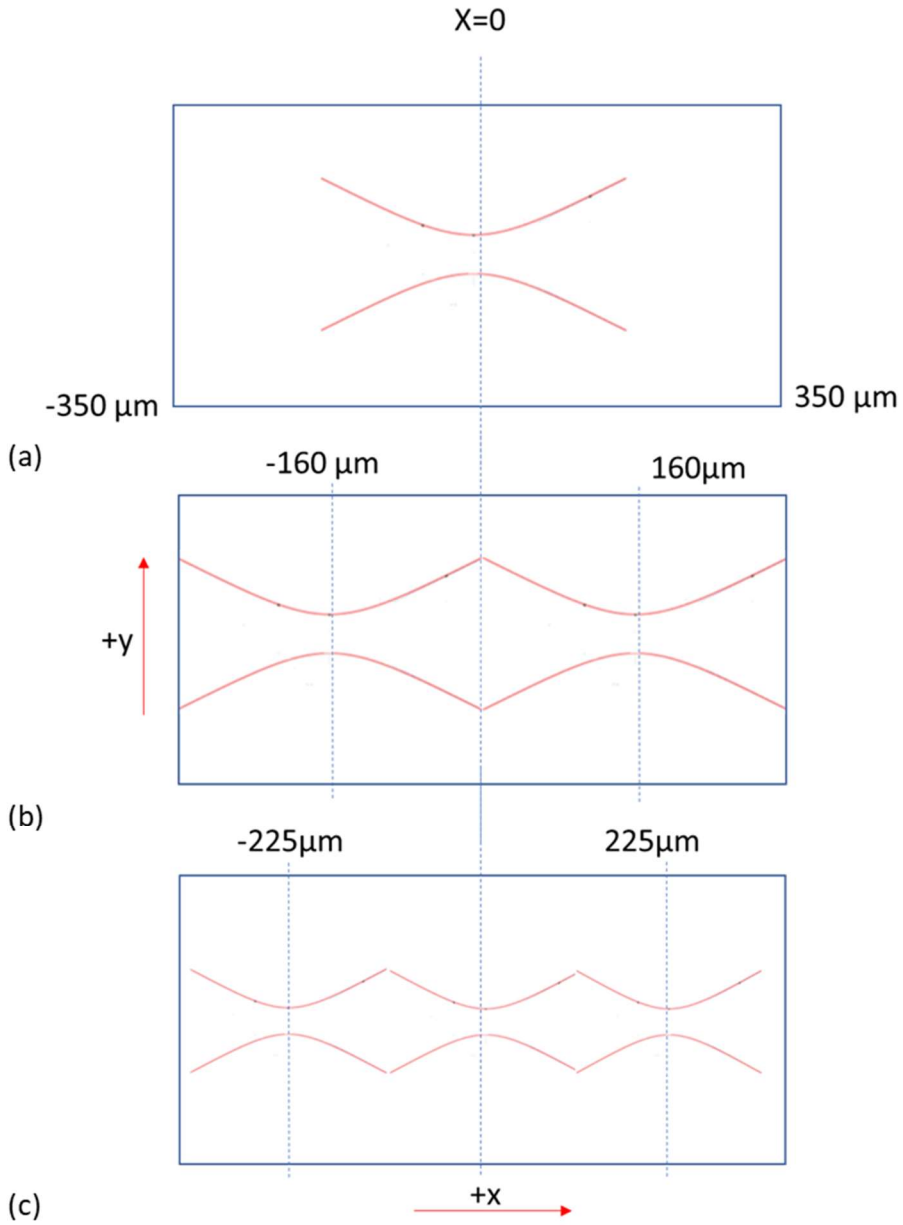

Figure 72. Exemplary top view schematic of lighseet propagation in volume for the three different scenarios imaging stack with (a) a single light-sheet focus position at 0 µm without actuation of the illumination ETL. (b) two light-sheet focus positions at -160 µm and 160 µm with a ETL actuation of -50 mV and 50 mV respectively (c) three light-sheet focus positions at -225 µm, 0 µm and 225 µm with a ETL actuation of -68 mV , 0 mV and 68 mV respectively.

5.3.2 LabVIEW Control

The illumination active elements used in the microscopy setup control is schematically illustrated in Figure 73. A Teensy 3.6 microcontroller is used for synchronising most of the hardware instead of the Arduino from the previous chapter. Specifically, it is responsible for the input of the electrothermal MEMS for both the static and resonant rotation, as well as, the input of the ETL-3-10. It is important to note that the control of the EL-10-30 is implemented separately with the manufacturer provided Optotune Lens driver 4 - OEM version. The Teensy board is able to generate a square-wave pulse-train that will be amplified to enable driving of the MEMS resonant actuators within the specified range. The static MEMS angles are controlled through a dedicated DAC chip with its output amplified and fed through the actuators on either side of the MEMS in order to enable both a positive and negative angle change. The EL-3-10 is driven through a second amplifier that will allow the device to operate within the specified range. Connections between the driving unit and the active elements are implemented with standard jumper wires.

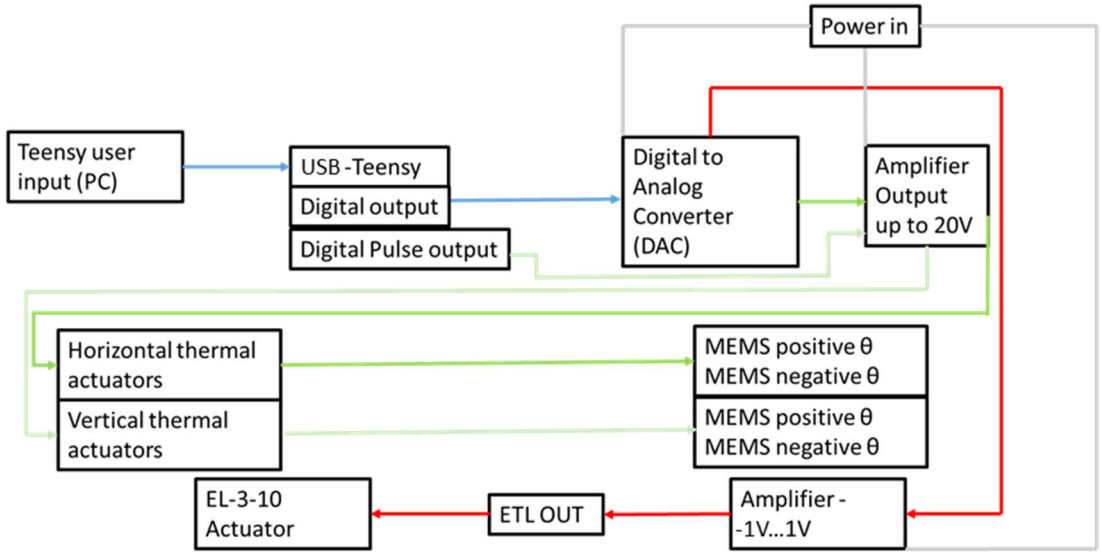

Figure 73. High-level schematic of active element control using a Teensy 3.6 board. (This is co-designed, and implemented by Dr. Ralf Bauer.)

The synchronization of the described electrical actuation processes is implemented using LabVIEW 2020. The objective of the synchronization is to relate each newly illuminated plane with the required change of focus. Specifically, the incremental angle change of the static axis of the MEMS will be combined by the incremental change of tunable lens curvature. Additionally, the generation of the light-sheet is also actively synchronized. This aims to reduce the effects described in chapter 3.2.2 where the resonant line decreases with the increase of the static line. As a result, the resonant actuators will receive a different frequency pulse input during the variation of the static angle.

The overview schematic for the developed LabVIEW design is illustrated in Figure 74. The purpose of this section is to introduce a more accurate and versatile method for addressing the non-linear response between two elements, building upon the approach discussed in section 4.3.1. In contrast to the focus score algorithm previously introduced, this method requires the user to input a series of calibration values for three critical variables: MEMS (static angle), Lens (lens actuation), and Freq (frequency of resonant angle), as illustrated in Figure 75. This calibration process is necessary because, unlike the tunable lens, the electrothermal MEMS used in the system exhibits a non-linear response when actuated. The actuation of the MEMS slow axis is detailed in section 3.2.2. Similarly, the MEMS resonant angle demonstrates non-linearity when both scan line and static rotation are simultaneously engaged.

To address these non-linearities, a spline fit is employed to generate a lookup table, correlating the fitted values to specific sample space values. This process results in each sample space value being matched with the system's three variables. The sample space changes linearly, which is expected to more effectively address the MEMS non-linearity. It is crucial to note that the reliability of this process depends on the accuracy of the calibration data. As experimental conditions change, recalibration may be necessary to ensure consistent operation. This dependency on accurate calibration was identified as a limitation in the data presented in this chapter. An additional correction method, exploring how linearity in the z axis can be addressed using Fiji tools, is presented at a later point in section 5.3.5.

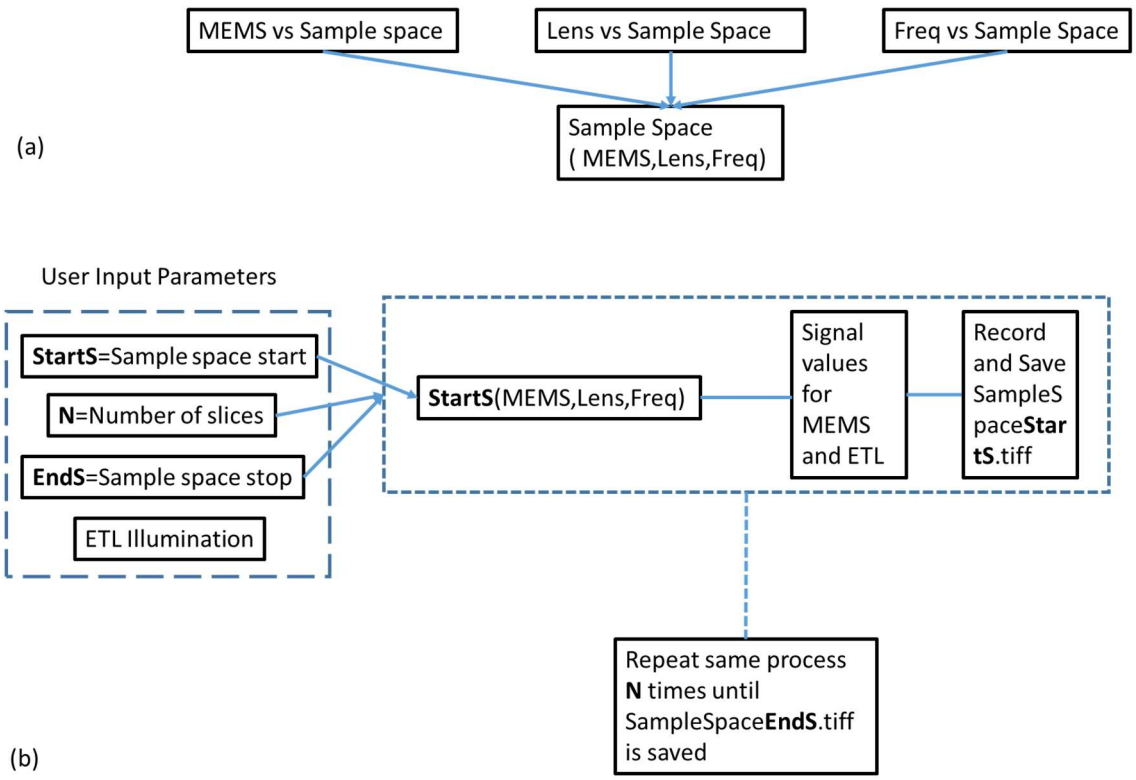

Figure 74 High-level schematic of LabVIEW. (This is co-designed, and implemented by Dr. Ralf Bauer) a) Block diagram of the sample space LabVIEW initialization. b) Block diagram of the image acquisition methodology in LabVIEW.

The second part of the developed LabVIEW design includes all the necessary processes for the user to collect an image volume through automated image acquisition based on the sample space synchronization linear fit calibration as seen in Figure 75. Specifically, the user defines a start and stop value assigned to the sample space along with a number of slices required for the stack. The ETL illumination value is also entered that will set the position of the light-sheet axially. The software will enter a loop for the defined amount of iterations where the signals for the three values will be synchronized and the recorded image will be saved accordingly. This will create the 3D stacks of the desired number of slices between the specified range.

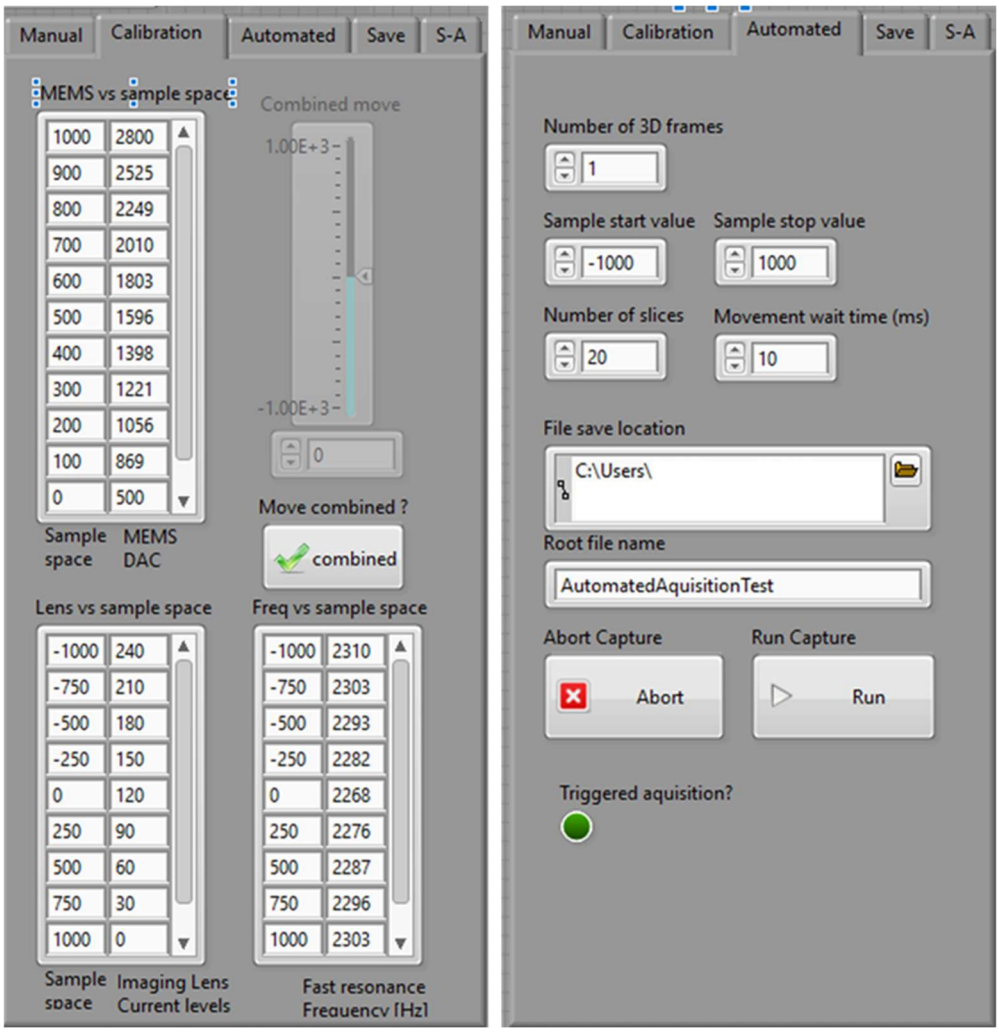

Figure 75. LabVIEW control.

It is important to note that further action has been deemed necessary in understanding and correcting the response of the MEMS mirror in the imaging experiments. As a result, a semi-automated method was introduced with the option to collect a set of varying focus images for each step of the MEMS. This approach collects a range of 10 images for each light-sheet position, varying the imaging path ETL by 4.2 µm steps around the nominal focal position. This allows a post-imaging evaluation if any anomalies in the synchronised positioning between the imaging and excitation path have occurred. The stacks presented in this chapter are a combination both the automated and semi-automated method in an effort to always present in focus images of each stack. Further expansion on the correction of the imaging ETL and MEMS calibration is provided in following sections where the imaging results are presented. The z steps provided for the imaging stacks is the average step calculated from the

total range in z needed to cover the specified volume and divided by the number of slices that form the stack.

Stitching

In the scenarios where the light-sheet is axially translated along the beam propagation axis, further processing steps are required after acquisition of the stacks. For the scenario with two light-sheet positions, using the specify and crop tool of Fiji, the two acquired stacks are cropped into two halves along the x-axis, keeping the sides that include the light-sheet focus in each occasion. The stacks are recombined resulting in a single stack with two light-sheet focus points along the width. In a similar fashion the stack of 3 light-sheet positions is cropped in 3 equal parts. The parts are combined again to form the resulting stack with 3 light-sheet focus points occurring along x.

5.3.3 Optical Sectioning Performance Evaluation on Ring-stained Targets

An evaluation of the axially translated light-sheet can be made with imaging of the 15 μm ring-stained bead sample. The slide is positioned in the imaging area with an attached 3D-printed prism in an angled configuration as introduced previously. A section of the FOV positioned at x = +110 μm away from the centre is chosen for the analysis. The imaging experiment focuses on the improvements in sectioning performance that are observed with the axially stitched light-sheet compared to a static light-sheet used for the same set of beads.

To evaluate the effect of the axially translated light-sheet on imaging performance, it is crucial to consider the dynamics that occur when ring-stained fluorescent beads are illuminated. The key characteristic of these beads is their hollow structure, resulting in fluorescence emission only from their surface. As the light-sheet optically sections the bead, its thickness serves as a metric for its sectioning ability. This can be quantified by two values derived from the intensity profile plot of each bead: the maximum intensity detected at the surface and the minimum intensity at the central area of the bead. Initially, we consider the scenario of a bead being sectioned at the light-sheet focus. Here, the intensity is expected to be higher as a Gaussian light-sheet exhibits its

peak intensity at its beam waist. Concurrently, the Gaussian light-sheet has its minimum thickness at the beam waist, and if this part of the beam sections the beads, the intensity in the centre should drop to lower values, ideally approaching zero. It is important to note that for the latter to occur, the bead diameter should be significantly larger than the full width at half maximum of the light-sheet at its beam waist. When optically sectioning the beads with parts of the light-sheet away from its waist, two effects are observed. First, the fluorescence intensity from the bead surface decreases due to the lower illumination intensity in the Gaussian profile. Second, the minimum intensity in the bead centre increases. This occurs because the thicker cross-section of the light-sheet illuminates multiple planes in the axial direction, collecting fluorescence information from a larger portion of the bead surface. To quantify these differences, several examples are presented in the following sections. These examples demonstrate how the light-sheet thickness and position relative to the bead affect the intensity profile, providing insights into the system's sectioning ability and overall imaging performance.

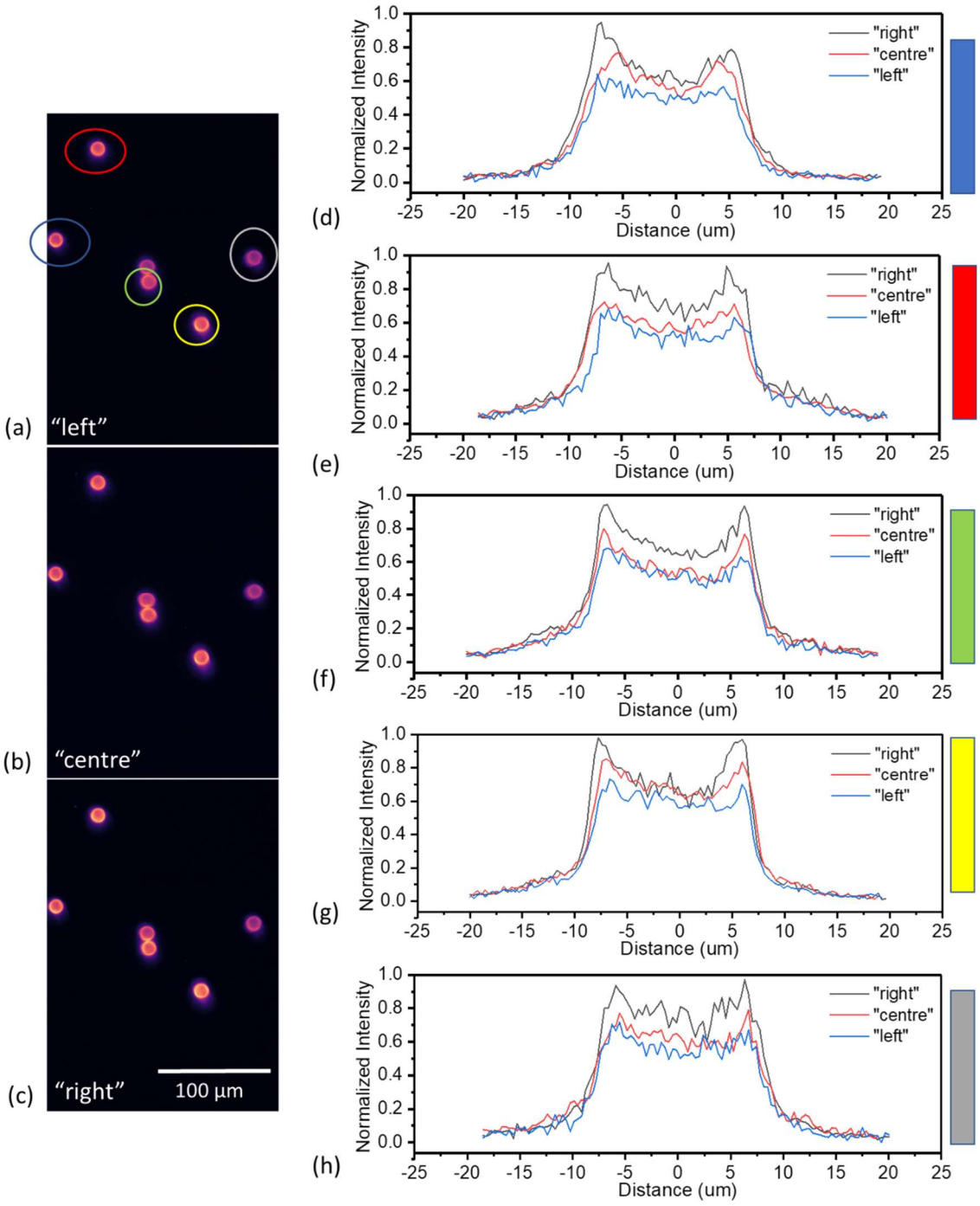

Figure 76. Maximum projection of ROI FOV of 15 µm bead target for three different light-sheet focus positions namely, (a) x = -160 µm (left) (b) x= 0 µm (centre) and (c) x = +160 µm (right). Plot profiles of a set of 5 beads colour coded to identify in the graph((d)blue, (e)red, (f)green, (g)yellow,(h) grey). Each graph contains three datasets of the repsective intensity plot profiles of the same bead for the three different ligh-sheet positions.

As is shown in Figure 76, a set of 5 beads is selected for the analysis. For each of the three maximum projection bead images the light-sheet focus is positioned in a different location along the x axis with the appropriate actuation of the excitation ETL. Specifically, in the "left" image the light-sheet is position at x=-160 μm which is outside of the shown FOV. The same stands for the "centre" where the light-sheet focus is positioned closer to the set of beads but still outside the FOV at x=0 μm. For image "right" the focus of the light-sheet is inside the FOV at x=+160 μm and is located between the "red" and "green" bead of the set. Each one of the beads is individually analysed in terms of their intensity profile along the centre of the bead for the three different light-sheet locations and the results are presented in the profile plots of Figure 76 (d)-(h). The results of all 5 comparison plots have been normalized according to the maximum intensity value between the three measurements.

The effect of the location change for the light-sheet focus is evident in all 5 plots with the "right" positioned light-sheet being the one that produces the beads with the higher overall intensity in each case. The peak intensity in each series of the 5 graphs occurs in the outer ring part of the beads due to its staining. Comparing the peaks for all 5 graphs, there is a bigger difference in the range of 20% to 30% between the "right" and "centre" light-sheet that is also presented in the maximum intensity projections as the difference in brightness between the respective two images. The "left" image shows the lowest peak brightness whereas the difference between "left" and centre is smaller between 5% and 10% throughout the test. This is expected as, compared to the "right" light-sheet, both the "left" and "centre" focus outside of the selected FOV area, leading to significant less signal.

In terms of sectioning, it is again evident that the position of the light-sheet focus is affecting the results as expected. The nature of the ring-stained beads allows for a more accurate interpretation of this, as the 15 μm beads are only emitting fluorescence from the outer surface. It is important to note that the thickness of the light-sheet is not small enough, compared to the diameter of the beads, to allow the intensity of the plot to drop close to zero values when the beam is sectioning its volume. Nonetheless the improved sectioning ability due to the axial translation can be observed to the "right" light-sheet in all the 5 measure beads where the centre-to-surface intensity difference varies from 30% to 40%. The same measurement for the remaining two positions will

provide substantially different results with the intensity difference along the centre of the beads reaching up to 25 % for the “centre” light-sheet and only up to 15% for the “left” light-sheet.

5.3.4 Fluorescence Imaging Resolution

Investigating the fluorescence imaging resolution requires an analysis of a sub-micron target that will reveal information of the intensity PSF graphs for both the lateral and axial resolution. Starting with the lateral resolution analysis, the Fluoro-Max Dyed Green Aqueous Fluorescent Particles G500 by Thermofisher are used in the 3D printed well structure introduced in Figure 77. The target is implemented following the methodology introduced in 4.3.2. The microscope slide structure will then be positioned in an angled configuration between the illumination and imaging path to enable fluorescent imaging as it has been illustrated in previous chapters. The xy view of the sample can be used to acquire information regarding the lateral resolution of the system. The intensity profile across the centre of the bead will result in the PSF illustrated in Figure 78 (a). The FWHM of this is 1.13 μm.

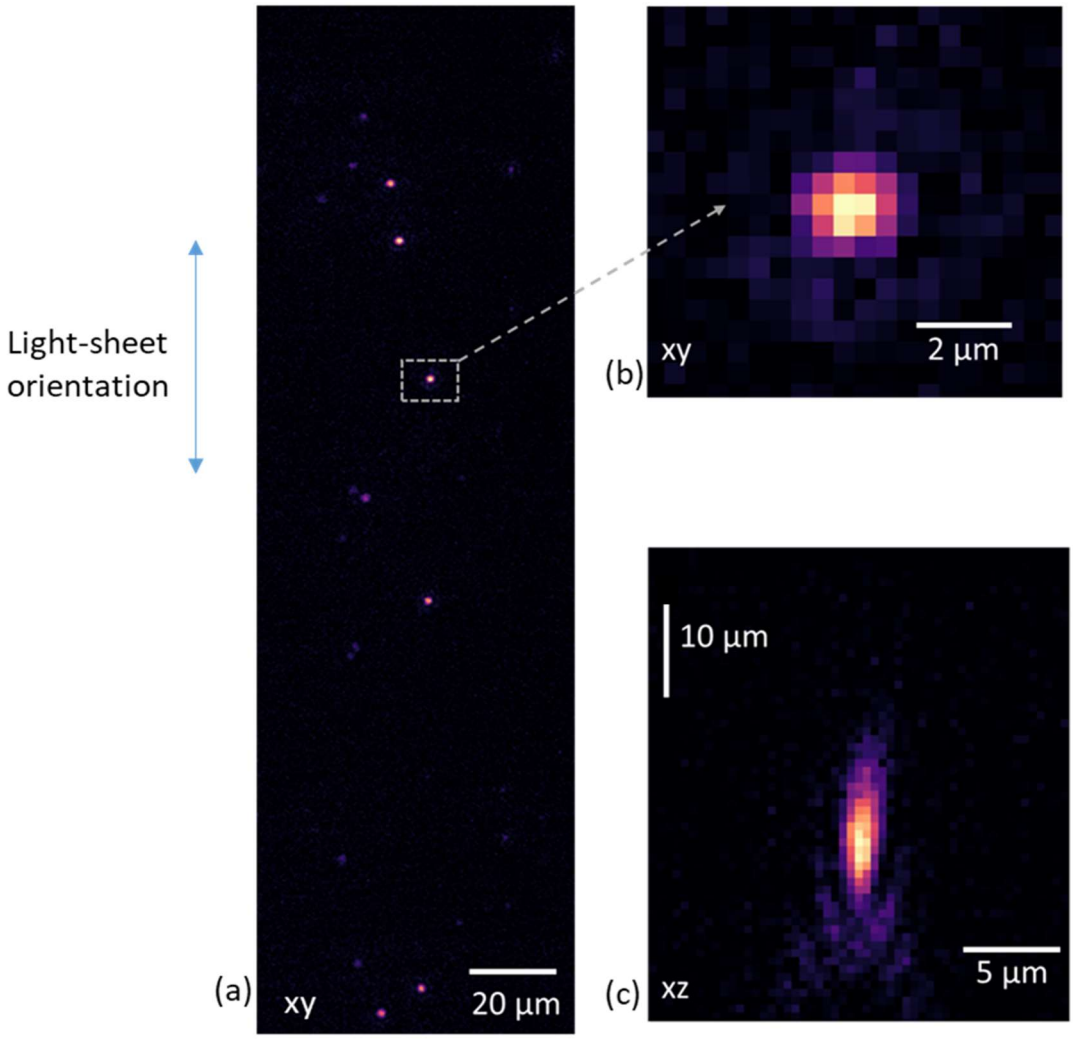

Figure 77. (a) xy slice for ROI of the 0.5µm bead target. (b) xy slice of the sub-micron bead (c) xz slice of same bead, captured with axially shifting the focus of the imaging ETL in 1.05 µm steps.

The axial resolution is assumed to be equal to the thickness of the light-sheet which is also confirmed in the previous characterization in 4.3.2. This is true for systems without high NA objectives. The thickness of the light-sheet in this LSFM system is equal to 7.1 µm.

In order to further evaluate the imaging capabilities of the system, the imaging ETL is used to change the focus of the imaging path while the bead target and light-sheet position remain stationary. The ETL is actuated with steps of 0.25 mA that result in a 1.05 µm step along z, covering an area of z=+15 µm to z=-15 µm with z=0 µm being

the point where the microbeads are in focus. The stack of images is analysed with Fiji. A top re-slice will reveal the xz view as illustrated in Figure 77 (c). The intensity profile of the bead across its centre in the z direction is used for the PSF plot presented in Figure 78 (b). The FWHM of the plot results in 13.5 µm and equals the imaging axial resolution of the imaging arm. This confirms that the axial resolution of the imaging optics is 1.9 times higher than the light-sheet thickness and as a result the minimum axial resolution of the system is defined by the thickness of the light-sheet beam at 7.1 µm.

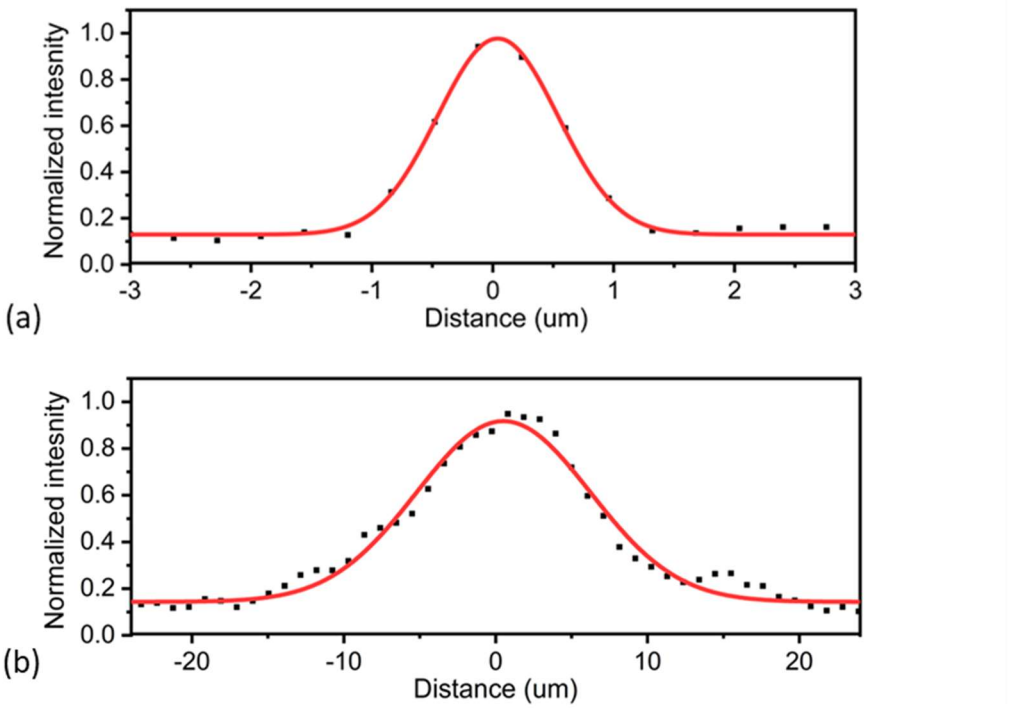

Figure 78. (a) xy intensity profile along the centre of the 0.5 µm bead with a Gaussian fit (red line). The FWHM of 1.13 µm equals the lateral resolution. (b) xz intensity profile along the centre of the xz reslice for the same particle with a Gaussian fit. The FWHM of 13.5 µm equals the axial resolution of the imaging path with stationary light-sheet and refocusing of the tunable lens.

In addition, both the axial and lateral resolution can be used to calculate the effective NA of the imaging optics. According to chapter 2.2.2, a rearrangement of the formula will provide the effective NA of the system with the substitution of the measured lateral resolution.

$$NA = \frac{0.61\ x\ \lambda}{Lateral\ resolution} = \frac{0.61\ x\ 0.51\ \mu m}{1.13\ \mu m} = 0.275$$

Equally the axial resolution formula can be rearranged for the estimation of the effective NA using the Abbe [137] equation below:

$$NA = \sqrt{\frac{2\ \lambda}{Axial\ Resolution}} = \sqrt{\frac{2\ x\ 0.51\ \mu m}{13.5}} = 0.275$$

The effective NA of the system agrees well between both resolution measurements. This is leading to the result that the imaging path numerical aperture is not in practice the same as specified for the imaging objective. This can be attributed to aberrations introduced by the optical quality of the low-cost objective.

5.3.5 Imaging of Cell Slice

Assessment of the imaging capabilities with the axially shifting LSFM is accomplished with the FluoCells™ Prepared Slide #1 by Thermofisher. The Slide contains a thin section of a BPAE cell where the F-actin is stained with Alexa Fluor™ 488 phalloidin. This will result in emission of 520 nm (peak wavelength) light from the F-actin areas when the sample is illuminated with the 488 nm light-sheet. The imaging analysis involves results of the three different scenarios analysed in 4.3.2. In the first example the light-sheet does not get shifted axially through the FOV, following by an example with the light-sheet translated to two symmetric focal position within the FOV and finishing with the FOV including three light-sheet focus positions. Additionally, an alternative approach to chapter 4.3.3 is presented for correcting anomalies in the z-axis spacing for a single stack accessible within Fiji. Finally, the ability to rotate the coordinate systems and access more effectively information for thin samples is also presented. All images presented in this chapter are recorded with the same properties for the camera and illumination settings. Specifically, the camera exposure time is set to 50 ms while the camera is used without binning. The laser power at the sample location is equal to 0.15 mW. The results presented are part of imaging stacks comprising of 201 figures for each z scan with the z step for each scan being equal to 1.3 μm. Each step is a result of the combined actuation of the static MEMS angle and

the imaging ETL. The chosen step size is again based on the observations made in the previous chapter. The step size of 1.3 µm meets the Nyquist sampling criterion in z with a measured light-sheet width of 7.1 µm. The FOV is equal to 697 x 438 µm, as a result of the objective lens magnification and IDS camera used. The height of the FOV presented in the images is limited to 344 µm to ensure a more uniform light-sheet intensity throughout the imaged area. Additionally, the covered z range from the combined movement of the active elements is measured at 261.3 µm. The depth is addressed by using 30% of the ETL range and 80% of the available MEMS range for the static rotation. This results in total imaged volume of 697 x 344 x 261.3 μm^3 (x,y,z).

Similar to the imaging presented in chapter 4.3.3, the angled position of the thin slide sample provides the opportunity to present xy projections of single slices with the thickness information related to the thickness of the illuminating light-sheet. Specifically, Figure 79 illustrates the same slice for the three different stacks, the centre of the FOV is at position (x,z) = (161 µm ,104 µm). According to chapter 5.3.1 this is the position where the light-sheet focal plane is in the scenario of having two light-sheet focal points. As a result, Figure 79 (b) shows the scenario with the thinnest sectioning at this point. The thickness of the sectioning is increased for the two remaining figures, with Figure 79 (a) having the widest section with the light-sheet focused 160 µm away from the centre of the shown FOV. Equally, Figure 79 (c) has the second-best sectioning for this example with the focusing of the light-sheet positioned 65 µm away from the centre of the FOV.

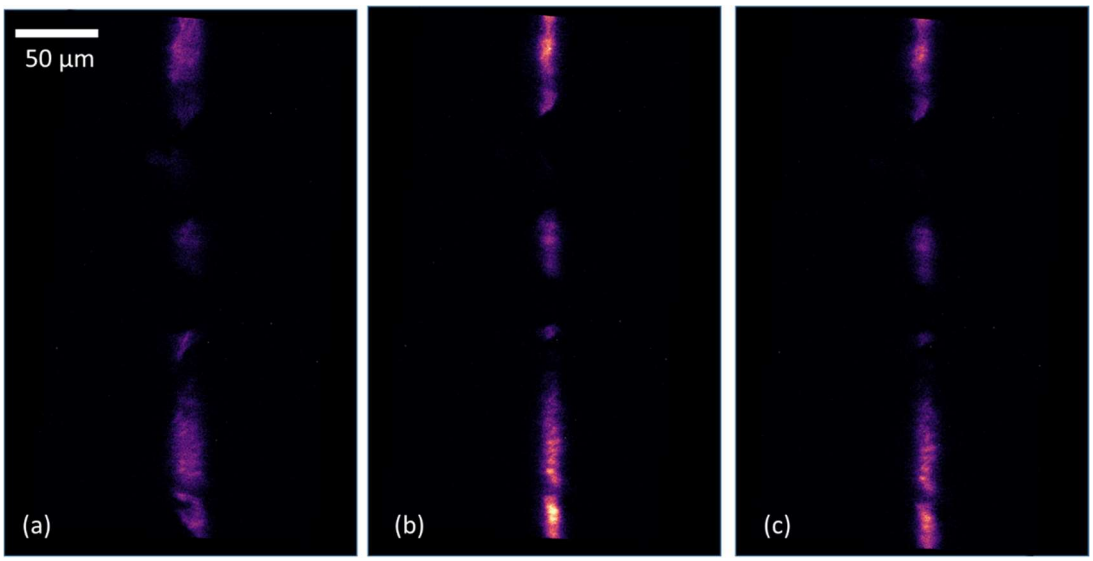

Figure 79. xy slices of the same sample position at (x,z) = (161µm ,104 µm) for three different stacks where the light-sheet focus position is at (a) x=0µm (b) x1= -160 µm and x2 = 160 µm (c) x1= -225 µm, x2= 0 µm and x3 = 225 µm.

A maximum intensity projection for the same stack is presented in Figure 80 and allows observation of the full FOV imaged for the three different scenarios. As is expected in the case of the light-sheet focused at one position (Figure 80 (a)), the intensity and contrast are better along the centre of the maximum intensity projection and the image quality gradually decreases towards the edges. Equally in the scenarios where two (Figure 80 (b)) and three (Figure 80 (c)) focus points of the light-sheet occur within the FOV, the intensity and contrast are higher throughout the whole FOV. Since the maximum thickness of the stitched light-sheet is only 10% larger between the two cases, there is not noticeable differences in the imaging area. On the other hand, a noticeable intensity difference is present when the two reconstructed maximum intensity projections are compared with the maximum intensity projection with no axial shifting of the light-sheet. The estimated decrease in the maximum light-sheet thickness of 45% and 56% can justify this difference. Finally, a striping effect is visible in the two stitched images (Figure 80 (b), (c)) and is also illustrated in Figure 80 (d). The periodic striping observed at the edge of the presented field of view (FOV) is a result of undersampling caused by the non-linear relationship between the light-sheet scan and space. Sampling refers to the number of slices collected within a specified z-range, which ideally should be equally spaced at intervals defined by the Nyquist criterion. The problem arises from the ET MEMS static angle that translates the light-

sheet in z, as explained in section 3.2.2. A method to correct for this non-linear relationship was introduced in section 5.3.1; however, as demonstrated here, it only limits the effect rather than completely addressing it. The characterization curve of the MEMS static angle (Figure 19) showed that equal voltage step increases resulted in unequal angle increases. Specifically, near the 0-angle region (representing the centre of the FOV), the angle increases in smaller increments, whereas for larger angles, the incremental change is more substantial. This static angle response of the MEMS directly relates to the light-sheet scan in z within the system. Consequently, the incremental collection of images at each plane leads to non-linear z-spacing between the collected planes. The planes acquired near the centre of the FOV have denser sampling compared to the sparse sampling that occurs near the edges of the FOV. As a result, the central parts of the projection have a sampling rate satisfying the Nyquist limit, whereas this is not true for the edges of the FOV, leading to "dark" interval stripes between the acquired slices.

The reason this effect is only apparent on one edge of the FOV is attributed to optical aberrations observed on the other edge. It is believed that the effect is present on both edges, but blurriness in the imaging, possibly due to the combination of the objective limitations and tunable lens orientation, obscures this issue on one side.

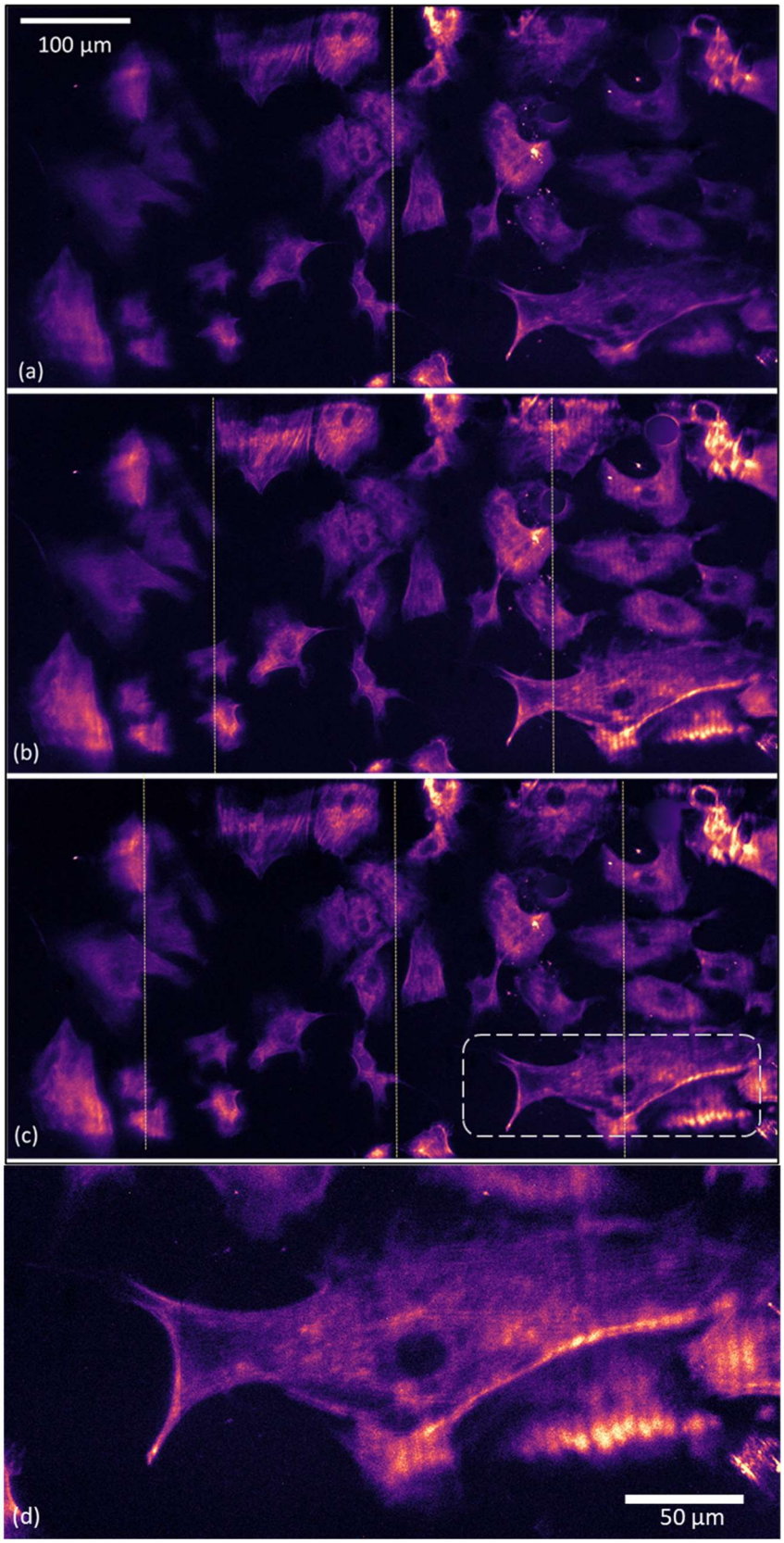

Figure 80. Maximum intensity projection (xy) for BPAE slide with the light-sheet focus at (a) x=0µm (b) x1= -160 µm and x2 = 160 µm (c) x1= -225 µm, x2= 0 µm and

x3 = 225 μm. (Projections shown in this figure have been processed to remove saturated areas in two locations from fluorescent particles, possible located either on the prism or on the cover slip. Original maximum projections are presented in Appendix A). Dashed lines show locations of light-sheet focus. (d) Zoomed in section of the maximum projection shown in the previous image, highlighting the observed striping artefacts.

The xz reslice of the cell sample with spacing 1.3μm is presented in Figure 81 for the light-sheet at rest. The sigmoid response of the intensity over the depth of the imaged volume reveals that further processing is needed in order to correct the non-linearity of the MEMS angle response. The irregularity in this case is more prominent in the central areas where the MEMS is illuminating planes at a slower rate than the outer parts of the FOV. The projected straight line from the first imaged plane to the last imaged plane reveals the measured value of the imaging angle at 20°. Correction of this response is required to investigate both the striping artefacts of Figure 80, as well as, accessing a coordinate transformed image of to the microscope slide in its native coordinate system (x',y ,z').

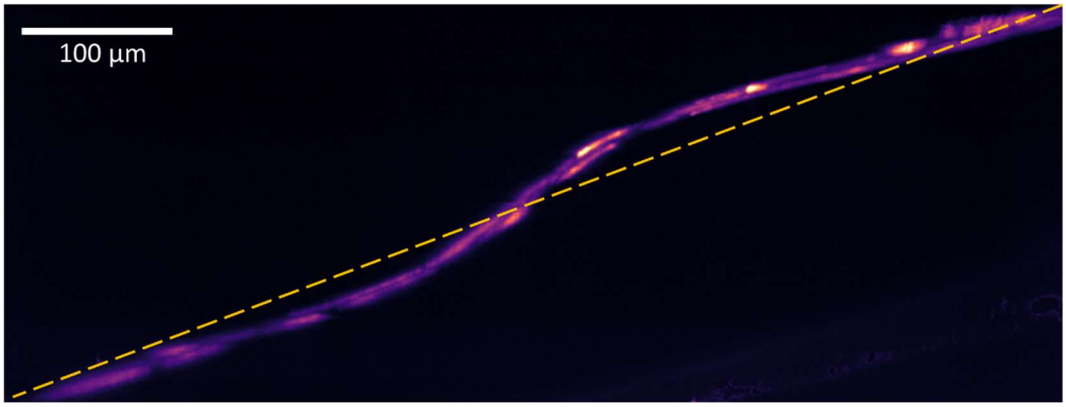

Figure 81. Maximum intensity projection (xz) of BPAE cell sample. Orange dashed line shows an ideal linear response of the MEMS for accessing equally spaced z planes in the sample volume.

For the same purpose a process was introduced in chapter 4.3.3, with the shifting of pixel lines along a straight line being capable of correct the z spacing response. In this chapter an alternative method is presented for correcting this irregularity within Fiji by using the Straighten tool [138]. A segmented line is drawn along the length of the response for the xz stack (see Figure 82(a)), with a linewidth equal to 201 pixels. The straighten tool will correct the curve into a straight line parallel to the x axis (see Figure 82 (b)). Using the Transform j: Rotate Function [139] and rotating the sample by 20°

in the z axis will transfer the response to its correct orientation with a linear response (see Figure 82 (c)). It is important to note that the pixel size needs to be adjusted at this point in order to account for the extended line length that occurred during the straighten transform. Scaling values are based on the fitting accuracy of the resulted straight line. Additionally, the transform j:Rotate fills the rotated area with pixels that need to be cropped before the scaling. For this example, the dimensions of the pixel are assigned at the final step in order to ensure that the x and z axis match the original dimensions.

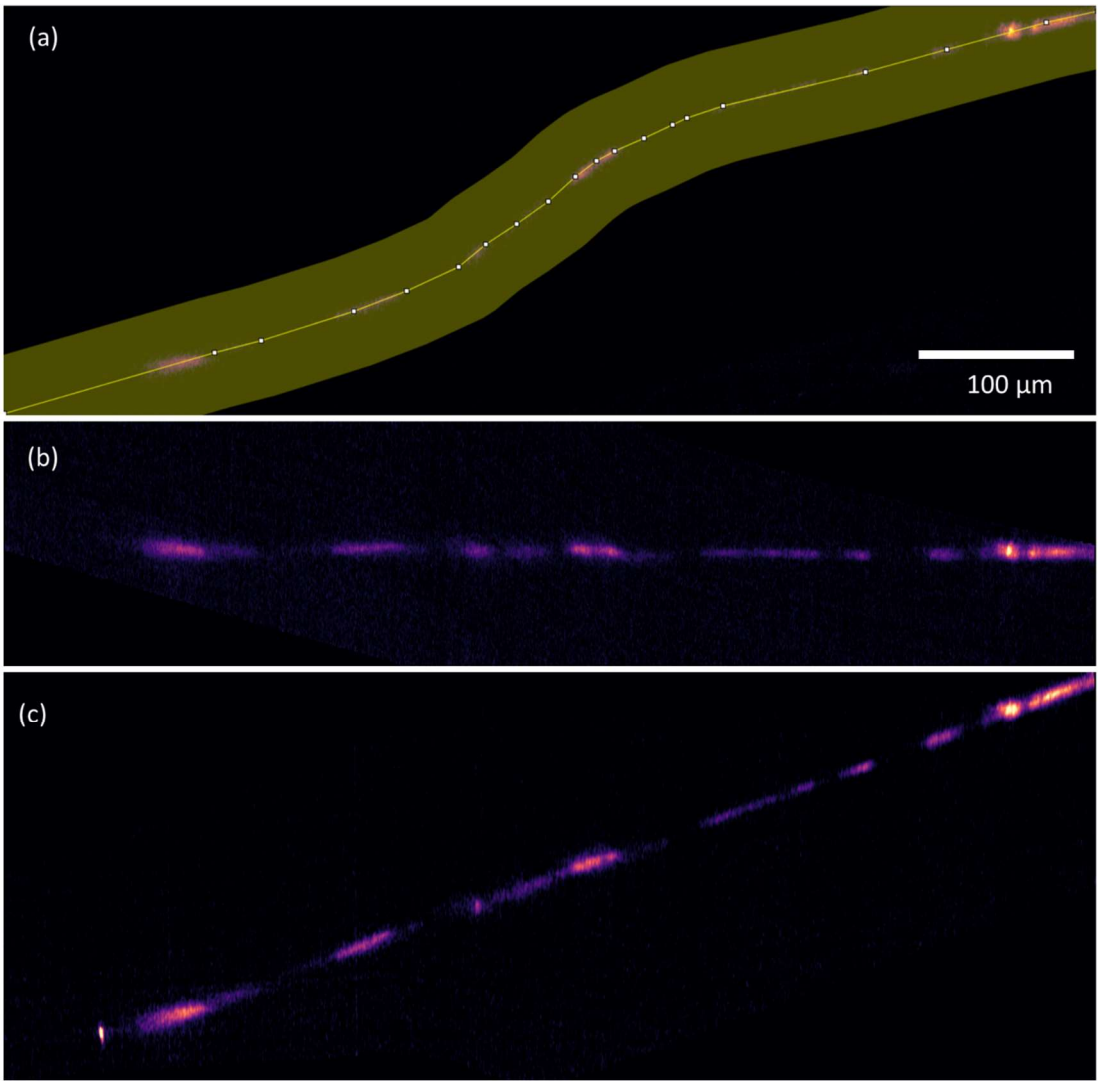

Figure 82. (a) Segmented line fit over xz stack. (b) Result of straight tool (c) Transform to original angle and scale to fit original dimensions.

The same process is repeated for the three different stacks. The xy maximum projections of the stacks after the linear response correction can be seen in Figure 83.

The correction of the response has equalized the z distance of each slice but in the case of the overall image quality striping artefacts seem to be consistent throughout the edge of the FOV. As it was expanded earlier, the underlying reason for their appearance is due to a combination of experimental factors, and the post processing methods applied here cannot correct for it

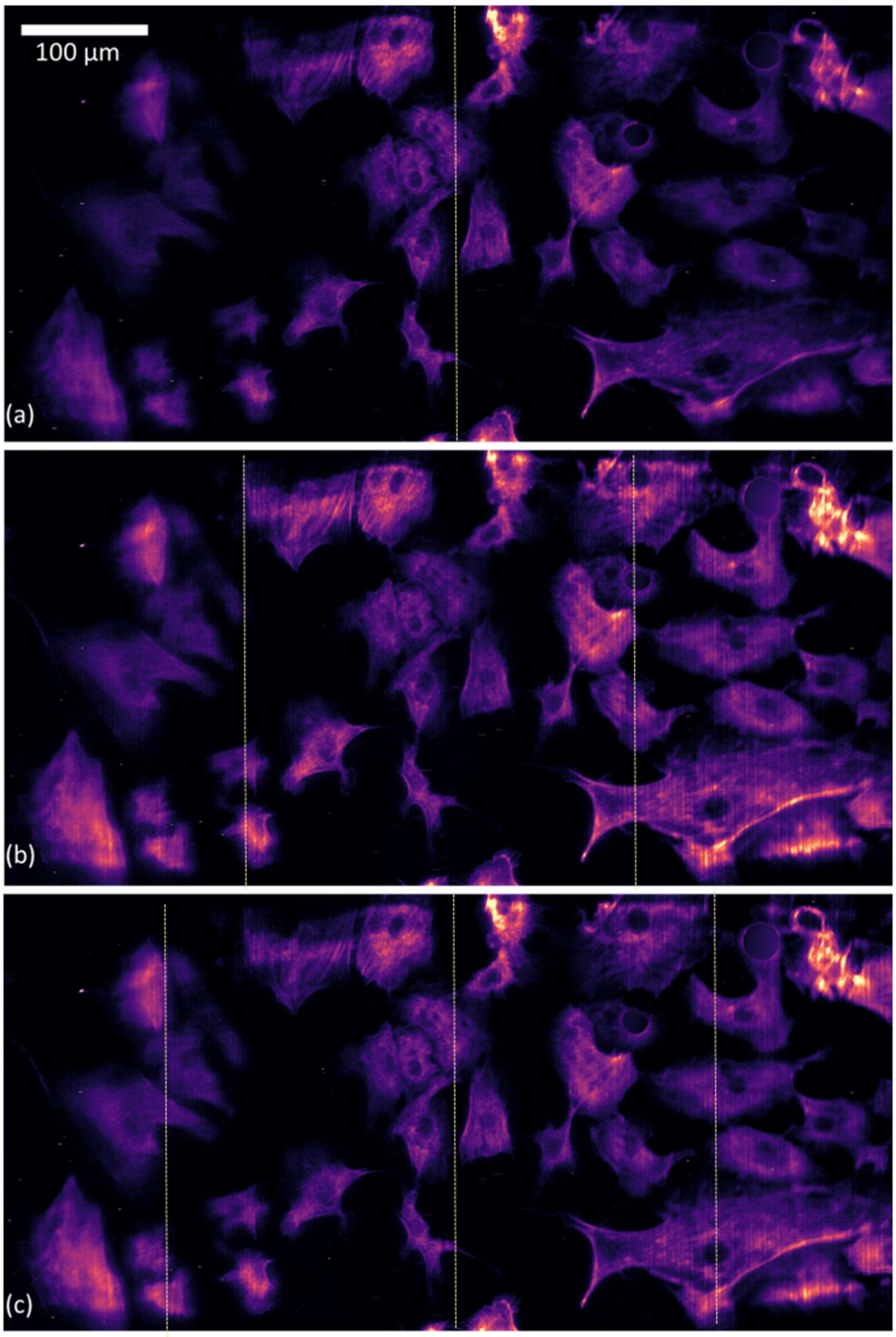

Figure 83. Maximum intensity projections after fitting a linear response for the MEMS static angle slide with the light-sheet focus at (a) x=0µm (b) x1= -160 µm and x2 = 160 µm (c) x1= -225 µm, x2= 0 µm and x3 = 225 µm. (Correction of saturated artefacts was performed in a similar way to Figure 81) Dashed lines show locations of light-sheet focus.

A coordinate transform of the stacks is suggested in order to collect the images of the thin BPAE cell sample in its original, microscope slide coordinate system. Conversely

to the angled resliced method used in chapter 4.3.3 for the same outcome, in this chapter the coordinate transform is accomplished with the Transform J : Rotate tool. The xz stack of Figure 82 (c) is rotated by 20 degrees with isotropic resampling, resulting in Figure 84. This will ensure that the voxel of the image is resampled during rotation with each dimension matching the dimension of the smallest value. In the case of the example the voxel size is 0.36 μm^3.

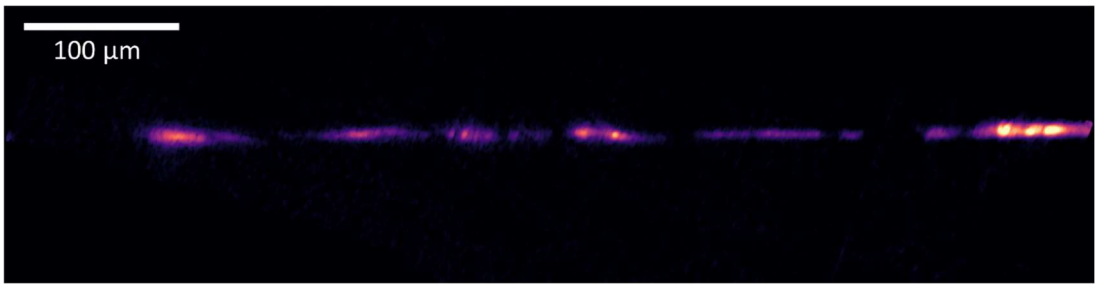

Figure 84.Result of xz stack Transform J:Rotate rotation by 20°. The resulted stack is now transformed to the x'z' system.

The resulting coordinate system is the x'z' as it has also been presented in chapter 4.3.4. The process is repeated for all three stacks. The x'y' projection can be accessed by re-slicing the stack vertically. The maximum intensity projections (x'y) for the three stacks are shown in Figure 85. The results present an accurate representation of the monolayer BPAE actin network with the x/x' ratio being defined by cos20=0.94 . The resulting new width of the FOV is extended to 741.7 µm while the height remains the same at 344.8 µm. Due to the nature of the sample it is not possible to estimate the thickness in the z' direction as it is expected to be in the tenths of micrometers and well below the axial resolution of the system.

In conclusion, the imaging of the cell slice in this case was accomplished for the three different scenarios representing the light-sheet focus position changes within the FOV. The results confirmed the belief that the method of axially scanning the light-sheet will benefit the image quality in terms of SNR. Additionally, the alternative methods shown for the correction of the MEMS non-linearity and coordinate transform may lead to more practical and efficient processing of such stacks.

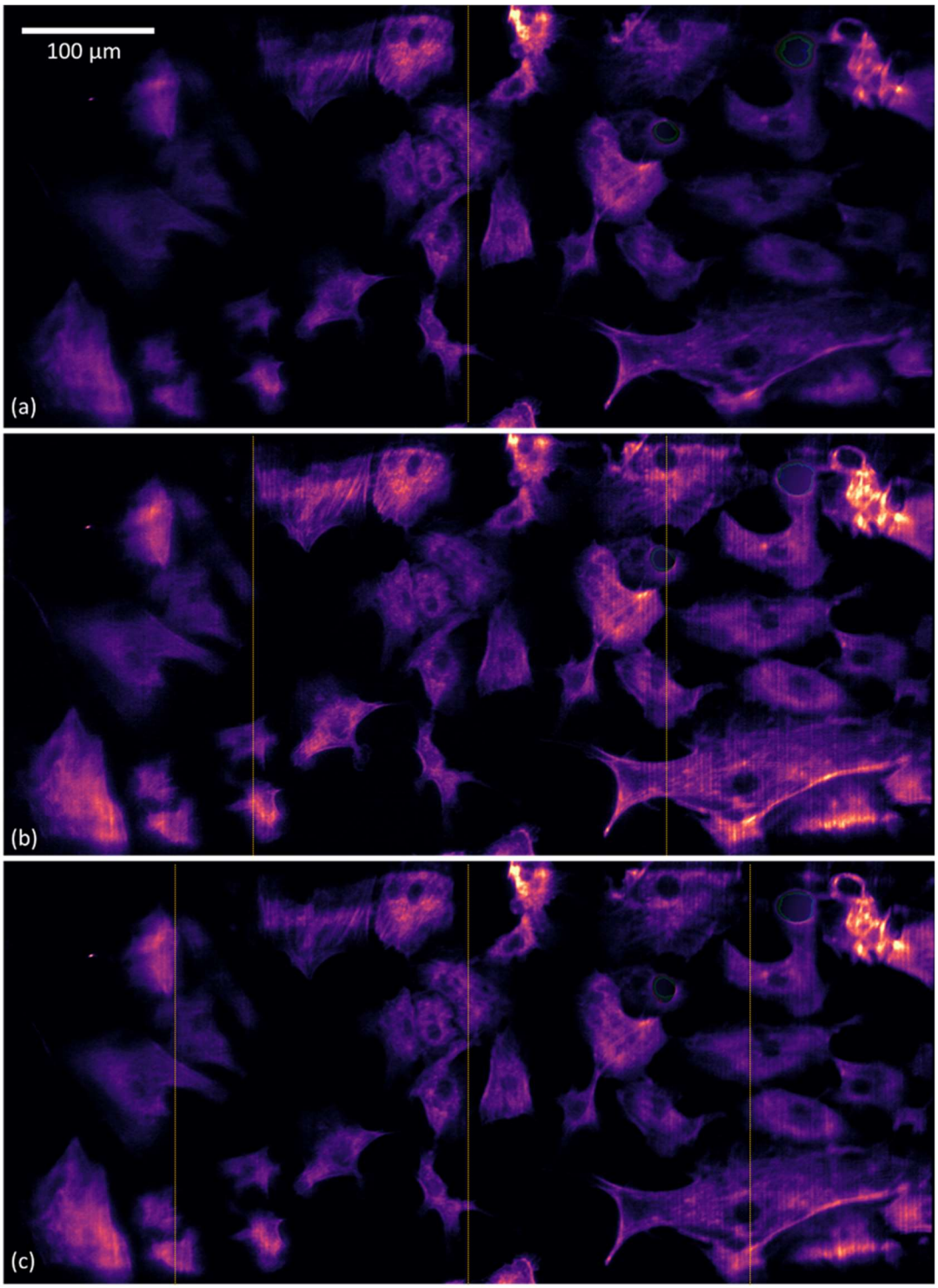

Figure 85. Maximum projection of x' y' coordinates after the rotation of the original coordinate system. The three different figures correspond to the different scenariaos analyzed with the waist of the light-sheet being positioned at (a) x=0 µm (b) x1= -160 µm and x2 = 160 µm (c) x1= -225 µm, x2= 0 µm and x3 = 225 µm.

5.4 Summary

In this chapter, focus is given on designing an alternate version of a miniaturized LSFM. This version of the LSFM system focused on expanding on features that were considered limiting such as the maximum addressable imaged depth in the z-axis. For this reason, the electrothermal MEMS mirror was used instead of the PZ MEMS as it has been shown to have over two times the angular range in the respective axis. In the same spirit a set of changes were made in the equipment, that was believed to contribute to the overall imaging performance and capability of the LSFM system without the risk of significant size or cost increase. Those changes have to do with the camera that provides now a larger FOV than before and the tunable lens with an increased aperture capable of collecting more light from the illuminated sample. But one of the main features of this microscope is the inclusion of a tunable lens in the illumination path. The EL-3-10 was positioned right before the light-sheet focusing lens in a special coupled 3D printed holder and is able to change the beam waist position of the light-sheet along its propagation axis. In this way, the axial resolution along z is homogenized and does not suffer to the same extent by the Gaussian beam expansion. Specifically, three different scenarios were presented with the beam waist left in the original central position of the FOV, the beam being placed in two positions and the beam being placed in 3 different positions. The scenarios of the multiple beam positions required the acquisition of two and three stacks respectively that were later combined into one imaging stack for each scenario. The results showed a satisfactory level of contrast improvement in the edges of the FOV with the use of the axial scan that can be attributed to the homogeneity of the light-sheet while imaging speed has been reduced due to the requirement of acquiring up to 3 times as many images. Finally, an alternate practical approach is presented for the sigmoid response correction and the coordinate rotation, making use of Fiji tools and providing a simpler methodology of visualizing the sample in the microscope slide coordinates.

6 Discussion

This chapter aims to discuss several key conclusions of the work that has been presented in the previous chapters. Specifically, key differences between the optical elements and optical setups, and methodologies that have been used in the two versions of miniaturized LSFM are analysed here.

6.1 2D MEMS Mirrors

The MEMS mirrors introduced in this work are considered the fundamental elements behind the operation of the LSFM system. The characterization chapters (3.1 3.2) focused on presenting the specification and capabilities of the devices. In this part, it is deemed useful to compare the key characteristics of the two MEMS as well as discuss on the possible limitations that they pose.

Table 2. Comparison between piezoelectrically actuated MEMS (PZ MEMS) and electrothermally actuated MEMS (ET MEMS)

MEMS mirrors	**Static TOSA max. (Two actuators)**	**Resonant TOSA max. (Single actuator)**	**Different actuation mechanism for the two axes**	**Radius of curvature**
PZ MEMS	±1.5°	27°	Yes	20 m
ET MEMS	±4°	5.5°	No	65 mm

As it is presented in Table 2 the two mirrors can be directly compared in several categories. The static angle of the MEMS is the more critical component when it comes to defining the maximum depth of the imaged volume as it directly relates to the parallel translation of the light-sheet in z. Here, the ET MEMS is the device that can

produce 2.6 times larger TOSA than the PZ MEMS. It is important to note that in the implementation of the two microscopy setups the tunable lens refocusing range was larger than the range of light-sheet translation for the same axis. This practically means that in this scenario the feature that solely defines the range is the static angle. Besides the addressable angle range it is equally important to consider how this range can be achieved. Ideally, the response between the voltage input and the angle output should be linear where each voltage step corresponds to the same increase in angle. Unfortunately, this hasn't been the case for either the PZ MEMS and ET MEMS. As shown in 3.1.2 and 3.2.2 the response of the angle is non-linear in both cases around 0 as the response rate changes with the variation of the input voltage. This nonlinearity has increased the complexity level of the system control during the implementation stage. In the second implementation of the setup the acquisition software attempted to correct for this, but even in the case of lookup table values and linear fitting of the response curve, small errors could still be noted and had to be corrected. The sigmoid response of the static angle in both cases can have an effect on the 3D imaging results as it was noted in 4.3.3 and 5.3.5 making it complicated to get direct information from the transform rotation and any other post processing task that is further needed in the 3D space. The errors can be attributed to the accuracy of the fitting software and alignment tolerances of the mirror. A similar effort to the one made in chapter 5.3.2 could be made but this time with higher resolution in terms of the lookup table points and possibly with active feedback where the user can manually recalibrate the response in a fast and efficient way. Those tasks could be implemented in future versions of the project and reduce the need of the timely post processing steps in Fiji.

On the other axis the resonant scan angle is the parameter that relates to the height of the light-sheet. In contrast here, the PZ MEMS is the one that can produce a larger angle, equal to 4.9 times of the maximum angle generated by the ET MEMS for single actuator use. It is important to note here that the light-sheet height should practically be tall enough to overcover the FOV that the imaging sensor defines along y. Any increase after that has no practical impact beyond reducing the illumination power in the useable FOV when the imaging optics and camera sensor remain unchanged. As it can be seen from the imaging results presented in chapter 4.3.3 the PZ MEMS resonance angle range has been large enough to produce a scanned light-sheet that

covers the FOV without actuating the device near its damage limit. Additionally, the decoupled static and resonant actuation means that the resonant angle remains the same, regardless of the static angle input, leading to a more stable overall operation off the device. In contrast, the ET MEMS demonstrates more complicated characteristics for its resonant operation. Specifically, the resonance response of the mirror varies significantly as the frequency increases above 2290 Hz. In this case the mirror changes its rotation along the desired axis, with offset movement from the vertical axis being a factor in the outcome. This can be noted in the results as a shift from a scan line to an oval pattern when the laser reflection of the scanning mirror is observed on a screen. The effect of the second axis can be attributed to the axis' eigenfrequency being present around 2300 Hz. This in practice means that only up to 60% of the actuating power of the mirror can be used for the generation of the scan line. Additionally, the behaviour of the rotation axis does not seem to be consistent when the static axis is enabled as it was noted in 3.2.2. The resonant frequency on one axis changes with the actuation of the static axis revealing possible cross-talk between the two device channels, a characteristic that is specific to the operation of this ET MEMS. Both of the two particularities had to be addressed in the implementation phase of the microscope. The use of both vertical actuators in resonance was chosen along with careful alignment and cropping in order to have uniform illumination over the full sample volume, as in the edges of the static movement range there is higher intensity that can affect the imaging result. This is due to the sinusoidal waveform input that can be applied with the use of the Arduino board. In the previous implementations these areas are purposely positioned outside of the FOV to not affect the imaging results, but with the limited maximum range that was available in the ET MEMS setup, it was not possible to implement this with ease.

Finally, it is worth noting the difference in curvature of the surface between the two mirrors. The PZ MEMS is a flat mirror with a radius of curvature of 20 meters. In contrast the ET MEMS has a radius of curvature of 65 mm. In practical terms this means that the two mirrors cannot be used interchangeably in the same optical path design as beam reflection from the curved ET MEMS surface will cause a collimated beam to be focused whereas reflection of the PZ MEMS of the same beam will not affect its collimation. For this reason, the microscope set up of the ET MEMS

incorporated a correction approach with the curvature correction lens before the MEMS at a 2F distance to ensure that the beam is collimated before entering the telescope path. But the inclusion of curved optical components like the lens and MEMS as well as the angles that need to be introduced in order to implement this, can affect negatively the end result of the beam. This can be in the form of aberrations such as astigmatism that are likely present.

It is safe to say that the regardless the plethora of advantages that the two MEMS devices bring to the design and implementation of the microscopy setups, they also pose a set of constraints that need consideration and further work. In some of the issues presented above, such as, the linearity of the static angle response for both MEMS or the nonlinear resonance response of the PZ MEMS, more focus can be given on further correction through control software approaches. This could minimize nonlinear behaviour of the MEMS in those cases. In cases where the imaging volume was limited by only the MEMS, further improvement could be achieved with exploring the use of another MEMS mirror that can follow both a bigger and a more linear angle response. It is important to remind here that none of the two devices were specifically designed for LSFM. This can explain certain limitations they pose either in their quasi-static or resonant response. At the start of the presented research work, the vast majority of MEMS mirrors were part of research projects and not commercially available. At the moment the field of MEMS mirror is getting a number of commercially available products to market in a range of packaging options. Companies like, Mirrorcle, Ultimems, Hamamatsu, Maradin, and Stanley have commercialized 2D MEMS mirrors capable of performing the tasks required for miniaturized LSFM. Additionally, off the shelf products like the 2D fast scanning mirror from Optotune can be used as an alternative option. Even though the device is not a MEMS in its strictly technical term, due to its comparatively bigger size, it retains a lot of the advantages such as being relatively inexpensive and capable of both a fast-resonant axis and a quasi-static actuation.

6.2 Implementing and Characterizing a Miniaturized LSFM Design

The implementation of two versions of the miniaturized LSFM system can be used as a point of discussion and reflection of the achieved results and needs of each setup. Specifically, Table 3 summarizes the fundamental categories form comparison between the miniaturized LSFM and axially scanned miniaturized LSFM setups.

Table 3. Comparison between the two microscopy setups

Microscopy setup	Imaging volume (Length x Height x Width)	Lateral resolution	Axial resolution (light-sheet thickness)	Light-sheet width < 10.5 μm over a length of
Miniaturized LSFM	435 x 140 x 60 μm³	1.1 μm	3.8 μm	200
Axially scanned miniaturized LSFM	697 x 344 x 261.3 μm³	1.1 μm	7.1 μm	Up to 697 μm

The imaging volume is an important specification of every 3D microscope, and as LSFM is traditionally used for bigger samples a respectively large FOV is often preferable. In that spirit, targeted effort was made to increase the imaging volume between the first and second design. The lateral parameters of the FOV (x,y) have been increased by a factor of 1.4 and 1.6 respectively. Since both setups use the same 20x objective, the increase of the FOV can be attributed to the different camera used according to equation of chapter 4.2.1. Specifically, the IDS camera has a larger sensor size allowing for imaging of a larger area. Furthermore, the fact that the same objective has been used in both setups results in the same lateral resolution for both microscopes at 1.1 μm. According to the theoretical value of resolution for the used objective and

wavelength of emission, the expected resolution value was in the sub-micron range. In reality this number can be increased by a few factors such as aberrations and overall quality of the microscope objective. We believe that the objective low-end price poses expected limitation in its quality and as a result affect the expected resolution.

The axial resolution in both microscopes is defined by the light-sheet thickness since the depth of field of the imaging arm is measured at 13.5 μm and thus higher than the thickness of 3.8 μm and 7.1μm in both cases respectively. What it is important to focus on regarding the light-sheet thickness and axial resolution is how it is preserved in areas far away from the centre of the FOV where due to the Gaussian beam identity of the beam the thickness will increase. So, one has to consider the imaging needs and capabilities of the system to balance this trade-off. In other words, the "tighter" a beam is focused, the more drastic is the increase occurring away from the centre of the beam waist. In practice this can be observed in the first microscopy setup where the illumination path lenses have been chosen for a small thickness beam achieving a FWHM of 3.8 μm. The confocal parameter was measured 76 μm while the shift to the next order of magnitude is observed at 100 μm away from the centre of the beam waist in each direction where the FWHM of the beam jumps to 10μm, a factor of 2.6 compared to the axial resolution at the centre. Achieving a more uniform light-sheet is always a balancing act, as based on the Gaussian equation the way to achieve this usually means sacrificing the beam waist thinness and is up to the microscope targeted characteristic to evaluate this compromise. In that spirit the imaging optics of the second microscopy set up were selected towards a more balanced approach resulting in a beam waist of 7.1 μm FWHM at the centre of the FOV. In this case the confocal parameter is extended to 210 μm (less than 1/3 of the FOV) which also roughly coincides with the range that the thickness of the light-sheet stays within the same order of magnitude. A dedicated feature is introduced in this microscopy setup that is predominantly managing to keep a uniform light-sheet and extend it throughout the entire FOV x axis. That includes the integration of the tunable lens and the methodology of acquiring 2 or 3 stacks where the light-sheet focused being "scanned" axially in each iteration as described in chapter 5.3.1. This approach signified the benefits of light-sheet thickness uniformity in the FOV even with an increased starting light-sheet thickness compared to the first microscopy setup. It is important to note

that this approach can pose its own limitations as the current implementation of the tunable lens scanning increases the time of acquisition. This would also be more prominent in the event of a tighter focused beam where the iterations of achieving a uniform beam would be even more leading to respective increase in acquisition time. A small correction to this would be the imaging of smaller ROIs of interest around the focused light-sheet and then a recombination of those ROIs to create the final stack, trying to mimic to an extent how the optimal solution of a rolling shutter camera could tackle this.

Finally, it is important to note that the true benefits of the axial translation of the light-sheet would be easier to appreciate with a sample of larger thickness as the information of the z slices would reveal imaging with better sectioning, with the increase of the focus points within the FOV.

7 Conclusions and Future Work

This thesis has shown the development and characterization of two variations of a small foot-print MEMS mirror enabled LSFM setup that has all-optical beam scanning and can image microscope slide mounted samples.

The development of the microscopy systems brought together a novel combination of active optical elements and custom 3D printed optical and mechanical components for a compact imaging solution. The use of 2D MEMS mirrors has been proposed for both the generation of the light-sheet and its z scan translation over the illuminated volume depth. The functionalities of the MEMS technology along with the small size factor proved to be highly beneficiary towards the purpose of the project. Specifically, the 2D PZ mems mirror was introduced and characterized in terms of its design and operational characteristics. The 1.1 mm diameter mirror silicon/PZT MEMS chip, was capable of achieving a static TOSA of up to ±1.5° on one axis with a resonant TOSA of up to 27° on the vertical axis. Furthermore, another type of MEMS mirror has been presented in this thesis. The 2D ET MEMS is focusing on electrothermal actuation benefiting of the thermal properties of its silicon structure and custom suspension design. This mirror was capable of TOSA of ±4° and a resonant angle of up to 5.5° for single actuator use.

Another active optical element found beneficial for the development of a compact LSFM system is the tunable lens, either as a refocusing element in the detection path of the microscope or as a varifocal axial scanner in the illumination path. Two tunable lenses by Optotune were presented in this thesis with their main difference lying in the aperture of the lens of either 3mm or 10mm. The electromagnetically driven mirrors were also capable of changing their curvature with their respective maximum optical power values reaching 100 dpt and 300 dpt respectively.

Finally, the introduction to the fundamental optical elements was completed with the presentation of the 3D printed 30°/60° prism, and expended work that was facilitated within the 3D printing environment. A dedicated protocol was presented on how to fabricate the prism and post-process it to achieve glass-like surface quality. The use of

the 3D printed was also proved to be beneficial for the optical holders that house the miniature lenses of the system. The design focused on how to make the most of the limited space with a safe and stable custom lens frame design that fits into the Thorlabs half inch lens tube using the company's retainer rings.

The integration of the 2D PZ MEMS mirror and the 3mm tunable lens in an orthogonal optical design as it has been described in this thesis, formed the first iteration of the miniaturized LSFM setup. In this design the PZ electric MEMS is positioned at 45° angle before a 3-lens telecentric path. The fast scan of the mirror generates the light-sheet where its minimum thickness is measured at 3.8 μm, equal to the axial resolution. Equally the quasi-static scan on the orthogonal axis, resulted in a 60 μm translation of the light-sheet along the depth of the imaged volume. The change of curvature of the tunable lens that is located behind the imaging objective in the detection path allows the imaging of each one of the resulted illuminated planes. Both elements were controlled by an Arduino code while their synchronization was accomplished within the LabVIEW environment. A user interface was also developed within the same environment to facilitate the imaging experiments. The device responsible for the capturing the information of each plane is the sCMOS camera. The imaging path optics resulted in a lateral resolution of 1.1 μm and a FOV of 435 μm x 246 μm. The microscope was evaluated for its performance using a microscopy slide as a test sample. The optimization of the imaging a microscope slide at an oblique angle was possible with the insertion of the 3D printed prism in the system that managed to significantly reduce optical aberrations. Imaging results of a microscope slide using submicrometric nanobeads confirmed the initial characterizations regarding the axial and lateral resolution of the microscope. Finally, the imaging of a cell slide was also presented. In this case a protocol was developed to explore the coordinate transform from the axis of the microscope to the coordinate axis of the slide, that was deemed more appropriate for the presentation of such results.

The next part of the research focused on specific improvements that could be implemented on the features of the miniaturized LSFM system while keeping the cost in relatively similar sub 10000 GBP levels. The updated microscopy setup was developed on the same basis with the generation and translation of the light-sheet along the depth of the imaged volume being a result of a 2D MEMS mirror while the

corresponding change of focus to the illuminated plane being attributed to the use of a detection tunable lens. The uses of the ET MEMS mirror instead of the previously used MEMS assisted in increasing at 261.3 μm the illuminated volume depth that could be addressed as it could achieve a higher quasi-static angle. The FOV using a larger sCMOS camera chip device is increased to 697 μm x 344 μm. In an effort to increase the performance of the imaging system an electrical tunable lens with higher aperture was selected (diameter of 10 mm instead of 3 mm). Furthermore, the integration of a tunable lens was introduced in the illumination path. The purpose of the lens was to generate a homogenously thin light-sheet through the whole FOV. The performance of the lens in the imaging was evaluated with a methodology that used the repetition of the same z stack for multiple position of the light-sheet focus. The resulting stacks were cropped in predefined positions and recombined together in a way that the light-sheet appeared homogenous in a recombined stack. The results focused on a comparison between the original central light-sheet focus and the recombined stacks of 2 and 3 light-sheet focus points within the FOV. The outcome of the use of the tunable lens in the illumination path was a light-sheet that remains homogeneous ranging from its minimum width of 7.1 μm to a maximum width of 10.5 μm for a range of x= 697 μm. It is important to note that this is also the axial resolution of the system. The respective lateral resolution remains consistent in the 1.1 μm range. In terms of the results presentation, again the stacks are processed to a transformation of the coordinate axis, and presented for the three different cases.

In summary, the work presented in this thesis showed a promising set of results for the initial implementations of developing a miniaturized LSFM system. The main objectives of the research have been explored and met through a series of characterization and evaluation experiments that were documented in the previous chapters of this work. But it also opens an equally promising amount of future work that can rely on the current systems and experimental findings. As it has been suggested previously the setups can be benefited with the use of MEMS devices that recently have become available in the market and offer a more stable operation, with larger angle capabilities. Their availability as commercial products also can benefit their use as they can easily become available in case of a breakdown compared to custom made devices. In the field of possible hardware replacements, a direct upgrade

to the system can come with the integration of a camera with a rolling shutter mode. This camera, even though more expensive, can be used to synchronize its readout with the moving of the axial scanning tunable lens for homogenously thin light-sheet imaging in a faster manner than in the current implementation.

Additionally, the system can be benefited by a change in the orientation of the orthogonal axis similarly to the work that has been presented by others [72], [112]. Such a configuration would allow for a more straightforward approach to sample mounting and possible use of sample immersion configuration with appropriate dish chambers with imaging medium. In fact, the small scale of the microscopy systems allows the physical rotation of the microscope as the individual components are mounted on a free-standing breadboard of the required footprint. This is usually a less flexible adjustment in most microscopy optical systems that are directly mounted on the optical table.

Summing up, it is important to outline the system's need to be used with a variety of samples. Even though the imaging of a sample is usually a result of a bigger research project, potentially with a collaborator form the field of life sciences, it is the ultimate goal for a microscope to be evaluated under such circumstances. In the project presented, the focus was given in the development of the technology with test samples. But as it has been mentioned in this thesis the design of the system allows a certain degree of flexibility with the types of systems that can be imaged. The resolution and FOV of the system would make it a solid choice for studies on cleared samples such us cleared embryonic organs that are being studied in developmental biology and gene expression studies or microfluidic devices used in disease modelling studies. In the field of live imaging and considering the suggested improvement the system could be used in zebrafish embryo studies. Of course, for any such study the microscope would have to be modified with environmental controls to keep the sample in stable condition and receive further optimizations in terms of its temporal resolution. Even though the microscope slide is the suggested option for the sample housing, the system could also be used with petri dish, or different types of containers considering the microscope assumes a change in orientation axis. These types of improvements and suggestions could potentially involve such systems in high-impact studies. As a result, they can

fulfill the aim of developing imaging instrumentation that enables the collection of data leading to ground-breaking scientific results.

8 References

[1] S. Liu, P. Hoess, and J. Ries, “Super-Resolution Microscopy for Structural Cell Biology,” *Annual Review of Biophysics*, vol. 51. Annual Reviews, pp. 301–326, May 09, 2022. doi: 10.1146/annurev-biophys-102521-112912.

[2] Y. Park, C. Depeursinge, and G. Popescu, “Quantitative phase imaging in biomedicine,” *Nat. Photonics*, vol. 12, no. 10, pp. 578–589, 2018.

[3] W. C. Lemon and K. McDole, “Live-cell imaging in the era of too many microscopes,” *Curr. Opin. Cell Biol.*, vol. 66, pp. 34–42, Oct. 2020, doi: 10.1016/J.CEB.2020.04.008.

[4] “ZEISS Lightsheet 7 – Light Sheet Microscope.” https://www.zeiss.com/microscopy/en/products/light-microscopes/light-sheet-microscopes/lightsheet-7.html (accessed May 07, 2023).

[5] “LS2 Live - Viventis Microscopy.” https://viventis-microscopy.com/products/ls2-live/ (accessed May 07, 2023).

[6] E. H. K. Stelzer *et al.*, “Light sheet fluorescence microscopy,” *Nat. Rev. Methods Prim. 2021 11*, vol. 1, no. 1, pp. 1–25, Nov. 2021, doi: 10.1038/s43586-021-00069-4.

[7] H. Siedentopf and R. Zsigmondy, “Uber Sichtbarmachung und Größenbestimmung ultramikoskopischer Teilchen, mit besonderer Anwendung auf Goldrubingläser,” *Ann. Phys.*, vol. 315, no. 1, pp. 1–39, 1902, doi: 10.1002/ANDP.19023150102.

[8] A. H. Voie, D. H. Burns, and F. A. Spelman, “Orthogonal-plane fluorescence optical sectioning: Three-dimensional imaging of macroscopic biological specimens,” *Journal of Microscopy*, vol. 170, no. 3. pp. 229–236, 1993. doi: 10.1111/j.1365-2818.1993.tb03346.x.

[9] E. H. K. Stelzer *et al.*, “A new tool for the observation of embryos and other large specimens: confocal theta fluorescence microscopy,” *J. Microsc.*, vol.

179, no. 1, pp. 1–10, 1995, doi: 10.1111/j.1365-2818.1995.tb03608.x.

[10] J. Huisken, J. Swoger, F. Del Bene, J. Wittbrodt, and E. H. K. Stelzer, “Optical sectioning deep inside live embryos by selective plane illumination microscopy,” *Science*, vol. 305, no. 5686, pp. 1007–1009, 2004, doi: 10.1126/science.1100035.

[11] M. Renz, “Fluorescence microscopy—A historical and technical perspective,” *Cytom. Part A*, vol. 83, no. 9, pp. 767–779, Sep. 2013, doi: 10.1002/CYTO.A.22295.

[12] A. Jabłoństski, “Efficiency of Anti-Stokes Fluorescence in Dyes,” *Nat. 1933 1313319*, vol. 131, no. 3319, pp. 839–840, 1933, doi: 10.1038/131839b0.

[13] J. W. Lichtman and J.-A. Conchello, “Fluorescence microscopy,” *Nat. Methods*, vol. 2, no. 12, pp. 910–919, 2005.

[14] Stokes, G.G. , “XXX. On the change of refrangibility of light,” *Philos. Trans. R. Soc. London*, vol. 142, pp. 463–562, Dec. 1852, doi: 10.1098/RSTL.1852.0022.

[15] P. Rodríguez-Sevilla, S. A. Thompson, and D. Jaque, “Multichannel Fluorescence Microscopy: Advantages of Going beyond a Single Emission,” *Adv. NanoBiomed Res.*, vol. 2, no. 5, p. 2100084, 2022.

[16] J. Kapuscinski, “DAPI: a DNA-Specific Fluorescent Probe,” *Biotechnic & histochemistry*, vol. 70, no. 5, pp. 220–233, 2009, doi: 10.3109/10520299509108199.

[17] M. Melak, M. Plessner, and R. Grosse, “Actin visualization at a glance,” *Journal of cell science, 130(3), pp.525-530*, Feb. 2017, doi: 10.1242/DEV.150052.

[18] K. Im, S. Mareninov, M. F. P. Diaz, and W. H. Yong, “An introduction to Performing Immunofluorescence Staining,” *Methods Mol. Biol.*, vol. 1897, p. 299, 2019, doi: 10.1007/978-1-4939-8935-5_26.

[19] R. Yuste, “Fluorescence microscopy today,” *Nat. Methods 2005 212*, vol. 2, no.

12, pp. 902–904, Dec. 2005, doi: 10.1038/nmeth1205-902.

[20] C. Stewart and J. Giannini, “Inexpensive, open source epifluorescence microscopes,” *J. Chem. Educ.*, vol. 93, no. 7, pp. 1310–1315, Jul. 2016, doi: 10.1021/ACS.JCHEMED.5B00984/ASSET/IMAGES/LARGE/ED-2015-00984T_0005.JPEG.

[21] A. D. Elliott, “Confocal Microscopy: Principles and Modern Practices,” *Curr. Protoc. Cytom.*, vol. 92, no. 1, p. e68, Mar. 2020, doi: 10.1002/CPCY.68.

[22] A. Diaspro, G. Chirico, C. Usai, P. Ramoino, and J. Dobrucki, “Photobleaching,” *Handb. Biol. Confocal Microsc. Third Ed.*, pp. 690–702, 2006, doi: 10.1007/978-0-387-45524-2_39/COVER.

[23] P. P. Laissue, R. A. Alghamdi, P. Tomancak, E. G. Reynaud, and H. Shroff, “Assessing phototoxicity in live fluorescence imaging,” *Nat. Methods 2017 147*, vol. 14, no. 7, pp. 657–661, Jun. 2017, doi: 10.1038/nmeth.4344.

[24] P. O. Bayguinov, D. M. Oakley, C. Shih, D. J. Geanon, M. S. Joens, and J. A. J. Fitzpatrick, “Modern laser scanning confocal microscopy,” *Curr. Protoc. Cytom.*, vol. 85, no. 1, p. e39, 2018.

[25] J. Oreopoulos, R. Berman, and M. Browne, “Spinning-disk confocal microscopy: present technology and future trends,” *Methods Cell Biol.*, vol. 123, pp. 153–175, 2014.

[26] R. M. Power and J. Huisken, “A guide to light-sheet fluorescence microscopy for multiscale imaging,” *Nat. Methods*, vol. 14, no. 4, pp. 360–373, Apr. 2017, doi: 10.1038/nmeth.4224.

[27] E. Reynaud, U. Kržič, K. Greger, E. S.-H. journal, and undefined 2008, “Light sheet-based fluorescence microscopy: more dimensions, more photons, and less photodamage,” *Taylor Fr.*, vol. 2, no. 5, pp. 266–275, Oct. 2010, doi: 10.2976/1.2974980.

[28] M. Jemielita, M. J. Taormina, A. Delaurier, C. B. Kimmel, and R. Parthasarathy, “Comparing phototoxicity during the development of a zebrafish craniofacial bone using confocal and light sheet fluorescence microscopy techniques,” *J.*

Biophotonics, vol. 6, no. 11–12, pp. 920–928, Dec. 2013, doi: 10.1002/JBIO.201200144.

[29] J. B. Pawley, *Handbook of biological confocal microscopy: Third edition*. 2006. doi: 10.1007/978-0-387-45524-2.

[30] W. A. Carrington, K. E. Fogarty, L. Lifschitz, and F. S. Fay, "Three-dimensional Imaging on Confocal and Wide-field Microscopes," *Handb. Biol. Confocal Microsc.*, pp. 151–161, 1990, doi: 10.1007/978-1-4615-7133-9_14.

[31] F. Pampaloni, B. J. Chang, and E. H. K. Stelzer, *Light sheet-based fluorescence microscopy (LSFM) for the quantitative imaging of cells and tissues*, vol. 360, no. 1. Springer, 2015, pp. 129–141. doi: 10.1007/s00441-015-2144-5.

[32] P. J. Keller and M. B. Ahrens, "Visualizing Whole-Brain Activity and Development at the Single-Cell Level Using Light-Sheet Microscopy," *Neuron*, vol. 85, no. 3, pp. 462–483, Feb. 2015, doi: 10.1016/J.NEURON.2014.12.039.

[33] Y. Wan, K. Mcdole, and P. J. Keller, "Light-Sheet Microscopy and Its Potential for Understanding Developmental Processes," *Annu. Rev. Cell Dev. Biol.*, 2019, *35*(1), pp.655-681, doi: 10.1146/annurev-cellbio-100818.

[34] R. Tomer, K. Khairy, F. Amat, and P. J. Keller, "Quantitative high-speed imaging of entire developing embryos with simultaneous multiview light-sheet microscopy," *Nat. Methods 2012 97*, vol. 9, no. 7, pp. 755–763, Jun. 2012, doi: 10.1038/nmeth.2062.

[35] D. Takao, A. Taniguchi, T. Takeda, S. Sonobe, and S. Nonaka, "High-Speed Imaging of Amoeboid Movements Using Light-Sheet Microscopy," *PLoS One*, vol. 7, no. 12, Dec. 2012, doi: 10.1371/JOURNAL.PONE.0050846.

[36] E. M. C. Hillman, V. Voleti, W. Li, and H. Yu, "Light-Sheet Microscopy in Neuroscience," *Annu. Rev. Neurosci.*, vol. 42, p. 295, Jul. 2019, doi: 10.1146/ANNUREV-NEURO-070918-050357.

[37] C. J. Greer and T. E. Holy, "Fast objective coupled planar illumination microscopy," *Nat. Commun. 2019 101*, vol. 10, no. 1, pp. 1–14, Oct. 2019, doi: 10.1038/s41467-019-12340-0.

[38] J. Andilla, E. J. Gualda, O. E. Olarte, and P. Loza-Alvarez, “Light-sheet microscopy: a tutorial,” *Adv. Opt. Photonics, Vol. 10, Issue 1, pp. 111-179*, vol. 10, no. 1, pp. 111–179, Mar. 2018, doi: 10.1364/AOP.10.000111.

[39] E. Remacha, L. Friedrich, J. Vermot, and F. O. Fahrbach, “How to define and optimize axial resolution in light-sheetmicroscopy: a simulation-based approach,” *Biomed. Opt. Express*, vol. 11, no. 1, p. 8, Jan. 2020, doi: 10.1364/BOE.11.000008.

[40] H. Sun, *A practical guide to handling laser diode beams*, vol. 147. Springer, 2015.

[41] J. Huisken and D. Y. R. Stainier, “Even fluorescence excitation by multidirectional selective plane illumination microscopy (mSPIM),” *Opt. Lett. Vol. 32, Issue 17, pp. 2608-2610*, vol. 32, no. 17, pp. 2608–2610, Sep. 2007, doi: 10.1364/OL.32.002608.

[42] J. M. Girkin and M. T. Carvalho, “The light-sheet microscopy revolution,” *J. Opt.*, vol. 20, no. 5, p. 053002, Apr. 2018, doi: 10.1088/2040-8986/AAB58A.

[43] P. J. Keller, A. D. Schmidt, J. Wittbrodt, and E. H. K. Stelzer, “Reconstruction of Zebrafish Early Embryonic Development by Scanned Light Sheet Microscopy,” *Science.*, vol. 322, no. 5904, pp. 1065–1069, Nov. 2008, doi: 10.1126/science.1162493.

[44] F. O. Fahrbach, V. Gurchenkov, K. Alessandri, P. Nassoy, and A. Rohrbach, “Light-sheet microscopy in thick media using scanned Bessel beams and two-photon fluorescence excitation,” *Opt. Express*, vol. 21, no. 11, pp. 13824–13839, 2013, doi: 10.1364/oe.21.013824.

[45] T. Meinert and A. Rohrbach, “Light-sheet microscopy with length-adaptive Bessel beams,” *Biomed. Opt. Express*, vol. 10, no. 2, p. 670, 2019, doi: 10.1364/boe.10.000670.

[46] T. Vettenburg *et al.*, “Light-sheet microscopy using an Airy beam,” *Nat. Methods*, vol. 11, no. 5, pp. 541–544, 2014, doi: 10.1038/nmeth.2922.

[47] B. C. Chen *et al.*, “Lattice light-sheet microscopy: Imaging molecules to

embryos at high spatiotemporal resolution," *Science*, vol. 346, no. 6208, p. 1257998, Oct. 2014, doi: 10.1126/science.1257998.

[48] K. M. Dean and R. Fiolka, "Uniform and scalable light-sheets generated by extended focusing," *Opt. Express*, vol. 22, no. 21, pp. 26141–26152, Oct. 2014, doi: 10.1364/OE.22.026141.

[49] M. Duocastella, C. B. Arnold, and J. Puchalla, "Selectable light-sheet uniformity using tuned axial scanning," *Microsc. Res. Tech.*, vol. 80, no. 2, pp. 250–259, Feb. 2017, doi: 10.1002/JEMT.22795.

[50] R. M. Power and J. Huisken, "Adaptable, illumination patterning light sheet microscopy," *Sci. Rep.*, vol. 8, no. 1, p. 9615, Dec. 2018, doi: 10.1038/s41598-018-28036-2.

[51] L. Gao *et al.*, "Extend the field of view of selective plan illumination microscopy by tiling the excitation light sheet," *Opt. Express, Vol. 23, Issue 5, pp. 6102-6111*, vol. 23, no. 5, pp. 6102–6111, Mar. 2015, doi: 10.1364/OE.23.006102.

[52] Q. Fu, B. L. Martin, D. Q. Matus, and L. Gao, "Imaging multicellular specimens with real-time optimized tiling light-sheet selective plane illumination microscopy," *Nat. Commun. 2016 71*, vol. 7, no. 1, pp. 1–10, Mar. 2016, doi: 10.1038/ncomms11088.

[53] J. Andilla, O. E. Olarte, D. Artigas, and P. Loza-Alvarez, "Decoupled illumination detection in light sheet microscopy for fast volumetric imaging," *Opt. Vol. 2, Issue 8, pp. 702-705*, vol. 2, no. 8, pp. 702–705, Aug. 2015, doi: 10.1364/OPTICA.2.000702.

[54] K. M. Dean, P. Roudot, E. S. Welf, G. Danuser, and R. Fiolka, "Deconvolution-free Subcellular Imaging with Axially Swept Light Sheet Microscopy," *Biophys. J.*, vol. 108, no. 12, p. 2807, Jun. 2015, doi: 10.1016/J.BPJ.2015.05.013.

[55] H. Sparks *et al.*, "Development a flexible light-sheet fluorescence microscope for high-speed 3D imaging of calcium dynamics and 3D imaging of cellular

microstructure," *J. Biophotonics*, vol. 13, no. 6, Jun. 2020, doi: 10.1002/JBIO.201960239.

[56] P. N. Hedde and E. Gratton, "Selective plane illumination microscopy with a light sheet of uniform thickness formed by an electrically tunable lens," *Microsc. Res. Tech.*, vol. 81, no. 9, pp. 924–928, Sep. 2018, doi: 10.1002/jemt.22707.

[57] F. F. Voigt *et al.*, "The mesoSPIM initiative: open-source light-sheet microscopes for imaging cleared tissue," *Nat. Methods 2019 1611*, vol. 16, no. 11, pp. 1105–1108, Sep. 2019, doi: 10.1038/s41592-019-0554-0.

[58] B. J. Chang, V. D. P. Meza, and E. H. K. Stelzer, "csiLSFM combines light-sheet fluorescence microscopy and coherent Structured illumination for a lateral resolution below 100 nm," *Proc. Natl. Acad. Sci. U. S. A.*, vol. 114, no. 19, pp. 4869–4874, May 2017, doi: 10.1073/PNAS.1609278114.

[59] C. H. Lu *et al.*, "Lightsheet localization microscopy enables fast, large-scale, and three-dimensional super-resolution imaging," *Commun. Biol.*, vol. 2, no. 1, 2019, doi: 10.1038/s42003-019-0403-9.

[60] M. Friedrich, Q. Gan, V. Ermolayev, G. Harms,, "STED-SPIM: stimulated emission depletion improves sheet illumination microscopy resolution," *Biophysical journal, 100(8), pp.L43-L45, 2011, doi : 10.1016/j.bpj.2010.12.3748*

[61] T. F. Holekamp, D. Turaga, and T. E. Holy, "Fast Three-Dimensional Fluorescence Imaging of Activity in Neural Populations by Objective-Coupled Planar Illumination Microscopy," *Neuron*, vol. 57, no. 5, pp. 661–672, Mar. 2008, doi: 10.1016/j.neuron.2008.01.011.

[62] E. J. Gualda, H. Pereira, T. Vale, M. F. Estrada, C. Brito, and N. Moreno, "SPIM-fluid: open source light-sheet based platform for high-throughput imaging," *Biomed. Opt. Express*, vol. 6, no. 11, pp. 4447–4456, 2015, doi: 10.1364/boe.6.004447.

[63] J. Huisken *et al.*, "Rapid 3D light-sheet microscopy with a tunable lens," *Opt.*

Express, Vol. 21, Issue 18, pp. 21010-21026, vol. 21, no. 18, pp. 21010–21026, Sep. 2013, doi: 10.1364/OE.21.021010.

[64] S. Bakas, D. Uttamchandani, H. Toshiyoshi, and R. Bauer, "MEMS enabled miniaturized light-sheet microscopy with all optical control," *Sci. Reports 2021 111*, vol. 11, no. 1, pp. 1–11, Jul. 2021, doi: 10.1038/s41598-021-93454-8.

[65] J. Huisken, E. H. K. Stelzer, J. Swoger, P. Verveer, and K. Greger, "Multi-view image fusion improves resolution in three-dimensional microscopy," *Opt. Express, Vol. 15, Issue 13, pp. 8029-8042*, vol. 15, no. 13, pp. 8029–8042, Jun. 2007, doi: 10.1364/OE.15.008029.

[66] R. S. Udan, V. G. Piazza, C. W. Hsu, A. K. Hadjantonakis, and M. E. Dickinson, "Quantitative imaging of cell dynamics in mouse embryos using light-sheet microscopy," *Dev.*, vol. 141, no. 22, pp. 4406–4414, Nov. 2014, doi: 10.1242/DEV.111021/VIDEO-6.

[67] A. Kaufmann, M. Mickoleit, M. Weber, and J. Huisken, "Multilayer mounting enables long-term imaging of zebrafish development in a light sheet microscope," *Development*, vol. 139, no. 17, pp. 3242–3247, Sep. 2012, doi: 10.1242/DEV.082586.

[68] M. Weber, M. Mickoleit, and J. Huisken, "Multilayer mounting for long-term light sheet microscopy of zebrafish," *J. Vis. Exp.*, no. 84, Feb. 2014, doi: 10.3791/51119.

[69] R. Galland, G. Grenci, A. Aravind, V. Viasnoff, V. Studer, and J. B. Sibarita, "3D high- and super-resolution imaging using single-objective SPIM," *Nat. Methods 2015 127*, vol. 12, no. 7, pp. 641–644, May 2015, doi: 10.1038/nmeth.3402.

[70] Y. Wu *et al.*, "Inverted selective plane illumination microscopy (iSPIM) enables coupled cell identity lineaging and neurodevelopmental imaging in Caenorhabditis elegans," *Proc. Natl. Acad. Sci. U. S. A.*, vol. 108, no. 43, pp. 17708–17713, Oct. 2011, doi: 10.1073/PNAS.1108494108/SUPPL_FILE/SM06.MOV.

[71] R. McGorty *et al.*, “Open-top selective plane illumination microscope for conventionally mounted specimens,” *Opt. Express*, vol. 23, no. 12, pp. 16142–16153, Jun. 2015, doi: 10.1364/oe.23.016142.

[72] A. K. Glaser *et al.*, “Light-sheet microscopy for slide-free non-destructive pathology of large clinical specimens,” *Nature biomedical engineering* vol. 1, no. 7, pp. 1–10, Jun. 2017, doi: 10.1038/s41551-017-0084.

[73] C. Dunsby, “Optically sectioned imaging by oblique plane microscopy,” *Opt. Express*, vol. 16, no. 25, pp. 20306–20316, Dec. 2008, doi: 10.1364/oe.16.020306.

[74] J. Kim *et al.*, “Oblique-plane single-molecule localization microscopy for tissues and small intact animals,” *Nat. Methods 2019 169*, vol. 16, no. 9, pp. 853–857, Aug. 2019, doi: 10.1038/s41592-019-0510-z.

[75] M. B. Bouchard *et al.*, “Swept confocally-aligned planar excitation (SCAPE) microscopy for high-speed volumetric imaging of behaving organisms,” *Nat. Photonics*, vol. 9, no. 2, pp. 113–119, Jan. 2015, doi: 10.1038/nphoton.2014.323.

[76] E. G. Reynaud, J. Peychl, J. Huisken, and P. Tomancak, “Guide to light-sheet microscopy for adventurous biologists,” *Nat. Methods 2014 121*, vol. 12, no. 1, pp. 30–34, Dec. 2014, doi: 10.1038/nmeth.3222.

[77] F. Amat, B. Höckendorf, Y. Wan, W. C. Lemon, K. McDole, and P. J. Keller, “Efficient processing and analysis of large-scale light-sheet microscopy data,” *Nat. Protoc. 2015 1011*, vol. 10, no. 11, pp. 1679–1696, Oct. 2015, doi: 10.1038/nprot.2015.111.

[78] P. G. Pitrone *et al.*, “OpenSPIM: An open-access light-sheet microscopy platform,” *Nat. Methods*, vol. 10, no. 7, pp. 598–599, Jun. 2013, doi: 10.1038/nmeth.2507.

[79] E. J. Gualda, T. Vale, P. Almada, J. A. Feijó, G. G. Martins, and N. Moreno, “OpenSpinMicroscopy: an open-source integrated microscopy platform,” *Nat. Methods 2013 107*, vol. 10, no. 7, pp. 599–600, Jun. 2013, doi:

10.1038/nmeth.2508.

[80] J. Girstmair, H. K. Moon, C. Brillard, R. Haase, and P. Tomancak, “Time to Upgrade: A New OpenSPIM Guide to Build and Operate Advanced OpenSPIM Configurations,” *Adv. Biol.*, vol. 6, no. 4, p. 2101182, Apr. 2022, doi: 10.1002/ADBI.202101182.

[81] “OpenSPIM.” https://openspim.org/ (accessed Mar. 29, 2024).

[82] “The mesoSPIM Initiative - mesospim.org.” https://mesospim.org/ (accessed Mar. 29, 2024).

[83] J. Girstmair *et al.*, “Light-sheet microscopy for everyone? Experience of building an OpenSPIM to study flatworm development,” *BMC Dev. Biol.*, vol. 16, no. 1, pp. 1–16, Jun. 2016, doi: 10.1186/S12861-016-0122-0/TABLES/4.

[84] Y. Wu *et al.*, “Reflective imaging improves spatiotemporal resolution and collection efficiency in light sheet microscopy,” *Nat. Commun. 2017 81*, vol. 8, no. 1, pp. 1–12, Nov. 2017, doi: 10.1038/s41467-017-01250-8.

[85] A. K. Glaser *et al.*, “A hybrid open-top light-sheet microscope for versatile multi-scale imaging of cleared tissues,” *Nat. Methods 2022 195*, vol. 19, no. 5, pp. 613–619, May 2022, doi: 10.1038/s41592-022-01468-5.

[86] C. Garbellotto and J. M. Taylor, “Multi-purpose SLM-light-sheet microscope,” *Biomed. Opt. Express, Vol. 9, Issue 11, pp. 5419-5436*, vol. 9, no. 11, pp. 5419–5436, Nov. 2018, doi: 10.1364/BOE.9.005419.

[87] J. Nylk *et al.*, “A compact Airy beam light sheet microscope with a tilted cylindrical lens,” *Biomed. Opt. Express, Vol. 5, Issue 10, pp. 3434-3442*, vol. 5, no. 10, pp. 3434–3442, Oct. 2014, doi: 10.1364/BOE.5.003434.

[88] B. Moretti, M. Wappner, H. E. Grecco, and N. P. Müller, “Compact and reflective light-sheet microscopy for long-term imaging of living embryos,” *Appl. Opt. Vol. 59, Issue 13, pp. D89-D94*, vol. 59, no. 13, pp. D89–D94, May 2020, doi: 10.1364/AO.383026.

[89] Z. Yang, P. Haslehurst, S. Scott, N. Emptage, and K. Dholakia, “A compact

light-sheet microscope for the study of the mammalian central nervous system," *Sci. Reports 2016 61*, vol. 6, no. 1, pp. 1–7, May 2016, doi: 10.1038/srep26317.

[90] B. Diederich *et al.*, "A versatile and customizable low-cost 3D-printed open standard for microscopic imaging," *Nat. Commun. 2020 111*, vol. 11, no. 1, pp. 1–9, Nov. 2020, doi: 10.1038/s41467-020-19447-9.

[91] P. N. Hedde, "miniSPIM—A Miniaturized Light-Sheet Microscope," *ACS Sensors*, vol. 6, no. 7, pp. 2654–2663, Jul. 2021, doi: 10.1021/ACSSENSORS.1C00607/SUPPL_FILE/SE1C00607_SI_002.AVI.

[92] D. Wang, C. Watkins, and H. Xie, "MEMS mirrors for LiDAR: A review," *Micromachines*, vol. 11, no. 5, p. 456, 2020.

[93] P. Janin, "MEMS devices for the control of trapped atomic particles," PhD Thesis, University of Strathclyde, 2022. doi: 10.48730/4SNA-ET92.

[94] M. H. Kiang, O. Solgaard, K. Y. Lau, and R. S. Muller, "Electrostatic combdrive-actuated micromirrors for laser-beam scanning and positioning," *J. Microelectromechanical Syst.*, vol. 7, no. 1, pp. 27–37, Mar. 1998, doi: 10.1109/84.661381.

[95] R. A. Miller and Y.-C. Tai, "Micromachined electromagnetic scanning mirrors," *Optical Engineering*, vol. 36, no. 5, pp. 1399–1407, May 1997, doi: 10.1117/1.601348.

[96] A. Paterson, R. Bauer, R. Li, C. Clark, W. Lubeigt, and D. Uttamchandani, "Spectral and temporal control of Q-switched solid-state lasers using intracavity MEMS," in *Solid State Lasers XXV: Technology and Devices*, 2016, vol. 9726, p. 97261U. doi: 10.1117/12.2211302.

[97] A. Paterson, R. Bauer, L. Li, W. Lubeigt, and D. Uttamchandani, "Range extension of a bimorph varifocal micromirror through actuation by a peltier element," *IEEE J. Sel. Top. Quantum Electron.*, vol. 21, no. 4, pp. 72–78, Jul. 2015, doi: 10.1109/JSTQE.2014.2381464.

[98] M. Tani, M. Akamatsu, Y. Yasuda, and H. Toshiyoshi, "A two-axis piezoelectric tilting micromirror with a newly developed PZT-meandering

actuator," in *Proceedings of the IEEE International Conference on Micro Electro Mechanical Systems (MEMS)*, 2007. doi: 10.1109/memsys.2007.4432994.

[99] S. T. S. Holmström, U. Baran, and H. Urey, "MEMS laser scanners: A review," *J. Microelectromechanical Syst.*, vol. 23, no. 2, pp. 259–275, 2014, doi: 10.1109/JMEMS.2013.2295470.

[100] Z. Qiu and W. Piyawattanametha, "MEMS-Based Medical Endomicroscopes," *IEEE J. Sel. Top. Quantum Electron.*, vol. 21, no. 4, pp. 376–391, Jul. 2015, doi: 10.1109/JSTQE.2015.2389530.

[101] C. Gorecki and S. Bargiel, "MEMS Scanning Mirrors for Optical Coherence Tomography," *Photonics 2021, Vol. 8, Page 6*, vol. 8, no. 1, p. 6, Dec. 2020, doi: 10.3390/PHOTONICS8010006.

[102] G. K. Fedder, H. Xie, and Y. Pan, "Endoscopic optical coherence tomography based on a microelectromechanical mirror," *Opt. Lett. Vol. 26, Issue 24, pp. 1966-1968*, vol. 26, no. 24, pp. 1966–1968, Dec. 2001, doi: 10.1364/OL.26.001966.

[103] A. D. Aguirre *et al.*, "Two-axis MEMS Scanning Catheter for Ultrahigh Resolution Three-dimensional and En Face Imaging," *Opt. Express*, vol. 15, no. 5, pp. 2445–2453, Mar. 2007, doi: 10.1364/OE.15.002445.

[104] H. Ra, D. Lee, H. J. Shin, K. C. Maitland, O. Solgaard, and R. Richards-Kortum, "Single fiber confocal microscope with a two-axis gimbaled MEMS scanner for cellular imaging," *Opt. Express, Vol. 14, Issue 19, pp. 8604-8612*, vol. 14, no. 19, pp. 8604–8612, Sep. 2006, doi: 10.1364/OE.14.008604.

[105] H. Ra, W. Piyawattanametha, Y. Taguchi, D. Lee, M. J. Mandella, and O. Solgaard, "Two-dimensional MEMS scanner for dual-axes confocal microscopy," *J. Microelectromechanical Syst.*, vol. 16, no. 4, pp. 969–976, Aug. 2007, doi: 10.1109/JMEMS.2007.892900.

[106] C. L. Arrasmith *et al.*, "MEMS-based handheld confocal microscope for in-vivo skin imaging," *Opt. Express, Vol. 18, Issue 4, pp. 3805-3819*, vol. 18, no. 4, pp.

3805–3819, Feb. 2010, doi: 10.1364/OE.18.003805.

[107] H. F. Zhang, K. Maslov, G. Stoica, and L. V Wang, “Functional photoacoustic microscopy for high-resolution and noninvasive in vivo imaging,” *Nat. Biotechnol.*, vol. 24, no. 7, pp. 848–851, 2006, doi: 10.1038/nbt1220.

[108] J. Yao *et al.*, “Wide-field fast-scanning photoacoustic microscopy based on a water-immersible MEMS scanning mirror,” *J. Biomed. Opt.*, vol. 17, no. 8, p. 80505, 2012.

[109] J. Y. Kim, C. Lee, K. Park, G. Lim, and C. Kim, “Fast optical-resolution photoacoustic microscopy using a 2-axis water-proofing MEMS scanner,” *Sci. Rep.*, vol. 5, no. 1, p. 7932, 2015, doi: 10.1038/srep07932.

[110] K. Park, J. Y. Kim, C. Lee, S. Jeon, G. Lim, and C. Kim, “Handheld Photoacoustic Microscopy Probe,” *Sci. Rep.*, vol. 7, no. 1, p. 13359, 2017, doi: 10.1038/s41598-017-13224-3.

[111] P. Tinning, M. Donnachie, J. Christopher, D. Uttamchandani, and R. Bauer, “Miniaturized structured illumination microscopy using two 3-axis MEMS micromirrors,” *Biomed. Opt. Express*, vol. 13, no. 12, pp. 6443–6456, 2022.

[112] J. Landry, S. Hamann, and O. Solgaard, “High-speed axially swept light sheet microscopy using a linear MEMS phased array for isotropic resolution,” *https://doi.org/10.1117/1.JBO.25.10.106504*, vol. 25, no. 10, p. 106504, Oct. 2020, doi: 10.1117/1.JBO.25.10.106504.

[113] R. Bauer and D. Uttamchandani, “MEMS micromirror based light sheet generator for biomedical imaging,” *Int. Conf. Opt. MEMS Nanophotonics*, Sep. 2017, doi: 10.1109/OMN.2017.8051499.

[114] T. Asari, T. Koyama, M. Tani, and H. Toshiyoshi, “A Bi-Axial piezoelectric mems scanning mirror for automobile lighting system,” *Int. Conf. Opt. MEMS Nanophotonics*, vol. 2019-July, pp. 224–225, Jul. 2019, doi: 10.1109/OMN.2019.8925159.

[115] A. Arslan, D. Brown, W. O. Davis, S. Holmstrom, S. K. Gokce, and H. Urey, “Comb-actuated resonant torsional microscanner with mechanical

amplification," *J. Microelectromechanical Syst.*, vol. 19, no. 4, pp. 936–943, 2010.

[116] M. Totzeck, "Interferometry," in *Springer Handbook of Lasers and Optics*, Berlin, Heidelberg: Springer Berlin Heidelberg, 2012, pp. 1255–1283.

[117] E. O. Fanijo, J. G. Thomas, Y. Zhu, W. Cai, and A. S. Brand, "Surface characterization techniques: a systematic review of their principles, applications, and perspectives in corrosion studies," *J. Electrochem. Soc.*, vol. 169, no. 11, p. 111502, 2022.

[118] A. M. Elshurafa, K. Khirallah, H. H. Tawfik, A. Emira, A. K. S. A. Aziz, and S. M. Sedky, "Nonlinear dynamics of spring softening and hardening in folded-MEMS comb drive resonators," *J. Microelectromechanical Syst.*, vol. 20, no. 4, pp. 943–958, 2011.

[119] "Science Foundry." https://science.xyz/services/foundry/ (accessed Jun. 29, 2024).

[120] J. R. Howell, M. P. Mengüç, K. Daun, and R. Siegel, *Thermal radiation heat transfer*. CRC press, 2020.

[121] M. Donnachie, D. Uttamchandani, and R. Bauer, "Thermal dynamics of 2-axis electrothermal MEMS micromirrors," in *2019 International Conference on Optical MEMS and Nanophotonics (OMN)*, 2019, pp. 228–229.

[122] P. Janin, D. Uttamchandani, and R. Bauer, "On-Chip Frequency Tuning of Fast Resonant MEMS Scanner," *J. Microelectromechanical Syst.*, vol. 31, no. 6, pp. 977–983, 2022, doi: 10.1109/JMEMS.2022.3201381.

[123] W. Zong *et al.*, "Large-field high-resolution two-photon digital scanned light-sheet microscopy," *Cell Res. 2015 252*, vol. 25, no. 2, pp. 254–257, Sep. 2014, doi: 10.1038/cr.2014.124.

[124] P. Haslehurst *et al.*, "Fast volume-scanning light sheet microscopy reveals transient neuronal events," *Biomed. Opt. Express, Vol. 9, Issue 5, pp. 2154-2167*, vol. 9, no. 5, pp. 2154–2167, May 2018, doi: 10.1364/BOE.9.002154.

[125] A. K. Chmielewski *et al.*, “Fast imaging of live organisms with sculpted light sheets,” *Sci. Reports 2015 51*, vol. 5, no. 1, pp. 1–9, Apr. 2015, doi: 10.1038/srep09385.

[126] “EL-3-10 lens — Optotune.” https://www.optotune.com/el-3-10-lens (accessed Oct. 20, 2024).

[127] “EL-10-30-C lens — Optotune.” https://www.optotune.com/el-10-30-c-lens (accessed Dec. 10, 2022).

[128] A. K. Glaser *et al.*, “Multi-immersion open-top light-sheet microscope for high-throughput imaging of cleared tissues,” *Nat. Commun.*, vol. 10, no. 1, pp. 1–8, 2019, doi: 10.1038/s41467-019-10534-0.

[129] R. McGorty, H. Liu, D. Kamiyama, Z. Dong, S. Guo, and B. Huang, “Open-top selective plane illumination microscope for conventionally mounted specimens,” *Opt. Express*, vol. 23, no. 12, pp. 16142–16153, 2015, doi: 10.1364/oe.23.016142.

[130] N. Shahrubudin, T. C. Lee, and R. Ramlan, “An overview on 3D printing technology: Technological, materials, and applications,” *Procedia Manuf.*, vol. 35, pp. 1286–1296, 2019.

[131] Rayleigh, “XXXI. Investigations in optics, with special reference to the spectroscope,” The *London, Edinburgh, Dublin Philos. Mag. J. Sci.*, vol. 8, no. 49, pp. 261–274, 1879.

[132] Z. Zhou, B. Pain, and E. R. Fossum, “Frame-transfer CMOS active pixel sensor with pixel binning,” *IEEE Trans. Electron Devices*, vol. 44, no. 10, pp. 1764–1768, 1997, doi: 10.1109/16.628834.

[133] S. Smith, “Special Imaging Techniques,” in *Digital Signal Processing: a Practical Guide for Engineers and Scientists*, United States: Elsevier Science & Technology, 2002.

[134] “Help Online - Origin Help - Gauss.” https://www.originlab.com/doc/origin-help/gauss-fitfunc (accessed Oct. 20, 2024).

[135] “Focus Measure - File Exchange - MATLAB Central.” https://uk.mathworks.com/matlabcentral/fileexchange/27314-focus-measure (accessed Dec. 08, 2022).

[136] J. Geusebroek, F. Cornelissen, A. W. M. Smeulders, and H. Geerts, “Robust autofocusing in microscopy,” *Cytom. J. Int. Soc. Anal. Cytol.*, vol. 39, no. 1, pp. 1–9, 2000.

[137] E. Abbe, “Beiträge zur Theorie des Mikroskops und der mikroskopischen Wahrnehmung,” *Arch. für mikroskopische Anat.*, vol. 9, no. 1, pp. 413–468, 1873.

[138] “Straighten...” https://imagej.net/plugins/straighten (accessed Dec. 04, 2022).

[139] “TransformJ: Rotate.” https://imagescience.org/meijering/software/transformj/rotate/ (accessed Dec. 06, 2022).

Appendix A

Maximum projections before saturated artefact correction and before application of magma lookup table for the three different scenarios that are shown in Figure 81 respectively.